โครงสร้างระดับไมโครและสมบัติไดอิเล็กทริกของฟิล์มบางแคลเซียมคอปเปอร์ไททาเนต เตรียมโดยวิธีโซล-เจล

นางสาวยูมัยเราะห์ กาซา

วิทยานิพนธ์นี้เป็นส่วนหนึ่งของการศึกษาตามหลักสูตรปริญญาวิทยาศาสตรมหาบัณฑิต

สาขาวิชาฟิสิกส์ ภาควิชาฟิสิกส์

คณะวิทยาศาสตร์ จุฬาลงกรณ์มหาวิทยาลัย

ปีการศึกษา 2553

ลิขสิทธิ์ของจุฬาลงกรณ์มหาวิทยาลัย

MICROSTRUCTURAL AND DIELECTRIC PROPERTIES OF CALCIUM COPPER TITANATE THIN FILMS PREPARED BY A SOL-GEL METHOD

Miss Yumairoh Kasa

A Thesis Submitted in Partial Fulfillment of the Requirements
for the Degree of Master of Science Program in Physics
Department of Physics
Faculty of Science
Chulalongkorn University
Academic Year 2010
Copyright of Chulalongkorn University

Thesis Title MICROSTRUCTURAL AND DIELECTRIC PROPERTIES OF CALCIUM COPPER TITANATE THIN FILMS PREPARED BY A SOL-GEL METHOD

By Miss Yumairoh Kasa

Field of Study Physics

Thesis Advisor Assistant Professor Satreerat K. Hodak, Ph.D.

Accepted by the Faculty of Science, Chulalongkorn University in Partial Fulfillment of the Requirements for the Master's Degree

Deputy Dean for Administrative Affairs,

. . . . Acting Dean, The Faculty of Science

(Associate Professor Vimolvan Pimpan, Ph.D.)

THESIS COMMITTEE

. . . . Chairman

(Assistant Professor Sojiphong Chatraphorn, Ph.D.)

. . . . Thesis Advisor

(Assistant Professor Satreerat K. Hodak, Ph.D.)

. . . . Examiner

(Santipong Boribarn, Ph.D.)

. . . . External Examiner

(Wisit Singhsomroje, Ph.D.)

ยูมัยเราะห์ กาซา : โครงสร้างระดับไมโครและสมบัติไดอิเล็กทริกของฟิล์มบางแคลเซียมคอปเปอร์ไททาเนตเตรียมโดยวิธีโซล-เจล. (MICROSTRUCTURAL AND DIELECTRIC PROPERTIES OF CALCIUM COPPER TITANATE THIN FILMS PREPARED BY A SOL-GEL METHOD) อาจารย์ที่ปรึกษาวิทยานิพนธ์หลัก : ผศ. ดร. สตรีรัตน์ กำแพงแก้ว โฮดัค, 100 หน้า.

แคลเซียมคอปเปอร์ไททาเนต (CCTO) ซึ่งเป็นสารที่มีโครงสร้างแบบเพอรอฟสไกต์ได้รับความสนใจอย่างมากเนื่องจากเป็นสารที่มีค่าคงที่ไดอิเล็กทริกสูง ฟิล์มบาง CCTO ถูกเตรียมด้วยเทคนิคโซลเจลแบบสปิน ฟิล์มบาง CCTO จะถูกสังเคราะห์ลงบนแผ่นรองรับที่แตกต่างกัน เพื่อที่จะศึกษาผลของแผ่นรองรับที่มีต่อโครงสร้างระดับไมโครและสมบัติไดอิเล็กทริกของฟิล์ม ฟิล์ม CCTO ที่ปลูกลงบนแผ่นรองรับแลนทานัมอะลูมิเนตมีแนวโน้มที่จะเป็นเอพิแทกซี CCTO ฟิล์มที่ปลูกลงบนแผ่นรองรับทั้งแลนทานัมอะลูมิเนตและนิโอดิเมียมแกลเลตแสดงการจัดเรียงตัวอย่างโดดเด่นของระนาบ {200} ด้วยค่าคงที่แลตทิซ 7.391 อังสตรอม และ 7.390 อังสตรอม ตามลำดับ แต่ฟิล์มที่ปลูกลงบนแผ่นรองรับซิลิกอนมีลักษณะเป็นพหุผลึกด้วยค่าคงที่แลตทิซ 7.380 อังสตรอม ผลจากกล้องจุลทรรศน์อิเล็กตรอนแบบส่องกวาดชี้ให้เห็นว่า ขนาดเกรนของฟิล์มที่ปลูกลงบนซิลิกอน แลนทานัมอะลูมิเนต และนิโอดิเมียมแกลเลต มีค่าเป็น 58 40 และ 44 นาโนเมตร ตามลำดับ สำหรับฟิล์มที่โดปด้วยเหล็ก พีคลักษณะเฉพาะของ CCTO จะยังคงมีอยู่จนกว่าความเข้มข้นของการโดปเหล็กไม่เกิน 6 % โดยน้ำหนัก การมีอยู่ของเหล็กในฟิล์มแสดงสถานะออกซิเดชัน Fe^{3+} ซึ่งสามารถพิสูจน์ได้โดยเทคนิคการวัดการดูดกลืนรังสีเอ็กซ์ ค่าคงที่ไดอิเล็กทริกของฟิล์ม CCTO ที่ปลูกบนแผ่นรองรับอะลูมินาและนิโอดิเมียมแกลเลตมีค่าลดลงเมื่อความถี่เพิ่มขึ้นตั้งแต่ 40 กิโลเฮิรตซ์ ถึง 1 เมกกะเฮิรตซ์ สำหรับฟิล์มที่ปลูกลงบนแผ่นรองรับนิโอดิเมียมแกลเลตมีค่าคงที่ไดอิเล็กทริกสูงประมาณ 1044-1020 ด้วยค่าความสูญเสียไดอิเล็กทริกประมาณ 0.0263-0.0134 นอกจากนี้ ค่าคงที่ไดอิเล็กทริกของฟิล์มที่ปลูกลงบนแผ่นรองรับนิโอดิเมียมแกลเลตสามารถถูกปรับได้ด้วยค่าเปอร์เซนต์การปรับเปลี่ยนเท่ากับ 2.6 เมื่อให้สนามไฟฟ้า 10^5 โวลต์ต่อเมตร

ภาควิชา …………ฟิสิกส์……   ลายมือชื่อนิสิต...

สาขาวิชา …………ฟิสิกส์…….   ลายมือชื่อ อ.ที่ปรึกษาวิทยานิพนธ์หลัก.........................

ปีการศึกษา ……….2553……...

THAI ABSTRACT PAGE

5072434023 : MAJOR PHYSICS

KEYWORDS : $CaCu_3Ti_4O_{12}$ THIN FILM / SOL-GEL TECHNIQUE / DIELECTRIC CONSTANT

YUMAIROH KASA : MICROSTRUCTURAL AND DIELECTRIC PROPERTIES OF CALCIUM COPPER TITANATE THIN FILMS PREPARED BY A SOL-GEL METHOD. THESIS ADVISOR : ASST. PROF. SATREERAT K. HODAK, Ph.D., 100 pp.

The high dielectric perovskite $CaCu_3Ti_4O_{12}$(CCTO) has recently attracted much attention. We have successfully prepared CCTO thin films by a sol-gel spin coating technique. We synthesized CCTO films on different types of substrates in order to study the effect of substrate types on the microstructure and dielectric properties of the films. The CCTO film grown on $LaAlO_3$ tended to be an epitaxial film. The CCTO films deposited both on $LaAlO_3$ and $NdGaO_3$ substrates showed {200} preferred orientation with the lattice constant of 7.391 Å and 7.390 Å, respectively. However, the films grown on Si were polycrystalline with the lattice constant of 7.380 Å. The Field Emission Scanning Electron Microscopy results indicated that the grain size of the films grown on Si, $LaAlO_3$ and $NdGaO_3$ were 58, 40 and 44 nm, respectively. For the Fe doped CCTO film, the characteristic peaks of CCTO were preserved as long as the concentration of the Fe-doped did not exceed 6% by weight. The existing of Fe in our films present Fe^{3+} oxidation state which were confirmed by X-ray Absorption Spectroscopy result. The dielectric constant of the CCTO film grown on Al_2O_3 and NGO substrates decrease with the increasing of frequency 40 kHz up to 1 MHz. The dielectric constant is high about 1044-1020 with low dielectric loss about 0.0263-0.0134 for the film deposited on NGO substrate. Moreover, the dielectric constant of the film deposited on NGO can be tuned with tunability of 2.6% by applying an electric field of 10^5 V/m.

Department : .. . . Physics . . . . . .   Student's Signature . . . .

Field of Study : . . . . . . Physics . . . . . .   Advisor's Signature . . . .

Academic Year : . . . . 2010 . . . .

Acknowledgements

During my graduate study at Chulalongkorn University, I have had a very great time and valuable experiences both in academic and personal life. I would like to thank all those who gave endless support to me.

First of all, I would like to express my deep gratitude to my advisor, Assistant Professor Dr. Satreerat K Hodak, for her guidance, understanding, encouragement, and friendly discussion during this work.

I express my sincere thanks to Assistant Professor Dr. Sojiphong Chatraphorn, Dr. Santipong Boribarn and Dr. Wisit Singhsomroje for attending as a chairman and committee of this thesis. Special thank goes to Dr. Anurat Wisitsoraat and Mr. Disayut Phokharatkul for helping in electrode sputtering and dicing the samples.

I would like to thank Synchrotron Light Research Institute (Public organization) for helping in XAS measurment at beamline 8, Siam Photon Laboratory, Nakhon Ratchasima province.

I would also take this opportunity to thanks the Department of Physics, Faculty of science and Center of Innovative Nanotechnology, Chulalongkorn university for financial support in doing this thesis as well as paying for expenses to attend the conference.

My sincere thanks also go to Miss Thidarat Supasai, Miss Ornnicha Kongwut, Mr. Pavarit Promsena and to all my friends and colleagues, for their fun, help, suggestion and a good relationship throughout my study.

Finally, I would like to express my deepest gratitude to my family for their love, understanding, encouragement and support throughout my entire study.

Contents

Page

Abstract (Thai) .... **iv**

Abstract (English) .... **v**

Acknowledgements .... **vi**

Contents .... **vii**

List of Tables .... **x**

List of Figures .... **xi**

Chapter

I INTRODUCTION **1**

1.1 Motivation 1

1.2 Aims of thesis 3

1.3 Overview of thesis 3

II THEORETICAL BACKGROUND **5**

2.1 $CaCu_3Ti_4O_{12}$ (CCTO) properties and applications 5

2.2 Concept of sol-gel process 6

2.3 Dielectric properties 10

2.3.1 Dielectric constant and loss 10

Page

III CHARACTERIZATION TECHNIQUES **15**

3.1 X-Ray Diffractometry 15

3.2 Atomic force microscopy 19

3.3 Field emission scanning electron microscopy 21

3.4 X-ray absorption spectroscopy 24

IV EXPERIMENTAL METHODS **28**

4.1 CCTO thin film synthesis 28

4.1.1 CCTO and Fe-doped CCTO precursor preparation 28

4.1.2 Substrate conditions and cleaning 29

4.1.3 Spin coating technique 32

4.2 Thin film characterization 35

4.2.1 Crystal structure determination of the CCTO thin films . . 35

4.2.2 Surface morphology, grain size and surface roughness determination of the CCTO thin films 36

4.2.3 Surface morphology, cross section and elemental composition determination of the CCTO films 36

4.2.4 Determination of oxidation state of Fe ion 37

4.3 Dielectric measurement 37

4.3.1 Conversion from capacitance to dielectric constant 39

V RESULTS AND DISCUSSION **41**

5.1 Effect of annealing temperature on structural properties and surface morphology of CCTO films 41

Page

5.2 Effect of substrates on structural properties and surface morphology of CCTO films 46

5.3 Effect of Fe-doping on structural properties and surface morphology of CCTO films 57

5.4 Electrical properties of CCTO films 62

VI CONCLUSIONS 72

References 76

Appendices 81

Appendix A: Fe-doping concentration 82

Appendix B: XRD Database 83

Appendix C: Conference Presentation 90

Appendix D: Publication 92

Vitae 100

List of Tables

Table **Page**

4.1 Si Single Crystal Substrate Properties. 30

4.2 LAO Single Crystal Substrate Properties. 30

4.3 NGO Single Crystal Substrate Properties. 31

4.4 Al_2O_3 Substrate Properties. 31

5.1 Summary of the CCTO peak analysis and lattice parameter obtained from XRD. 57

5.2 The stoichiometry of pure and Fe-doped CCTO films with different Fe contents. 61

List of Figures

Figure **Page**

2.1 Schematic representation of the unit cell of CCTO [23]. 6

2.2 Schematic illustration of a sol-gel process for material fabrication. . 8

2.3 The relationship between the film thickness and the spinning speed (left) and the spinning time (right). 9

2.4 Orientations of polar molecules in (a) an absence external electric filed (b) an applied external electric field. 10

2.5 Orientations of non-polar molecules in (a) an absence external electric filed (b) an applied external electric field. 11

2.6 Polarizability VS frequency. 14

2.7 A permittivity spectrum over a wide range of frequencies [31]. . . . 14

3.1 X-Ray tube. 16

3.2 (a) Characteristic X-ray (b) K-line spectrum of characteristic X-ray. 17

3.3 X-ray spectrum of molybdenum at 35 kV. The zoom view of K-line spectrum showing the separated $K_{\alpha 1}$ and $K_{\alpha 2}$ [32]. 17

3.4 Bragg's law. 18

3.5 Schematic diagram of the AFM components. 19

3.6 The Lernard Jones potential. 20

3.7 Schematic diagram of field emission scanning electron microscope. . 22

Page

3.8 Interaction between sample surface and primary incident electron. . 23

3.9 The interaction volume within a sample. 23

3.10 The schematic diagram of XAS experiment. 25

3.11 An example of absorption edges according to electronic transition (up arrows refer to X-ray absorption, down arrows refer to fluorescent X-ray emission). 26

3.12 An example of XAS spectrum. 27

4.1 The flow chart of synthesis pure and Fe-doped CCTO precursor. . . 29

4.2 Spin coater (SPIN COATER model P6700 series). 33

4.3 Temperature profile for annealing thin film. 34

4.4 The flow chart for the fabrication of pure and Fe-doped CCTO films. 34

4.5 X-ray diffractometer (BRUKER model D8-Discover). 35

4.6 Atomic force microscope (Veeco model Nanoscope IV). 36

4.7 Impedance analyzer (HP 4192A). 38

4.8 The image of CCTO interdigitated capacitor. 38

4.9 The CCTO interdigitated capacitor in a ring resonator. 39

4.10 FESEM image of the interdigitated electrode. 40

5.1 The XRD pattern of the CCTO films at various annealing temperature (a) 600 °C, (b) 700 °C, (c) 800 °C, (d) 900 °C and (e) 1000 °C. 43

5.2 AFM images (2×2 μm^2) in 2D and 3D of the CCTO films deposited on Si substrate. (a) and (b) annealed at 800 °C, (c) and (d) annealed at 900 °C, (e) and (f) annealed at 1000 °C. 45

Page

5.3 The XRD pattern of the CCTO film deposited on Si substrate annealed at 800 °C 46

5.4 AFM images (1×1 μm^2) in 2D and 3D of the CCTO films deposited on (a) and (b) Si substrate, (c) and (d) LAO substrate, (e) and (f) NGO substrate. 48

5.5 FESEM micrograph of the CCTO film deposited on Si substrate at 800 °C (a) plane view, (b) cross section and (c) the zoom of interface between the CCTO film and Si substrate surface. 49

5.6 X-ray diffractogram of CCTO film deposited on LAO substrate at 800 °C 51

5.7 The plane view of locations of atoms in (a) LAO (100) substrate (b) CCTO (200). 51

5.8 FESEM images of the CCTO film grown on LAO substrate at 800 °C (a) plane view, (b) cross section and (c) the zoom of interface between the CCTO film and the LAO substrate surface. 53

5.9 XRD spectra of the CCTO film grown on NGO substrate at 800 °C . 54

5.10 The plane view of locations of atoms in (a) NGO (110) substrate (b) CCTO (200). 54

5.11 FESEM microstructure of the CCTO film deposited on NGO substrate at 800 °C (a) plane view, (b) cross section and (c) the zoom of interface between the CCTO film and the NGO substrate surface. 56

5.12 The XRD spectra of pure and Fe-doped CCTO films with various Fe concentrations deposited on Si substrates at 800 °C 58

Page

5.13 The FESEM surface morphology of CCTO films deposited on Si substrates at 800 °C with different Fe concentrations (a) 4 wt%, (b) 5 wt%, (c) 6 wt% and (d) 7 wt% 60

5.14 The XANES spectra of Fe-doped CCTO films deposited on Si substrates at 800 °C with different Fe concentrations and the zoom of pre-edge region (inset). 61

5.15 XRD spectra of the CCTO thin film on alumina substrate annealed at 800 °C. 63

5.16 2D AFM images of the CCTO films deposited on (a) alumina substrate (b) NGO substrate annealed at 800 °C. 63

5.17 The frequency dependence of the capacitance of the CCTO thin film grown on alumina substrate annealed at 800 °C. 65

5.18 The frequency dependence of the capacitance of the CCTO thin film grown on NGO substrate annealed at 800 °C. 66

5.19 The (a) dielectric constant and (b) dielectric loss of the CCTO film deposited on Al_2O_3 substrate at 800 °C with different applied voltage. 68

5.20 The (a) dielectric constant and (b) dielectric loss of the CCTO film deposited on NGO substrate at 800 °C with different applied voltage. 69

5.21 The (a) semiconducting grains between grain boundaries and (b) equivalent circuit for the microstructure of CCTO. 70

CHAPTER I

INTRODUCTION

1.1 Motivation

Reducing size of microelectronic devices in the form of thin films such as capacitor in Dynamic Random Access Memory (DRAM) has attracted much interest in the industry and research fields. In recent years, $CaCu_3Ti_4O_{12}$ (CCTO) has been considered to be the first choice in reducing device dimension because of its giant dielectric constant over a wide temperature range (100-600 K) and a frequency range up to 1 MHz [1, 2]. Indeed, the dielectric constant of CCTO single crystal and ceramic is on the order of 10^5 and 10^4, respectively whereas that for the film is on the order of 10^3 [3, 4]. The origin of high dielectric constant behavior of CCTO have been proposed to be due to either an intrinsic or an extrinsic properties. At present, it has been accepted that the extrinsic properties associated with electrical heterogeneities such as insulating grain boundary layers between semi-conducting grain which similar in internal barrier layer capacitor (IBLC) and contact between sample and electrode effect are originated the high dielectric behavior in CCTO material [5, 6, 7, 8]. The values of dielectric constant depend on preparation methods that can affect the crystal formation of the materials [9]. Many researchers have reported on thin film synthesis on various substrates by physical deposition technique such as pulsed laser deposition (PLD) [10, 11] and sputtering [12]. Some works have reported on CCTO thin film preparation by chemical deposition such as sol-gel technique [13] and metal organic chemical vapor deposition (MOCVD) [14]. In the work of Shri Prakash et al., the polycrys-

talline CCTO thin films deposited on Pt(111)/Ti/SiO_2/Si substrate using radio frequency magnetron sputtering have a high dielectric constant about 5000 at 1 kHz and 400 K [12]. While in the studies of Si et al., the epitaxial CCTO films grown by PLD method on $LaAlO_3$ (LAO) substrate with $LaNiO_3$ (LNO) buffer layer have a constant dielectric value about 1500 at frequency range about 200 Hz-100 kHz and temperature about 100-150 K [15]. Some groups have fabricated CCTO thin film on LAO substrate by MOCVD technique but they did not report any dielectric measurements on their films [14]. Maurya et al. have reported that the CCTO film grown on Pt/Ti/SiO_2/Si substrates by sol-gel process showed the dielectric constant about 900 at 100 kHz when acetic acid was used to prepare the sol [16]. Besides the preparation method, changing substrate types also have an effect on dielectric constant. The dielectric constant of the CCTO film grown by PLD on Pt/Ti/SiO_2/Si substrate is about 983 at 100 kHz [17]. While in the work of Zhao et al. the dielectric constant of the CCTO film deposited on single crystal LAO substrate by PLD method is over about 2000 at 100 kHz [11]. By using the same method in depositing the film with different types of substrates, the obtained dielectric constant was quite different. In this work, we synthesized the CCTO films on various types of substrates. In the beginning of this work, we deposited the CCTO films on Si substrates in order to find the optimum temperature with minimum peak quantities of impurities and highest CCTO peak intensities. The CCTO films then were grown on single crystal LAO and NGO substrates which have similar crystal structure and and small lattice mismatch to CCTO films. The lattice mismatch of CCTO films on LAO substrate is about 2.5% smaller than that on NGO substrates which is about 4.3%. We also deposited the CCTO films on Al_2O_3 substrate, which is an electrical insulator substrate, to design the capacitor and calculate the dielectric constant of the film. We reported the dielectric properties of the films on Al_2O_3 substrate and compared the results with NGO single crystal substrate.

Recently, many groups have studied the effect of various dopants e.g. Mn, Ni, Co, Fe on structural, magnetic and dielectric properties. Chiodelli et al. reported

that the giant permittivity of bulk CCTO can be strongly increased to values of about 150000 by Co doping on Ti site [18]. Grubbs et al. reported that Fe doping in CCTO film revealed the lower dielectric loss compared with the undoped film [19]. Several research groups are interested in doping Fe or Mn in CCTO due to the simultaneous responses of electronic and magnetic properties [20, 21]. Many works have been reported on the CCTO ceramic doping and few works report on the CCTO thin film doping. In this thesis, we also report the effect of Fe-doped CCTO thin film on structural and morphology properties.

1.2 Aims of thesis

1) To investigate the optimum temperature for growing CCTO film on Si substrate by a sol-gel technique as well as to examine the effect of different substrates ($LaAlO_3$, $NdGaO_3$ and Al_2O_3) on structural and dielectric properties of CCTO films

2) To characterize the effect of Fe doped on structural properties of the CCTO films by X-ray diffractometry and field emission scanning electron microscopy.

1.3 Overview of thesis

This thesis is organized as follows:

Chapter II: In this chapter, I introduce the CCTO crystal structure, the basic principle of sol-gel technique and the general concept of dielectric constant and dielectric loss.

Chapter III: In this chapter, I explain the basic principles of the characterization techniques including XRD, AFM, FESEM and XAS.

Chapter IV: The experimental methods of CCTO thin film synthesis, thin film characterization and dielectric measurement are described.

Chapter V: The effects of temperature, different types of substrates, Fe-doping on CCTO film properties are shown and discussed.

Finally, Chapter VI: Conclusion of the thesis.

CHAPTER II

THEORETICAL BACKGROUND

In this chapter I will explain the general details of $CaCu_3Ti_4O_{12}$ material, their properties and applications. Then, concept of sol-gel process which was used to prepare the $CaCu_3Ti_4O_{12}$ thin film will be described. Finally, the dielectric properties which consist of dielectric constant and dielectric loss are explained.

2.1 $CaCu_3Ti_4O_{12}$ (CCTO) properties and applications

$CaCu_3Ti_4O_{12}$ has a cubic perovskite (ABO_3) related structure by an octahedral tilting distortion. This distortion is due to a size mismatch between the A-cations and the ABO_3 cubic. It has been reported that CCTO has no phase transition [22]. The lattice parameter of CCTO is 7.391 Å. Fig. 2.1 presents the unit cell structure of CCTO [23]. Ca atom (gray) is located at the center and the corners of unit cell, Cu atom (red) is located at the center of edge and the facial plane and Ti atom (yellow) is placed inside of octahedral cage with six oxygen atoms (blue) surrounding, forming TiO_6.

Many phases of $CaCu_3Ti_4O_{12}$ compound were discovered around 1967s [24]. In 1970s, more phases of CCTO were widely explored and the accurate structures were determined by Bochu et al [25]. However, the study of CCTO on their structural and electrical properties were begun very recently. Many researchers reported that there was no evidence of any structural phase transition in the

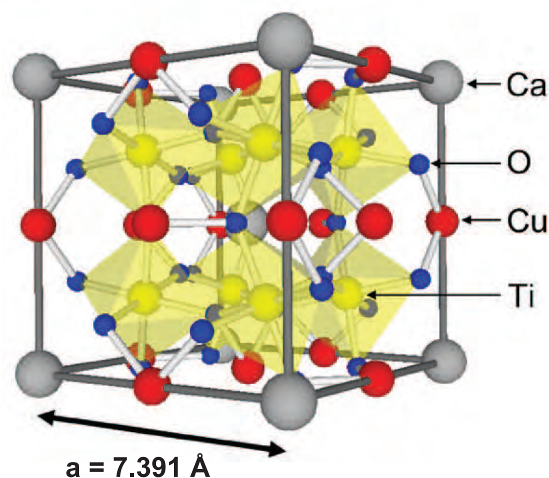

Figure 2.1: Schematic representation of the unit cell of CCTO [23].

CCTO structure from 100 K up to 600 K [26, 10]. Subramanian et al. [1] were the first group that study the dielectric properties of CCTO powders. The dielectric constant of the CCTO powder exhibited on the order of 12,000 and nearly constant from room temperature to 300 °C. The dielectric constant of the CCTO presented small dependence on temperature [27]. After there have been reports on the high dielectric constant of CCTO, the electrical properties of CCTO have attracted much interest in the research field. Due to their high dielectric constant over a wide range of temperature, CCTO thin films were suitable for capacitor application, microelectronic and microwave devices (cell phones) as well as gas sensors [28, 29, 30].

2.2 Concept of sol-gel process

Sol-gel process is a chemical process for the fabrication of materials e.g. thin films, ceramics, glasses. Such process is the phase transformation of a sol, which is solution containing solid particles in suspension, to form a gel, which is a solid network containing liquid components. During the sol-gel process, there are three chemical reactions occurred namely, hydrolysis, water condensation and alcohol condensation reactions as seen in equation 2.1- 2.3, leading to the formation of a

sol.

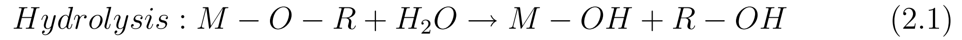

$$Hydrolysis : M - O - R + H_2O \rightarrow M - OH + R - OH \quad (2.1)$$

$$Water\ Condensation : M - OH + HO - M \rightarrow M - O - M + H_2O \quad (2.2)$$

$$Alcohol\ Condensation : M - O - R + HO - M \rightarrow M - O - M + R - OH \quad (2.3)$$

where M is a metal, OR is an alkoxyl group and OH is hydroxyl group.

In addition, the sol can apply in various types of materials as illustrated in Fig. 2.2. For example, thin films could be produced with sol by spin- or dip-coating on different substrates. After the sol is cast on a substrate, a wet gel will form. The extraction of liquid in wet gel under suitable condition was produced aerogel which is a highly porous and extremely low-density material. If the wet gel is evaporated, xerogel will occur and form dense ceramics after heat treatment. A uniform particle was formed by sol precipitation process. In the process of spin- or dip-coating, we avoid the sol precipitation on the films by selecting only the clear solution for the depositing process.

Generally, thin films coating can be obtained from spin- and dip-coating. In this work, I focus on spin coating technique. The spin coating technique can be done by the following steps. First, the substrate was loaded on a stage in spin coater. When the substrate was spun at high speed (typically around 3000 rpm), the clear sol then was dropped onto the center of the substrate and the sol is spread to the edge of the substrate. Then, the film was dried in order to eliminate the excess solvents from the film. The process was repeated to obtain the films with desired thickness. Spin speed is an important factor in controlling the thickness of the films. Usually, higher spin speeds and longer spin times create the thinner films as seen in Fig. 2.3. The spinning speed and spinning time used

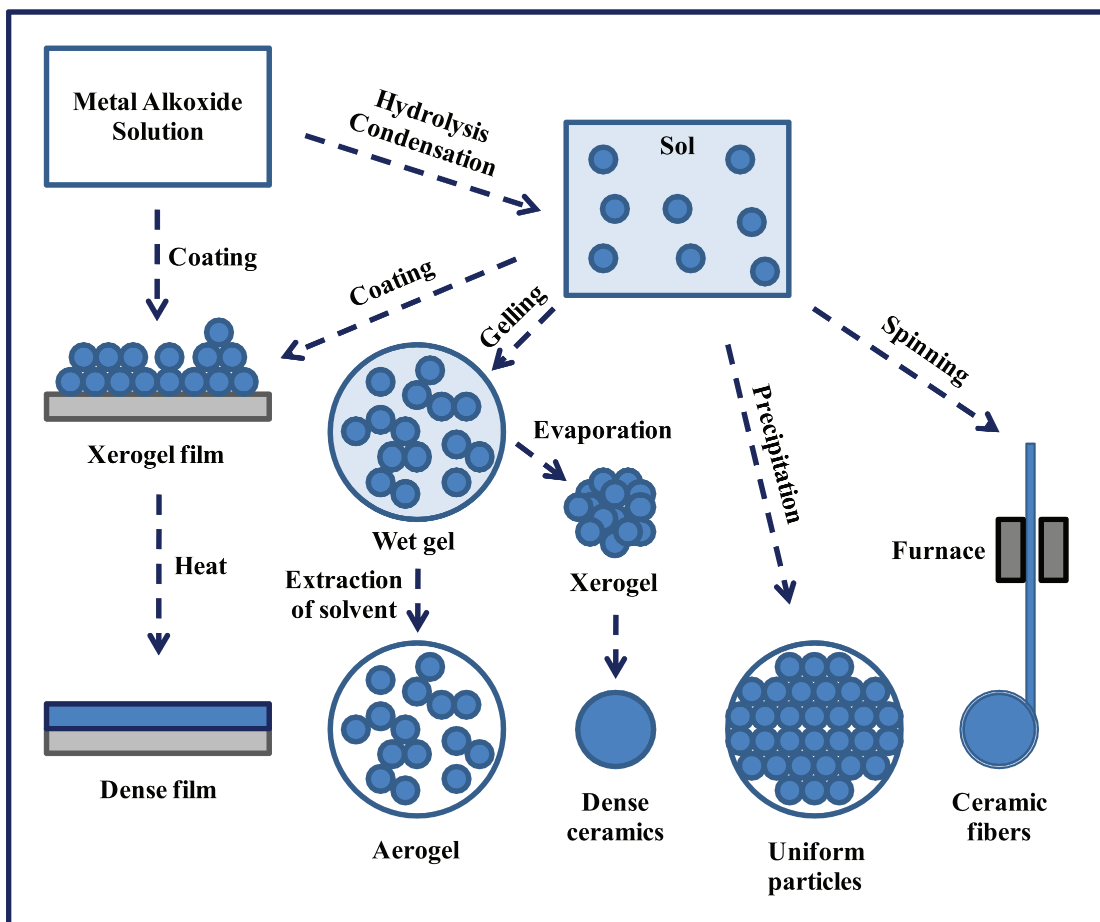

Figure 2.2: Schematic illustration of a sol-gel process for material fabrication.

in this thesis work was about 2000 rpm and 40 s, respectively which are similar to the spinning conditions of the work done by Jimenez et al [13]. Note that in this thesis, I did not measure the viscosity of the precursor and vary the spinning speed and time due to the high cost of copper acetate substance. In addition, the amount of precursor needed in the viscosity measurement system in order to obtain the value of viscosity has to be an order of many liters.

The advantages of sol-gel method are the possibility to obtain good homogeneity, precise composition control, large area coating and complex substrate coating. It requires simple and low cost apparatus and operation without using high vacuum. However, there are some limitation of sol-gel method, for example, the precursor are sensitive to react with the air atmosphere and the cracking of the films readily occur during drying process.

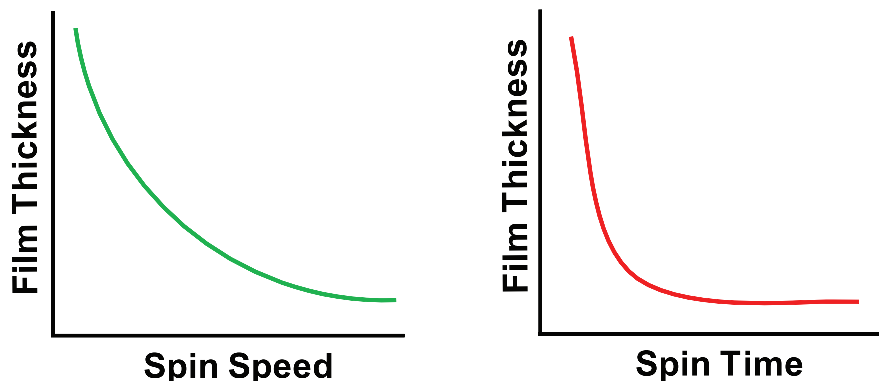

Figure 2.3: The relationship between the film thickness and the spinning speed (left) and the spinning time (right).

2.3 Dielectric properties

Dielectric are electrical insulating materials but they can carry small electric current because in microscopic point of view dielectrics consist of charges which attached to specific atoms or molecules. All charges can move a little bit within atoms or molecules when an external field is applied. Dielectrics can be divided into two types: polar and non-polar dielectrics. Polar dielectrics are dielectrics that have permanent electric dipole moments, when an external electric field is applied the orientation of polar molecule tended to align with an external field as shown in Fig. 2.4. However, the alignment is not complete due to the thermal agitation of the molecule. Non-polar dielectrics are dielectrics that do not have permanent electric dipole moments but electric dipole moments can be induced when applied an external filed as illustrated in Fig. 2.5. In this thesis, I will focus on the property of dielectric material in term of dielectric constant and dielectric loss.

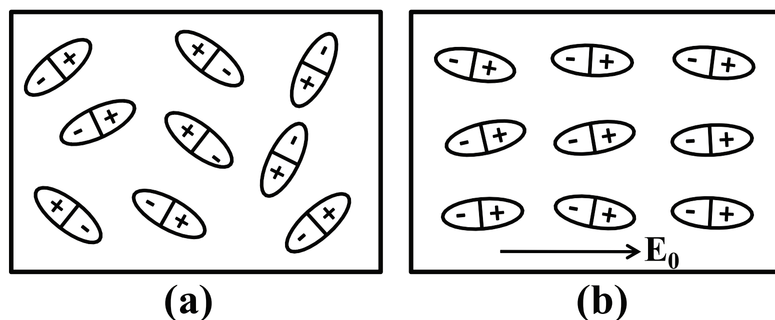

Figure 2.4: Orientations of polar molecules in (a) an absence external electric filed (b) an applied external electric field.

2.3.1 Dielectric constant and loss

When we applied an external electric field to the capacitor that fills a dielectric material between plates. The dielectric material that consists of permanent or induce dipole moments will align in the direction of an external field produced po-

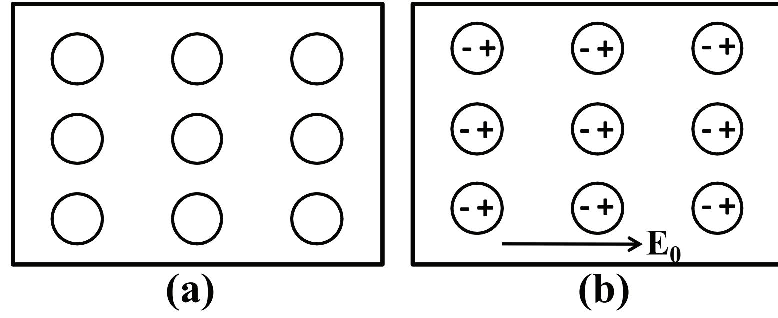

Figure 2.5: Orientations of non-polar molecules in (a) an absence external electric filed (b) an applied external electric field.

larization. Under applied electric field (E), the electric displacement D is described by

$$\overrightarrow{D} = \varepsilon_0 \overrightarrow{E} + \overrightarrow{P} \tag{2.4}$$

The term $\varepsilon_0 \overrightarrow{E}$ represents field due to free charge (the free charge means ions that embedded in dielectric materials) and $\overrightarrow{P}$ represents the field due to polarization in dielectric. The polarization $\overrightarrow{P}$ is proportional to the field $\overrightarrow{E}$ by

$$\overrightarrow{P} = \varepsilon_0 \chi_e \overrightarrow{E} \tag{2.5}$$

where χ_e is the electric susceptibility which is a parameter measuring the ease of polarization of a dielectric in response to an electric field. χ_e is dimensionless. From equation 2.4 leads to

$$\overrightarrow{D} = \varepsilon_0 \overrightarrow{E} + \varepsilon_0 \chi_e \overrightarrow{E} \tag{2.6}$$

$$\overrightarrow{D} = \varepsilon_0 \left(1 + \chi_e\right) \overrightarrow{E} \tag{2.7}$$

The term (1+χ_e) refers to dielectric constant (ε_r)

$$\overrightarrow{D} = \varepsilon_0 \varepsilon_r \overrightarrow{E} \tag{2.8}$$

where

$$\varepsilon = \varepsilon_0 \varepsilon_r \tag{2.9}$$

The ε is the permittivity of material and ε_0 is the permittivity of free space which has the value 8.85×10^{-12} C^2/Nm^2.
Therefore

$$\varepsilon_r = \frac{\varepsilon}{\varepsilon_0} \tag{2.10}$$

In summary, the dielectric constant or relative permittivity of material is the ratio of its permittivity (ε) to the permittivity of vacuum (ε_0). The permittivity is the value that explains the ability of a material to be polarized by an electric field. The dielectric constant of vacuum is 1, that means other materials are able to polarize than in vacuum. Therefore, the dielectric constant of a materials is always more than 1.

The dielectric constant of the material can be defined in the term of complex dielectric constant (ε^*)

$$\varepsilon^* = \varepsilon' - i\varepsilon'' \tag{2.11}$$

where ε' refers to the real part of the dielectric constant of the material and ε'' refers to the imaginary part of the dielectric constant of material which is the energy losses in dielectric material. The energy losses is converted to heat energy. The loss factor, which sometimes is called loss tangent, is related to the following expression

$$\tan\delta = \frac{\varepsilon''}{\varepsilon'} \tag{2.12}$$

The angle δ is equal to 0 in the ideal capacitor which means no losses in the capacitor.

In this thesis, I fabricated the CCTO coplanar capacitors and I will later explain how to convert the capacitance to dielectric constant in section 4.3.1. Since in the section 5.4 of this thesis shows the frequency dependence of the

dielectric constant and loss results, I will reveal the the frequency dependence of the dielectric constant in more detail in the next paragraph.

The dielectric response to frequency can be explained in the term of polarizability. Fig. 2.6 presents the frequency dependence of the electronic, ionic and dipolar polarizability. The electronic polarizability arises from the displacement of electron from the nucleus. The ionic polarizability occurs from the displacement of the charged ion in the crystal lattice. The dipolar polarizability is due to the motion of permanent dipole in dielectric material. From Fig. 2.6 it can be inferred that the dipolar and ionic polarisation respond at low frequency. At intermediate and high frequencies, there is a peak in the polarizability when the driving frequency resonant with the natural frequency of the electronic and ionic oscillations. The peak in the imaginary part of permittivity or the dielectric loss is accompanied at the same frequency as the resonant frequency at which there is an abrupt change with highest slope in the real part of permittivity or in the dielectric constant. In this thesis, the frequency range that I studied the dielectric responses for the CCTO films is in low frequency range (40 kHz-1Mz). Fig. 2.7 reveals that the permittivity spectrum over a wide range of frequency [31]. From the equation 2.5, the polarizability is proportional to the real part of the permittivity. When the ac electric field is applied in the terms of $\overrightarrow{E} = E_0 e^{-i\omega t}$ that means the dielectric material responses for that frequency f $= \omega/2\pi$. The response of the real and imaginary part of the polarizability to the applied frequencies are shown in Fig. 2.7. It has been seen that the real and imaginary part of the dielectric constant decrease with the increasing of frequency.

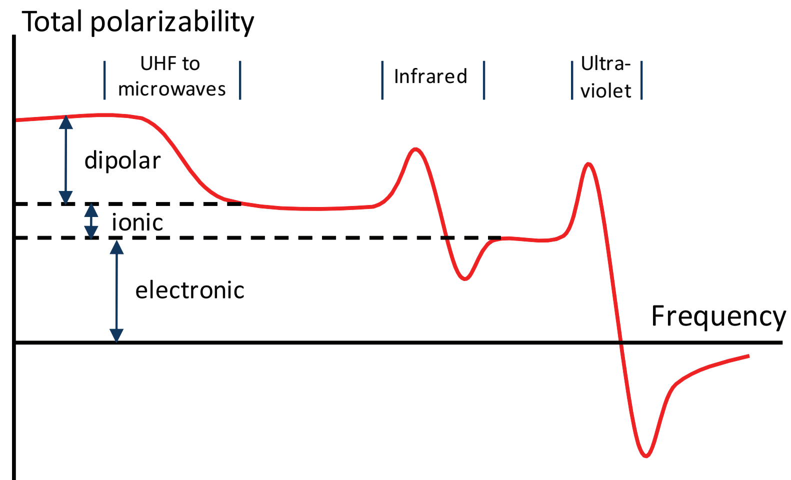

Figure 2.6: Polarizability VS frequency.

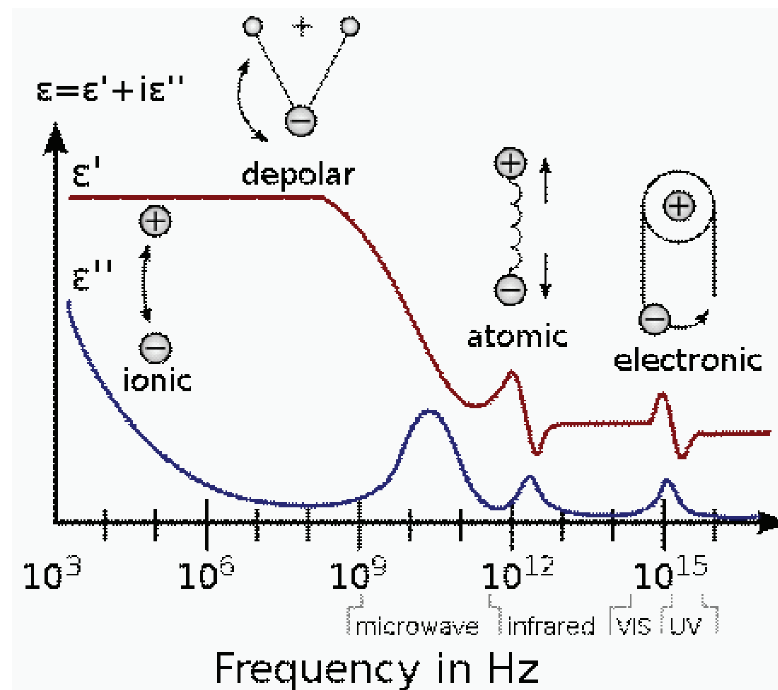

Figure 2.7: A permittivity spectrum over a wide range of frequencies [31].

CHAPTER III

CHARACTERIZATION TECHNIQUES

In this chapter, I will present the characterization techniques which were used to study the microstructure of our $CaCu_3Ti_4O_{12}$ films. The crystal structure of the films was examined by X-Ray diffractometer (XRD). The surface morphology of the films including grain size and roughness was analyzed by Atomic force microscopy (AFM). Field emission scanning electron microscopy (FESEM) was used to investigate the interface between the sample and the substrates, and also the surface morphology in a bigger scale. X-ray absorption spectroscopy (XAS) was used to examine the oxidation state of Fe in the film.

3.1 X-Ray Diffractometry

The X-Ray diffractometer (XRD) is an instrument for analysis crystal structure of the material by using X-ray diffraction principle. X-rays are electromagnetic radiation with wavelength in the range of 0.05-100 Å. The wavelength of X-ray is smaller than visible light (300-700 nm). The short wavelength of X-ray in the range of 0.5-2.5 Å is usually used to probe the material in order to determine the lattice parameters. Fig. 3.1 shows the X-ray tube which consists of an evacuated chamber, a cathode and an anode. At cathode, electrons are produced at the heating filament. The relatively positive high voltage is set at the anode causing the electrons to accelerate to the anode. A metal target is placed at the anode and the common targets are copper and molybdenum. When an electron hits an atom of the metal target, an inner shell electron moves out of the shell leaving a

hole and an outer shell electron moves down to the inner shell to fill in the hole. This electron transition results in the generation of characteristic X-rays.

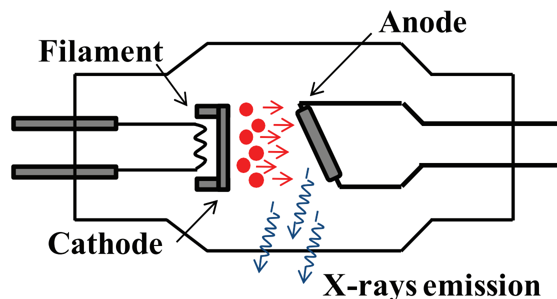

Figure 3.1: X-Ray tube.

X-rays which are produced from X-ray tube can be divided into two types; continuous X-ray and characteristic X-ray. Continuous X-ray or bremsstrahlung means braking radiation which occurs from inelastic scattering of electron when strikes the target result in losing energy. The resulting X-ray is continuous at which depends on applied voltage between cathode and anode. Characteristic X-ray are produced by transitions of orbital electrons from outer to inner shells which can be clearly explained by Bohr model of the atom as shown in Fig. 3.2 (a). In Bohr model, nucleus of the atom consists of neutron and proton is encircled by electron shells. The innermost called K-shell which are surrounded by L-shell and M-shell, respectively. When an incoming electron strikes the sample, an K-shell electron is removed which creates a vacancy and electrons with higher energy from L-shell or M-shell fill in the vacancy. These electronic transition produces X-ray and the transition from L-shell to K-shell produces K_{α} X-ray, as the transition from M-shell to K-shell produces K_{β} X-ray. The characteristic X-ray emission of K_{β} and K_{α} is shown as two sharp peaks as seen in Fig. 3.3. The base for the two sharp peaks on the left of Fig. 3.3 is continuous X-rays. The characteristic X-rays have a higher intensity than continuous X-ray and K_{α} X-rays have higher intensity than K_{β} X-rays. K_{α} is a combination of $K_{\alpha1}$ and $K_{\alpha2}$ [32] as seen in the expanded scale on the right of Fig. 3.3. $K_{\alpha1}$ and $K_{\alpha2}$ is produced by the filling of an electron from L_{III} and L_{II} in the vacancies of K-shell, respectively as shown in Fig. 3.2 (b).

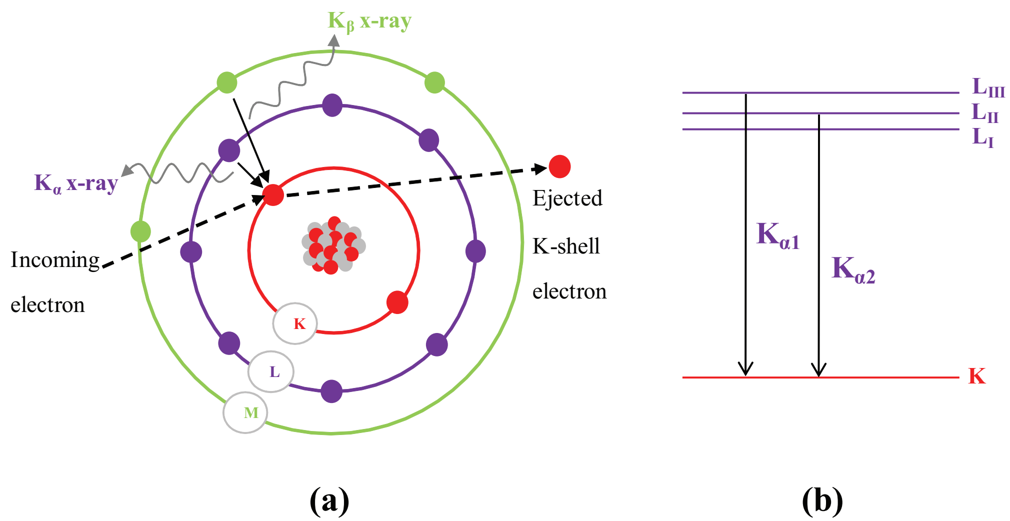

Figure 3.2: (a) Characteristic X-ray (b) K-line spectrum of characteristic X-ray.

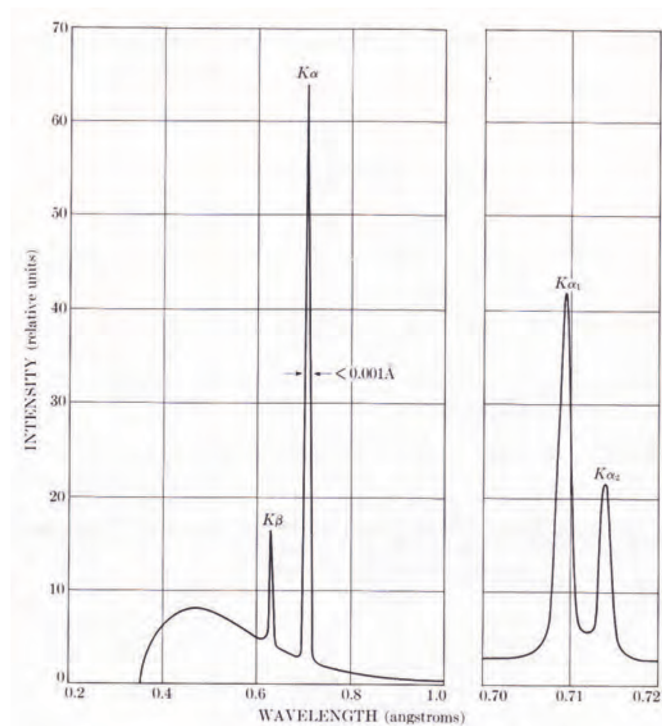

Figure 3.3: X-ray spectrum of molybdenum at 35 kV. The zoom view of K-line spectrum showing the separated $K_{\alpha 1}$ and $K_{\alpha 2}$ [32].

In this thesis, we used copper as a target with $K_{\alpha 1}$ wavelength about 1.5406 Å. The wavelength of the characteristic X-rays is different for each atom type in periodic table. Since the wavelength of the short X-rays is in the same range as the distance between the atomic plane in the material, from this reason X-ray is used to determine the lattice constants of various kinds of materials. The principle of XRD can be explained by Bragg's law as seen in equation 3.1. Fig. 3.4 represents the scattering of a monochromatic X-ray beam with one wavelength from crystal planes. When X-ray incident beam (ray 1 and ray 2) strikes the crystal planes at 1st and 2nd plane. The diffracted beam will have the maximum intensity if the path difference between the ray 1 and the ray 2 are equal to an integer times of the wavelength as shown in the formula:

$$2d \sin\theta = n\lambda \tag{3.1}$$

where d is the lattice spacing of the crystal,

θ is an incident angle which is the angle between the lattice plane and the incident beam,

λ is the wavelength of X-ray,

n is an integer.

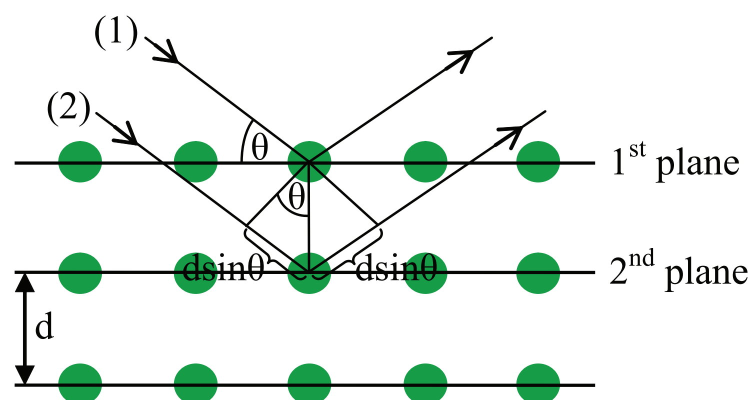

Figure 3.4: Bragg's law.

3.2 Atomic force microscopy

The atomic force microscopy (AFM) is a technique for investigating surface morphologies of relatively flat samples such as thin films and thick films. Generally, AFM consists of a very sharp tip attached to a microfabricated cantilever. Such a technique is based on the van der waals force upon the distance between the tip and the sample. Fig. 3.5 shows a schematic diagram of the AFM components. The laser beam is pointed at the back of the end of the cantilever where the tip is attached underneath it. The bending of the cantilever causes a change in reflected laser light from the back side of the cantilever either with the movement of the base where the sample is placed or the movement of the tip depending on each commercial model. The signal of reflected laser light detected by photodetector at different areas is converted to electrical signal. The AFM can be operated in three modes: the tip can be in constant contact with the sample called contact mode, it can be intermittently tapping gently on the sample called tapping mode and it can be slightly above the sample called non-contact mode.

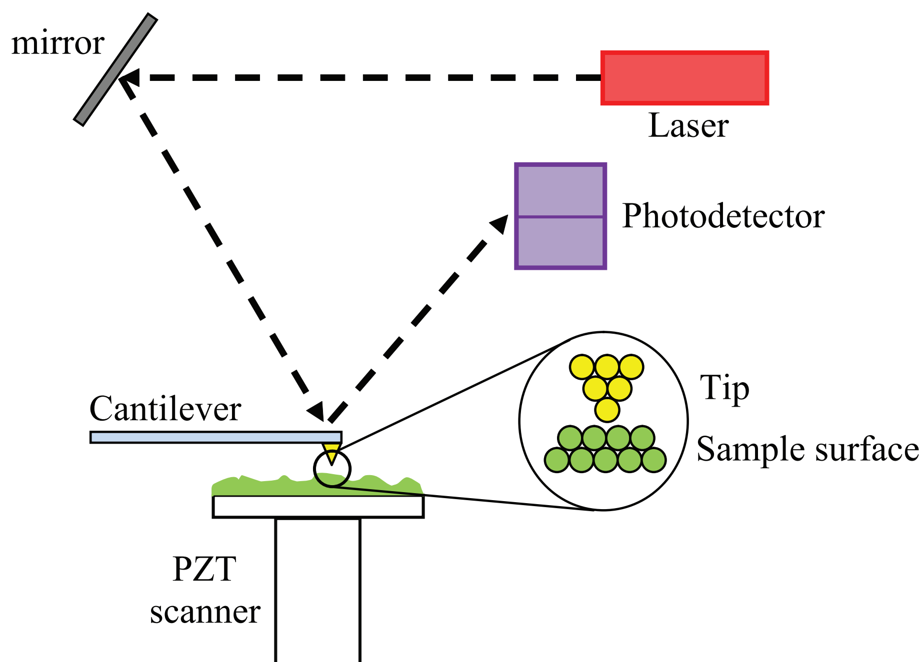

Figure 3.5: Schematic diagram of the AFM components.

The interaction between tip and sample surface is presented by a Lennard Jones Potential [33] as seen in Fig. 3.6. At the right side of the curve the tip is far from the sample surface. As the tip approaches to non-contact part, the distance between the sample surface and the tip is in the order of tens to hundreds angstroms and is in the range of attractive force. When the tip is in contact with the surface (less than a few angstroms), the force between the tip and the sample is repulsive.

In this thesis, tapping mode is used to characterize the surface of the films. For tapping mode, the cantilever used in this thesis is oscillating at or near its resonant frequency (300 kHz). The oscillation tip is then scanned at height where it nearly touches or taps the sample surface. Beside the surface morphology image, the surface roughness of the sample is also obtained in this mode. The surface roughness refers to root mean square (RMS) value. The RMS is standard deviation of the surface height values within the interested area and is calculated by

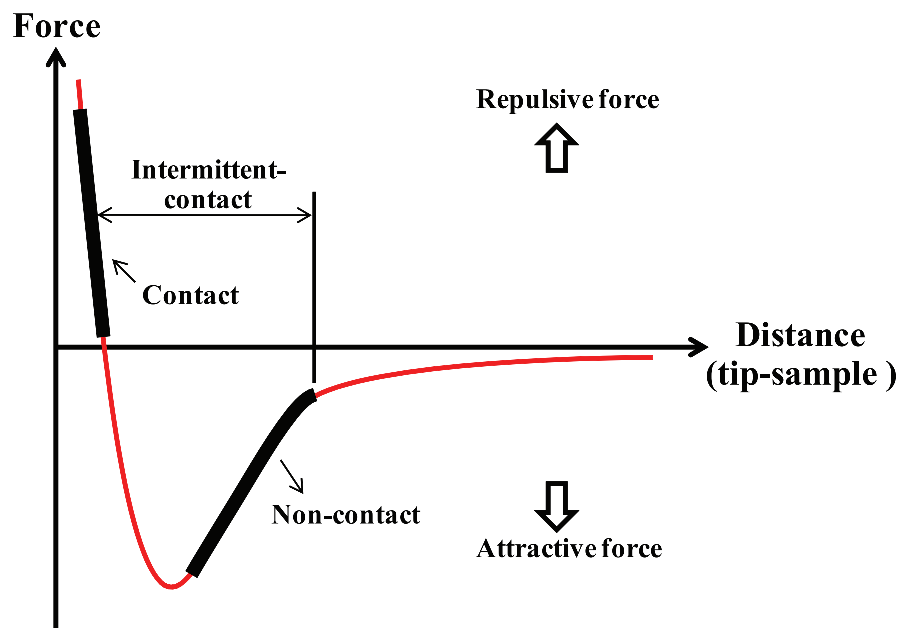

Figure 3.6: The Lernard Jones potential.

$$RMS = \sqrt{\frac{\sum_{i=1}^{N}(Z_i - \overline{Z})^2}{N}} \tag{3.2}$$

where Z_i is the surface height of each point,

$\overline{Z}$ is the average of the surface height within the interested area,

N is the number of point within the interested area.

In section 5.2, the result of both surface morphology and surface roughness obtained by AFM are shown.

3.3 Field emission scanning electron microscopy

The field emission scanning electron microscopy (FESEM) is one type of electron microscope that takes an image by using electrons instead of light to form an image. Surface, cross section as well as composition of the sample can be investigated by FESEM with high resolution approximately down to 2 nanometer (3 to 6 times better than scanning electron microscope (SEM)). Main differences between FESEM and SEM are emitter type. Thermionic emitter which use electrical current to heat up filament is used in SEM, while field emission source, also called a cold cathode field emitter, is used in FESEM. The cold cathode field emitter usually made of tungsten sharpened to a tip with radius about 100 nm. The filament does not need to be heated up but the tip is placed in a large electrical potential gradient. This gives electric field at the tip in the order of 10^{10} V/m which is high enough for electron emission from the cathode. By placing the cold cathode field emitter instead of the normal heated filament, can be clearer image, less electrostatically distorted image and high resolution obtained in FESEM. Fig. 3.7 presents the basic principle of the FESEM. A beam of electron is produced at the top of the microscope by a cold cathode filed emitter. The electron beam travels a vertical path and passes electromagnetic fields and lenses, focusing the beam down to the specimen.

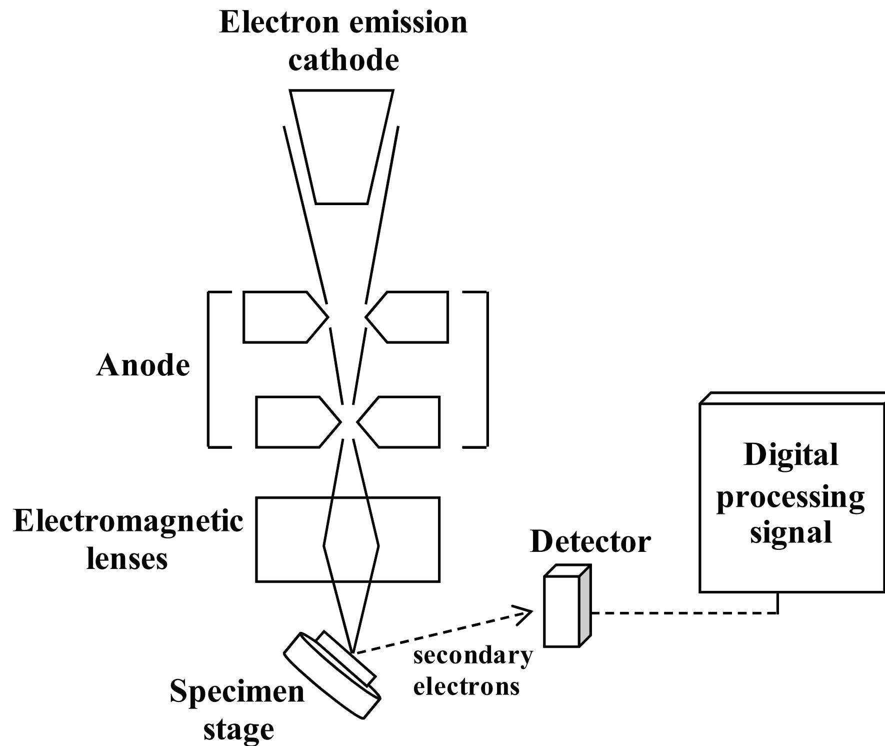

Figure 3.7: Schematic diagram of field emission scanning electron microscope.

These bombardment result in the generation of a variety of signals at surface and sub-surface of the sample. The signals are secondary electrons, back scattered electrons (BSE), characteristic x-ray, light (cathodoluminescence), auger electrons, and etc, as illustrated in Fig. 3.8.

The interaction of incident electron beam and sample causes losing energy of electron by scattering and absorption within interaction volume of the sample as presented in Fig. 3.9. Each type of signals can be detected by the specialized detector. In the imaging mode of FESEM or SEM, the secondary electrons are detected by the detector and form the surface images. The secondary electrons are ejected from the sample surface by inelastic scattering interaction with incident electrons. From the Fig. 3.9, the secondary electrons occurred near the sample surface about 10 nm in depth with the energy about 3-5 eV. However, the sample that is examined by FESEM or SEM must be electrically conductive in order to prevent electrostatic charge at the sample surface. On the other hand, for nonconductive specimen, they must be coated by electrically-conducting material

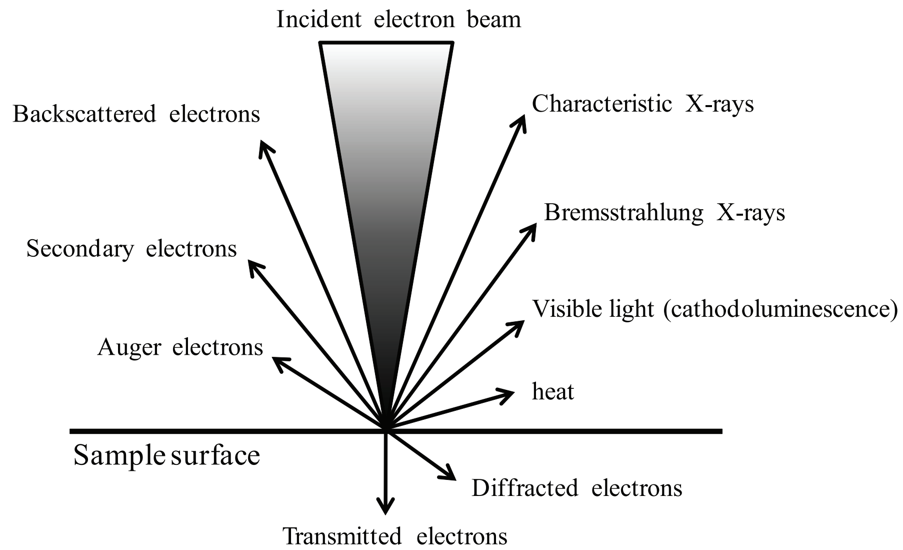

Figure 3.8: Interaction between sample surface and primary incident electron.

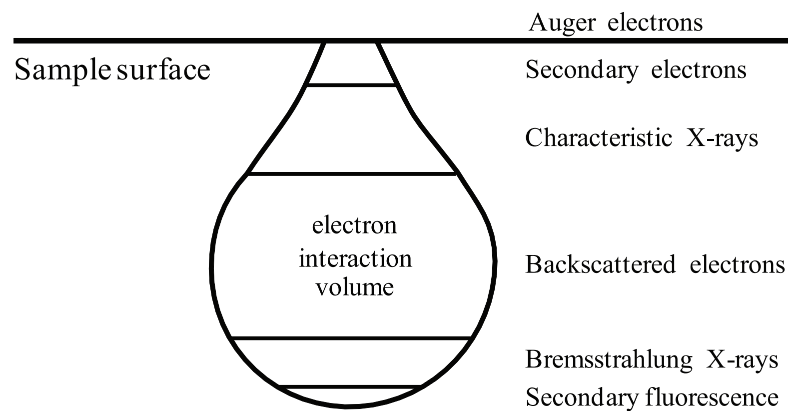

Figure 3.9: The interaction volume within a sample.

e.g. gold on the sample by sputtering process.

Energy dispersive X-ray spectroscopy (EDS or EDX) is an analytical technique used to identify the elemental composition of materials. EDS is attached to FESEM and SEM. The EDS technique detects the characteristic X-ray (see section 3.1) from the sample during bombardment by electron beam. Because the energy of X-ray are characteristic, the elemental compositions of the sample can be distinguished by observing the difference in X-ray energy values. The EDS spectrum is obtained by the plot of the intensity versus X-ray energy.

3.4 X-ray absorption spectroscopy

The X-ray absorption spectroscopy (XAS) is a characterization technique for determining structural information of the matter including local geometric and electronic structures. In the XAS experiment, a synchrotron light source is used as X-ray sources. A synchrotron light source covers all the wavelength of the electromagnetic spectrum with an intensity of 100 times higher than X-ray tube in X-ray diffraction instrument. The energy of synchrotron radiation can be tuned by using a crystalline monocromator to a range that incident photon can excite a core electron of absorbing atom to a continuum state. XAS can be operated in 2 modes which are transmission and fluorescence modes. Fig. 3.10 demonstrates the schematic diagram of XAS experiment. For the transmission mode, a monochromatic X-ray beam with intensity I_0 passing through the sample with thickness x. The transmission intensity after passing through the sample is

$$I_t = I_0 e^{-\mu x} \tag{3.3}$$

where: I_t is the intensity of transmitted X-rays,
I_0 is the intensity of incident X-rays,
μ is the absorption coefficient,
x is the thickness of the sample.

For the fluorescence mode, the detector will detect the fluorescent X-ray. The intensity of the fluorescent X-ray is

$$I_f \propto \mu I_0 \tag{3.4}$$

where: I_f is the intensity of fluorescent X-rays,
I_0 is the intensity of incident X-rays,
μ is the absorption coefficient.

From the XAS experiment, XAS spectrum is the plot between absorption (a.u.) and photon energy (eV). The increasing of the absorption energy in XAS spectrum is related to the absorption edges. The absorption edges are called in the order of increasing K, L_I, L_{II}, L_{III}, according to exited electron from 1s, 2s, $2p_{1/2}$, $2p_{3/2}$ to the continuum state, respectively (see Fig. 3.11). There are three region in XAS spectrum which are XANES, NEXAFS and EXAFS as seen in Fig. 3.12.

The X-ray absorption near edge structure (XANES) is the part of the spectrum that the energy of incident X-rays is high enough to move core electron to higher unoccupied valence states. XENES is mostly used to study information about the average oxidation states. The near edge X-ray absorption fine structure (NEXAFS) is the part of the spectrum that the electron is excited to the continuum. However, the kinetic energy of the photoelectron is low (10-40 eV) and the excite photoelectron is strongly backscattered by the neighboring atoms.

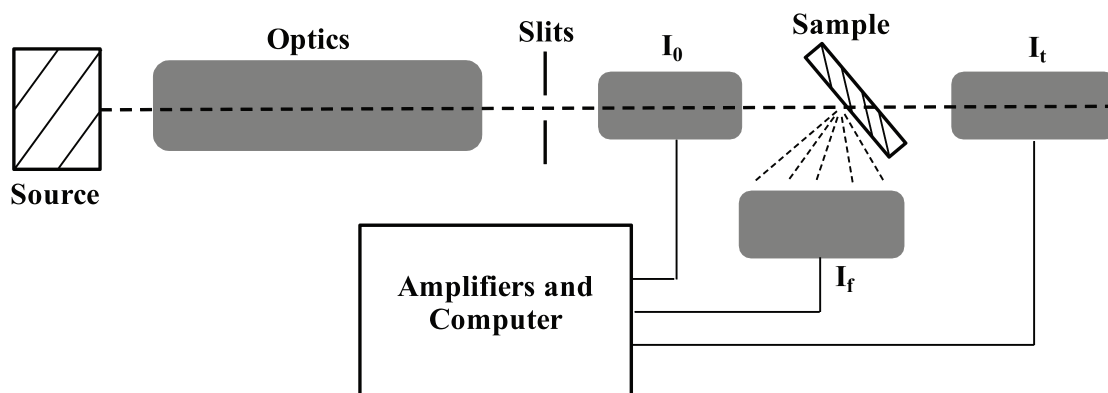

Figure 3.10: The schematic diagram of XAS experiment.

NEXAFS is used to study the number, kind of atoms close to absorber atom. The Fe atom behaved as absorber atom in this thesis. The extended X-ray Absorption fine structure (EXAFS) is the part of the spectrum that the kinetic energy of the photoelectron is high enough (50-1000 eV) that its wavelength can approximately compare with the distance to the neighboring atoms. EXAFS is used to study the number, kind and distances of the neighboring atom with each other and the absorber.

In this thesis, the fluorescent mode is used to investigate the oxidation state of Fe doping in the CCTO film deposited on si substrate.

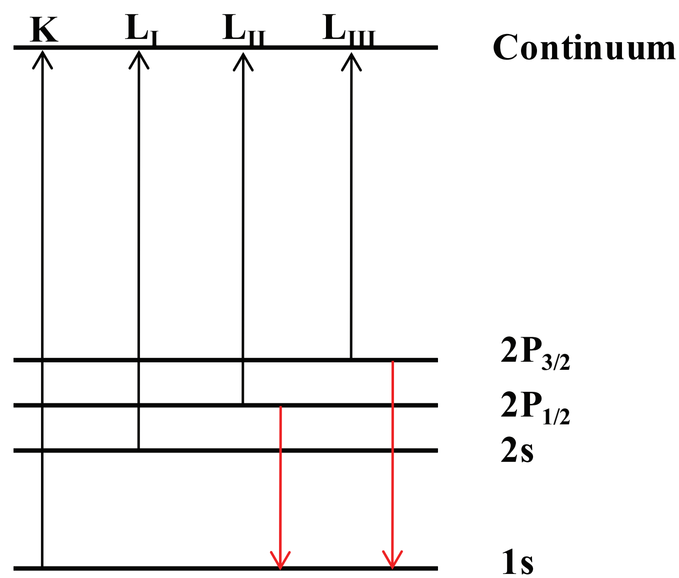

Figure 3.11: An example of absorption edges according to electronic transition (up arrows refer to X-ray absorption, down arrows refer to fluorescent X-ray emission).

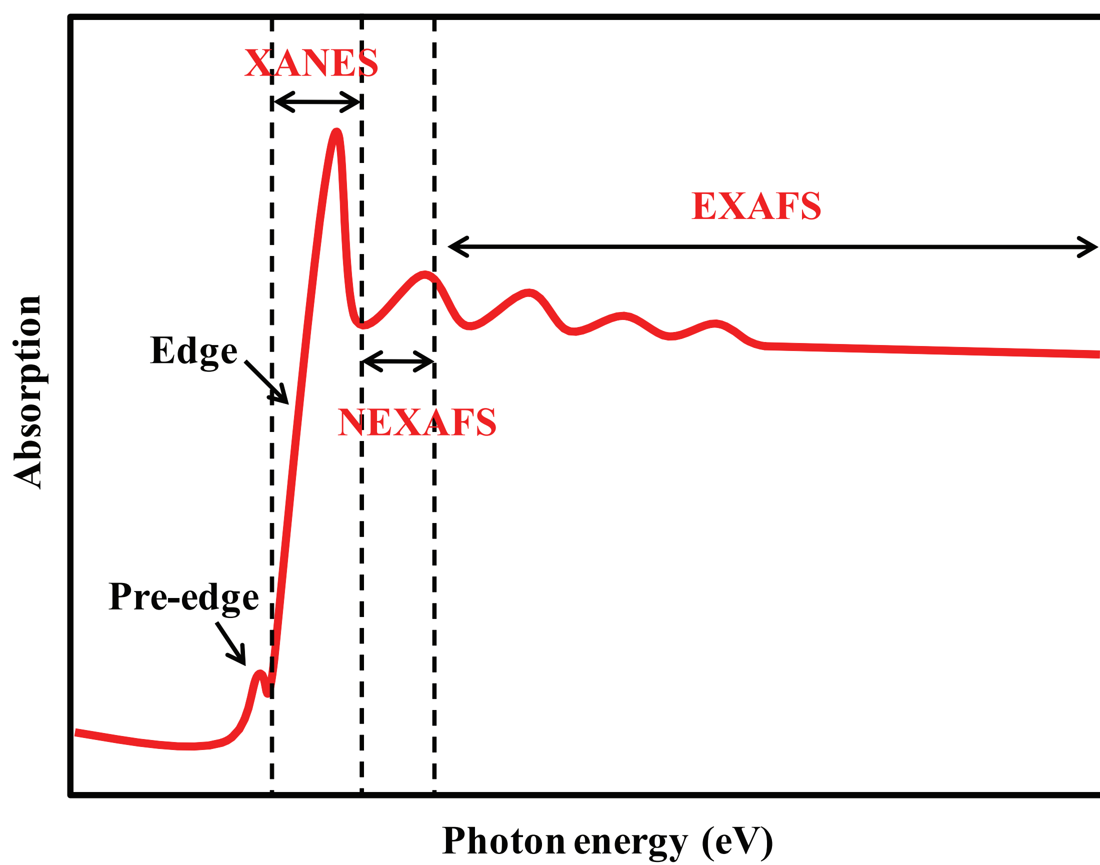

Figure 3.12: An example of XAS spectrum.

CHAPTER IV

EXPERIMENTAL METHODS

In this chapter, the experimental details are divided into three main parts. In the beginning of the chapter, I will focus on thin film synthesis by using a sol-gel technique. The CCTO and Fe-doped CCTO thin film characterization are explained including XRD, AFM, FESEM and XAS experiments. At the end of this chapter, the details of coplanar capacitor fabrication, the capacitance and loss tangent measurement as well as the conversion from capacitance to dielectric constant are explained.

4.1 CCTO thin film synthesis

4.1.1 CCTO and Fe-doped CCTO precursor preparation

The CCTO thin films were synthesized by a sol-gel technique. The starting materials were calcium acetate ($Ca(C_2H_3O_2)_2$), copper II acetate ($Cu(CO_2CH_3)_2$), titanium IV isopropoxide ($C_{12}H_{28}O_4Ti$), ethylene glycol ($C_2H_6O_2$) as well as formamide (CH_3NO) with A.R. purity. In the first step, calcium acetate was dissolved in acetic acid on a hot plate at 120 °C with stirring. Then, copper II acetate was added into it followed by the appropriate amount of titanium IV isopropoxide. Finally, ethylene glycol was added to increase the solution stability and formamide was added in order to reduce the viscosity of the solution to avoid the film cracking. In the Fe-doping process, iron II sulphate ($FeSO_4.7H_2O$) was added after dissolving copper II acetate with acetic acid. In this work, the Fe doping contents

were added as 4 wt%, 5 wt%, 6 wt% and 7 wt%, respectively (detail for Fe-doping see Appendix A). The flow chart of synthesis pure and Fe-doped CCTO precursor is shown in Fig. 4.1.

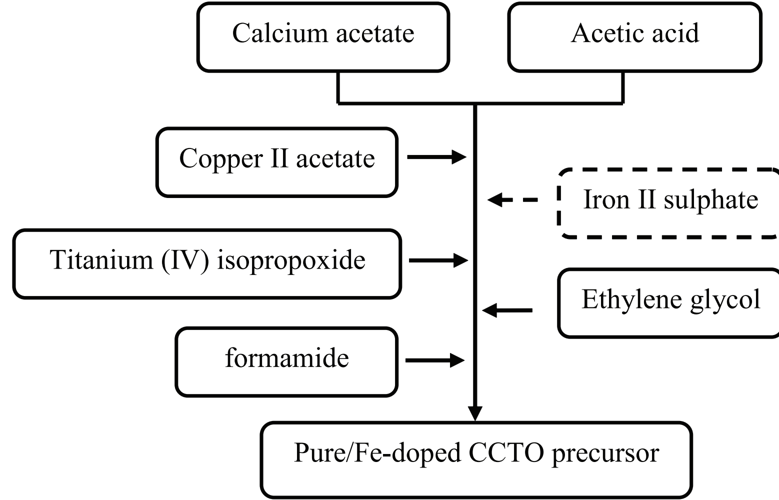

Figure 4.1: The flow chart of synthesis pure and Fe-doped CCTO precursor.

4.1.2 Substrate conditions and cleaning

Substrate cleaning is an important part for growing film with good quality. Before the substrate cleaning process is explained, I will briefly introduce substrate information which are used for coating CCTO films. Four different substrate types, Silicon wafer, Lanthanum aluminate, Neodymium gallate and Alumaina are used in this thesis. Silicon wafer (Si) with (100) orientation has a cubic structure with a lattice spacing of 5.43 Å and a thermal expansion coefficient of 4.05×10^{-6} K^{-1}. Table 4.1 shows other properties of Si single crystal substrate.

Lanthanum aluminate ($LaAlO_3$, LAO) with (100) orientation has a rhombohedral structure at room temperature and change a phase transition to the cubic perovskite structure at about 500-850 °C and it has twin structure which can be seen by naked eyes. A pseudocubic lattice parameter for LAO (100) is about 3.79 Å and the lattice mismatch between CCTO film and LAO substrate is 2.5%. Other properties of LAO single crystal substrate are illustrated in table 4.2

Table 4.1: Si Single Crystal Substrate Properties.

	Si Single Crystal Substrate Properties
Crystallographic structure:	Cubic a=b=c=5.43 Å
Twinning structure:	Twinfree
Color:	Dark gray
Density:	2.33 g/cm^3
Melting point:	1420 °C
Thermal expansion:	4.05×10^{-6} K^{-1}
Dielectric constant:	∼11.9 at 300K

Table 4.2: LAO Single Crystal Substrate Properties.

	LAO Single Crystal Substrate Properties
Structural type:	Distorted perovskite
Crystallographic structure:	Rhombohedral a=b=5.357 Å, c=13.123 Å
	α=β=60°, γ=120°
Twinning structure:	Orthogonal twin planes along (100)
Color:	light brown
Density:	6.52 g/cm^3
Melting point:	2080 °C
Thermal expansion:	1.0×10^{-5} K^{-1}
Dielectric constant:	∼25 at 300 K
Dielectric loss:	$\sim3\times10^{-4}$ at 300 K

Table 4.3: NGO Single Crystal Substrate Properties.

	NGO Single Crystal Substrate Properties
Structural type:	Distorted perovskite
Crystallographic structure:	orthorhombic
	a=5.426 Å b=5.496 Å c=7.707 Å
Twinning structure:	twinfree
Color:	light violet
Density:	7.56 g/cm^3
Melting point:	1605 °C
Thermal expansion:	0.9×10^{-5} K^{-1}
Dielectric constant:	~9 at 300 K
Dielectric loss:	~2-3$\times10^{-3}$ at 300 K

Table 4.4: Al_2O_3 Substrate Properties.

	Al_2O_3 Substrate Properties
Crystallographic structure:	Rhombohedral
	a=b=4.759 Å c=12.993 Å
Twinning structure:	Twinfree
Color:	white
Density:	3.85 g/cm^3
Melting point:	2052 °C
Thermal expansion:	8.2×10^{-6} °C^{-1}
Dielectric constant:	~9.8 at 300 K
Dielectric loss:	~ 2×10^{-4} at 300 K

Neodymium gallate ($NdGaO_3$,NGO) has a lattice parameter of about 3.86 Å. The lattice mismatch of the film and substrate is approximately 4.3%. The thermal expansion coefficient of NGO is about 0.9×10^{-5} K^{-1}. In this thesis, we used NGO substrates with (110) orientation. Some properties of NGO single crystal substrate are illustrated in table 4.3

Alumina (Al_2O_3) has a rhombohedral structure. Polycrystalline alumina is used in this work with the thermal expansion coefficient of 8.2 $\times10^{-6}$ $°C^{-1}$. Table 4.4 shows the summary of other properties for Alumina substrate.

Si single crystal substrates were used to investigate the optimum temperature for growing CCTO thin films condition. LAO and NGO single crystal substrates were used to deposit epitaxial films by a sol-gel process. Al_2O_3 substrates which are electrical insulator substrates were used to fabricate interdigitated CCTO thin film capacitor. All of the substrates were cut with a diamond pen approximately 1.5×1.5 cm^2 in size. Then, the substrates were cleaned by chemical process in order to remove the impurities such as dust and some particles that might be left from the cutting process before the coating process. The substrates were placed in a slotted teflon block, soaked in amount of acetone and placed in an ultrasonic bath for half an hour repeating two times in acetone. Then, the substrates were soaked again with an amount of methanol in ultrasonic bath and followed by deionize water. Finally, the substrates were dried by blowing with a 99.99% nitrogen gas.

4.1.3 Spin coating technique

After the synthesis of pure and Fe-doped CCTO are completed, each separate precursor was spun-coated on the substrate with the spinning speed of 2000 rpm for 40 sec by using spin coater (model P6700 series) as seen in Fig. 4.2. Then, the films were pre-heated at 120 °C for 20 min in order to dry the gel and remove remaining organic compounds. The films for each layer were annealed at 600-1000 °C (see the temperature profile in Fig. 4.3) for one hour in air atmosphere to form

a crystalline structure. This procedure was repeated for four times to obtained the films with 4 layers. The flow chart for the fabrication of pure and Fe-doped CCTO films are shown in Fig. 4.4. In this thesis, the pure and doped CCTO are deposited in the form of layers because in the work of Chang et al. revealed that the films with multi-cycle furnace annealing present less porous structure than single-cycle furnace annealing [34]. Multi-cycle furnace annealing was the same procedure of our film preparation with depositing one layer at a time followed by annealing for each layer.

Figure 4.2: Spin coater (SPIN COATER model P6700 series).

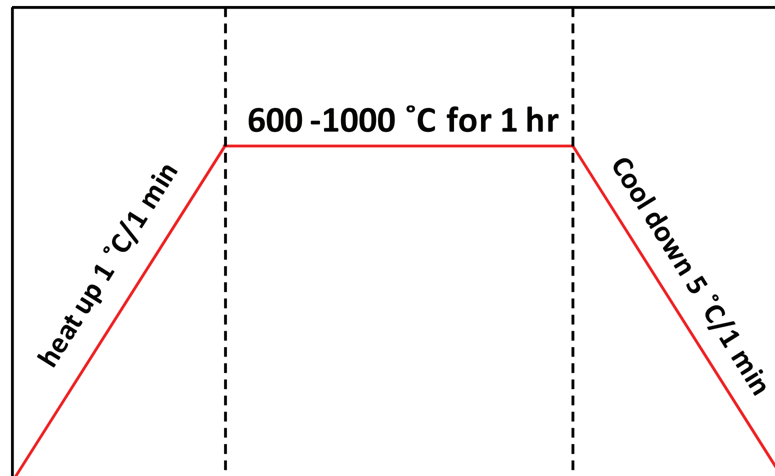

Figure 4.3: Temperature profile for annealing thin film.

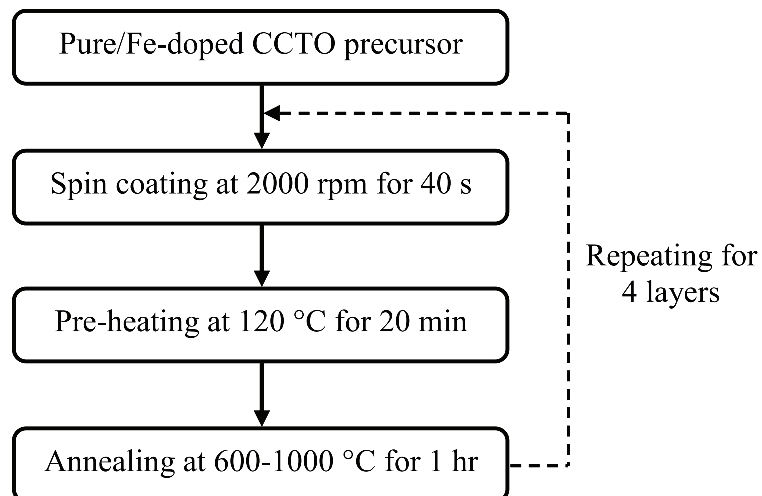

Figure 4.4: The flow chart for the fabrication of pure and Fe-doped CCTO films.

4.2 Thin film characterization

4.2.1 Crystal structure determination of the CCTO thin films

The crystal structure of the films was characterized by X-ray diffractometer (BRUKER model D8-Discover) (see Fig. 4.5) at Scientific and Technological Research Equipment Centre Chulalongkorn University (STREC). The X-ray measurement was collected by using $CuK_{\alpha1}$(λ =1.5406 Å) radiation with 40 kV and 40 mA in the 2θ range of 20° to 80° with scan step about 0.02°. The obtained X-ray data is the plot between 2θ and intensity. The (hkl) planes in X-ray data are compared with X-ray database (see Appendix B).

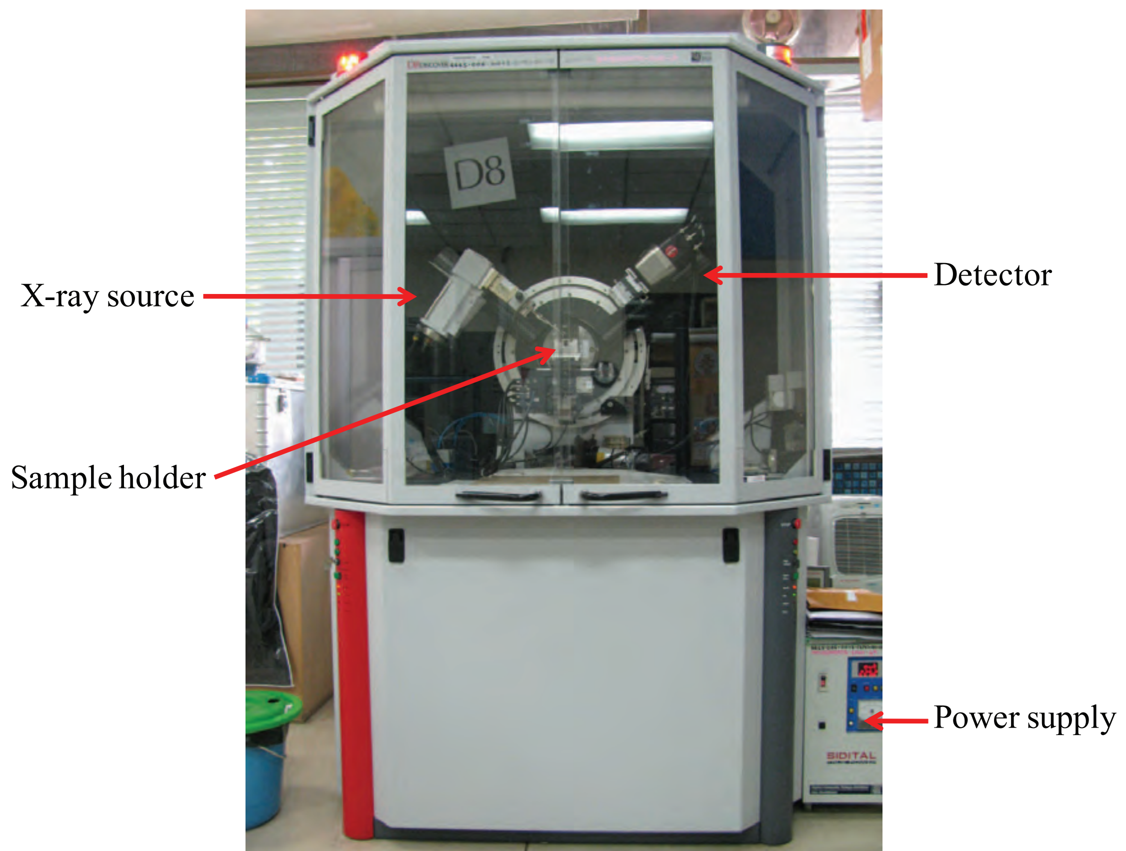

Figure 4.5: X-ray diffractometer (BRUKER model D8-Discover).

4.2.2 Surface morphology, grain size and surface roughness determination of the CCTO thin films

The surface morphology of the films was observed by Atomic force microscopy (Veeco model NanoScope IV) (see Fig. 4.6) at Scientific and Technological Research Equipment Centre Chulalongkorn University (STREC). The surface morphology including grain size study and surface roughness of the film was operated by using tapping mode with scanning size 2×2 μm^2.

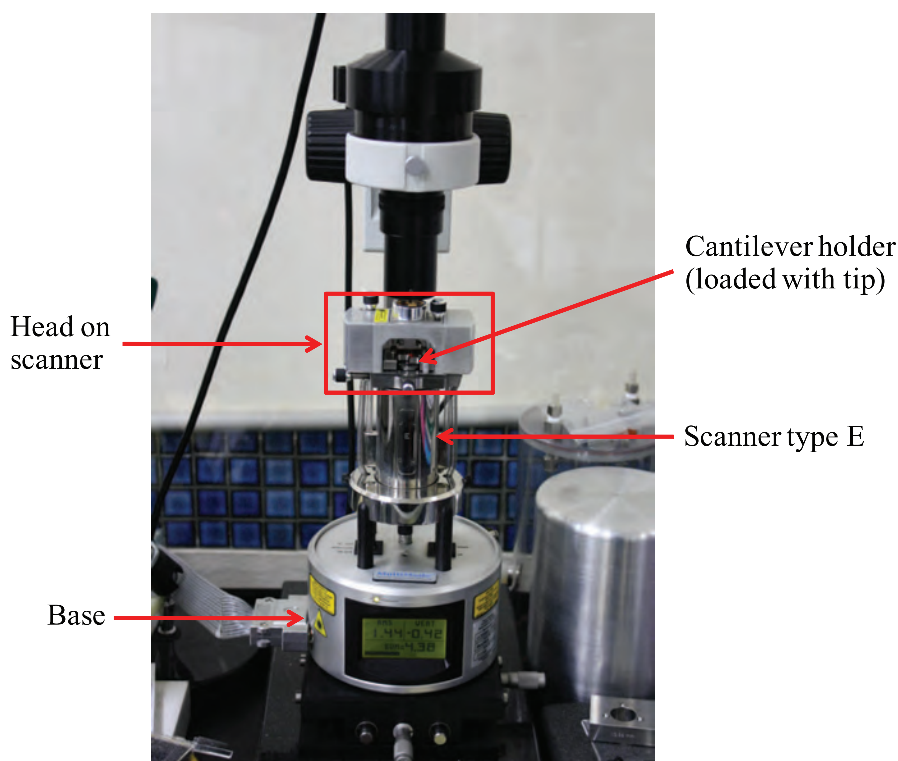

Figure 4.6: Atomic force microscope (Veeco model Nanoscope IV).

4.2.3 Surface morphology, cross section and elemental composition determination of the CCTO films

Field Emission Scanning Electron Microscopy (HITASHI model S-4700) was used to investigate the surface morphology as well as cross section of interface between the substrate and the sample. Before investigating, our films were glued

on a stub with a carbon tape and coated with gold on the sample surface by sputtering process to avoid the electrostatic charging at the sample surface. In our work, the measurement of FESEM was done at Thai Microelectronics Center (TMEC) located at Chachoengsao province.

The Energy Dispersive X-ray Spectroscopy (EDX) was used to examine the elemental composition of the CCTO film. The obtained energy from EDX result will be compared with the database. The sample for EDX analysis will not be coated by gold because the CCTO film itself is semiconducting material.

4.2.4 Determination of oxidation state of Fe ion

The oxidation states of Fe in our CCTO films were examined by X-ray absorption spectroscopy using synchrotron light source at beamline 8, Siam Photon Laboratory, Synchrotron Light Research Institute(Public organization) located at Nakhon Ratchasima province. Fluorescence mode XANES sprctra were recorded at room temperature. The Ge detector is used to detect the Fe K-edge X-ray absorption. For the focus, the beam dimensions were 19 mm $\times$ 1 mm. The sample size for XAS experiment was 1.5×1.5 cm^2 in order to receive the maximum X-ray beam.

4.3 Dielectric measurement

In this thesis, we measured the capacitance and dielectric loss of CCTO films using Impedance Analyzer (HP 4192A) as seen in Fig. 4.7. Prior to capacitance measurement, coplanar capacitors were fabricated in the form of interdigitated electrode on the top of the film by sputtering Ti and Au, respectively through the shadow mask. Since Au does not stick on any surface material, Ti is usually used to connect Au and the material. The interdigitated capacitors have been fabricated on the CCTO films. Since the patterning process was done on the

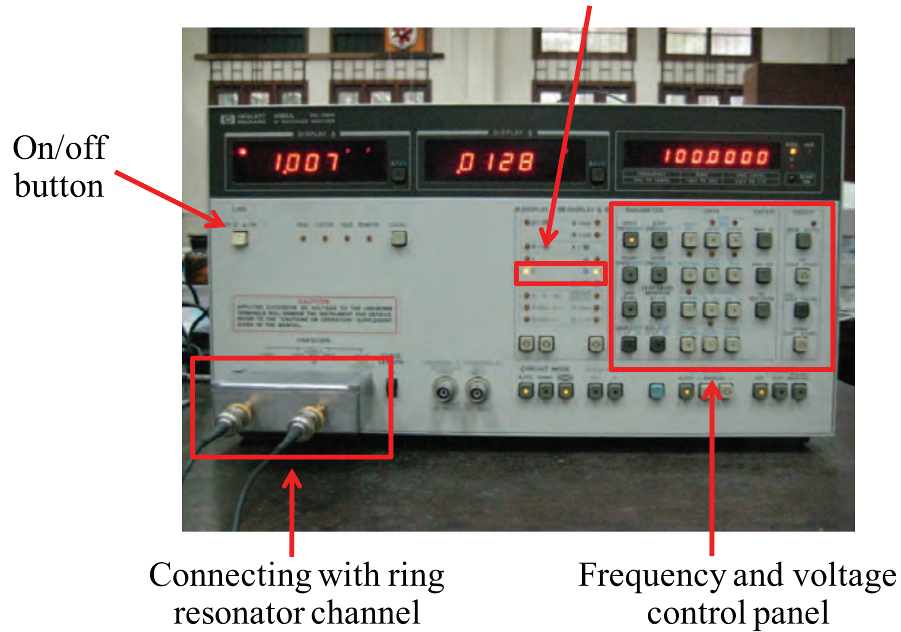

Figure 4.7: Impedance analyzer (HP 4192A).

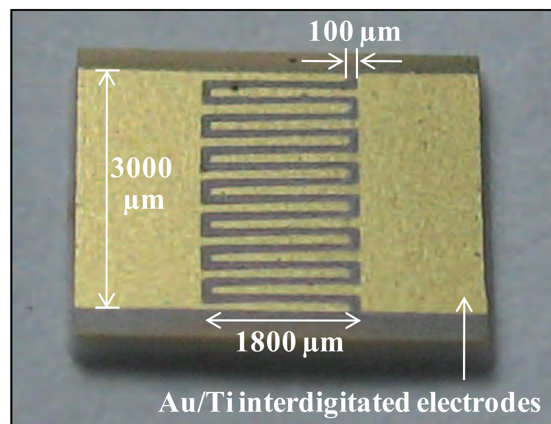

Figure 4.8: The image of CCTO interdigitated capacitor.

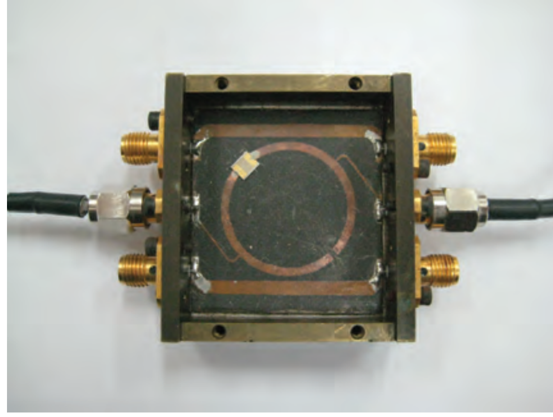

Figure 4.9: The CCTO interdigitated capacitor in a ring resonator.

whole piece of the substrate, a dicing saw was used to dice the sample to many individual capacitors. The overall size of the capacitor is about 2×3 mm^2 as seen in Fig. 4.8. The CCTO capacitors were mounted in a ring resonator by placing silver paint between the sample and resonator and let it dried as seen in Fig. 4.9. Then, the ring resonator box was connected to the impedance analyzer.

4.3.1 Conversion from capacitance to dielectric constant

From an Impedance Analyzer we obtained the capacitance and dielectric loss data of the CCTO films, the dielectric constant of the film in the form of coplanar capacitors can be calculated using the following expression [35]

$$\varepsilon_f = \varepsilon_s + \frac{C - K\left(1+\varepsilon_s\right)}{K\left(1-\exp\left(\frac{-4.6h}{G+W}\right)\right)} \tag{4.1}$$

where ε_f is the dielectric constant of the film,
ε_s is the dielectric constant of the substrate,
K is a constant depending on the size of gold finger in unit pF (see equation 4.3),
h is the film thickness,
G and W are the size of gold finger (see Fig. 4.10)

The value C is the measured capacitance per unit finger length per length of electrode, which is given by

$$C = \frac{C_m}{LN} \tag{4.2}$$

where C_m is the experimentally measured capacitance in unit pF,

L is the interdigitated finger length in unit m,

N is the number of gold finger of the electrode.

The constant K is defined by

$$K = 6.5\left(\frac{G}{G+W}\right)^2 + 1.8\frac{G}{G+W} + 2.37 \tag{4.3}$$

Equations 4.1-4.3 were derived by Farnell et al. [36] using an analytical model for interdigital electrode configuration as shown in Fig. 4.10.

In our work, the value of G, W, L and the thickness of the films obtained from FESEM measurement. The parameter G = 100 μm, W = 100 μm, therefore K = 4.535 pF. The number of fingers (N) is 14, the interdigital finger length is 1500 μm and the thickness of the film is approximately 500 nm.

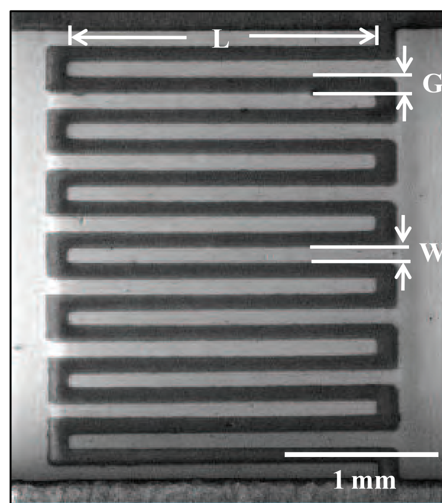

Figure 4.10: FESEM image of the interdigitated electrode.

CHAPTER V

RESULTS AND DISCUSSION

The results and discussions of the whole work are presented in this chapter. I will start with the effect of annealing temperature, different type of substrates and Fe doping on CCTO films, respectively. In the section 5.1, I will show the results and discuss the effect of annealing temperature on structural properties and surface morphology of CCTO films deposition on Si substrate. In section 5.2, the effect of substrates on these propertied will be discussed. The substrate types used to study in this thesis are silicon wafer, lanthanum aluminate, neodymium gallate and alumaina substrates. In the section 5.3, we studied the effect of Fe-doped on structural properties and surface morphology of CCTO films. Moreover, the results of electrical properties of CCTO film will be presented at the end of this chapter.

5.1 Effect of annealing temperature on structural properties and surface morphology of CCTO films

In this work, we synthesized the CCTO films by a sol-gel spin coating technique. The first part, CCTO films at different annealing temperature were deposited on Si substrates in order to find the optimum temperatures for the film growth condition. The CCTO films were annealed at 600-1000 °C temperature range. Fig. 5.1 shows the X-ray diffraction pattern of the CCTO films as a function

of annealing temperature.

For the CCTO film annealed at 600 °C does not exhibit any characteristic peaks of CCTO indicating that it has amorphous structure. As the annealing temperature increases to 700 °C, the TiO_2 and CaO peak occur at 27.4° and 37.0° diffraction angle, respectively. However, the unidentified peaks also occur at this temperature. When the annealing temperature is 800 °C, the CCTO film became polycrystalline and showed the characteristic peaks for (211), (220), (013), (222), (321), (400) and (422) planes. The three main peaks of CCTO which consist of (220), (400) and (422) planes appear with high intensities. All of the CCTO peaks were confirmed with the database [ICDD 01-075-2188] (see Appendix B). The peak positions at 27.4°, 36.0° and 54.3° indicated the diffraction plane of TiO_2. At the annealing temperature of 900 °C, the four TiO_2 peaks appear as seen as green plus sign and the (220), (222), (400) and (422) of CCTO peak occur. At 1000 °C, the peak intensities for CCTO decreased whereas for TiO_2 increased and also the unidentified peaks developed. The unidentified peaks also occur in previous study [37]. At the position of Si (400) planes in Fig. 5.1, there are the splitted peaks of $K_{\alpha 1}$ and $K_{\alpha 2}$ occurred even if $K_{\alpha 2}$ is filtered out. From this set of annealing temperatures we determine the optimum temperature for growing CCTO films to be 800 °C. The lattice parameter of CCTO thin films calculated by Bragg's expression at (220) plane with the maximum intensity is 7.380 Å are less than the value of bulk CCTO (7.391 Å).

The surface morphology of CCTO thin films at various annealing temperatures revealed by AFM are shown in Fig. 5.2. It is clearly seen that the average grain size of the film increases as the annealing temperature increases. The CCTO film annealed at 800 °C has an average grain size of about 50 nm (Fig. (a and b)) and increases to 130 nm and 400 nm for the film annealed at 900 °C (Fig. (c and d)) and 1000 °C (Fig. (e and f)), respectively. The increasing of the average grain size due to increase in temperature means an increase in kinetic energy of atoms so that atoms can diffuse and connect easily to form grains. At higher annealing temperatures, the atoms on the substrate have higher mobility and diffusion which

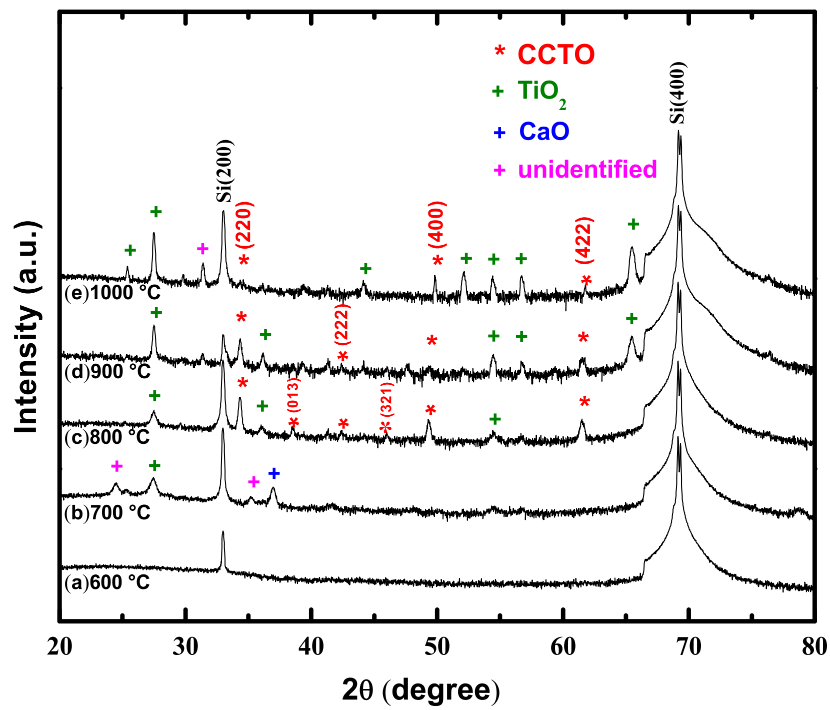

Figure 5.1: The XRD pattern of the CCTO films at various annealing temperature (a) 600 °C, (b) 700 °C, (c) 800 °C, (d) 900 °C and (e) 1000 °C.

are in line with the diffusion coefficient (D) [38]

$$D = D_0 \mathrm{e}^{\left(\frac{-E_d}{kT}\right)} \tag{5.1}$$

where E_d is the activation energy for diffusion,
k is the Boltzmann's constant,
T is the absolute temperature,
D_0 is the temperature-independent factor depending on the physical properties of the surface and of the particular materials involved.
The diffusion length is proportional to the diffusion coefficient. At high substrate temperatures, the mobility of ad-atoms on the substrate surface is normally increases so that the diffusion distance of the ad-atoms on the surface increase resulting in better growth of grains. At low temperatures, the ad-atoms do not have enough to overcome the potential energy of the nucleation sites of the substrate resulting in smaller grains. I observed the increase in grain size of CCTO on silicon substrate with increasing annealing temperature in accordance with the equation 5.1. Other works reported similar results of temperature dependence of grain size in various materials prepared by different growth techniques [39].

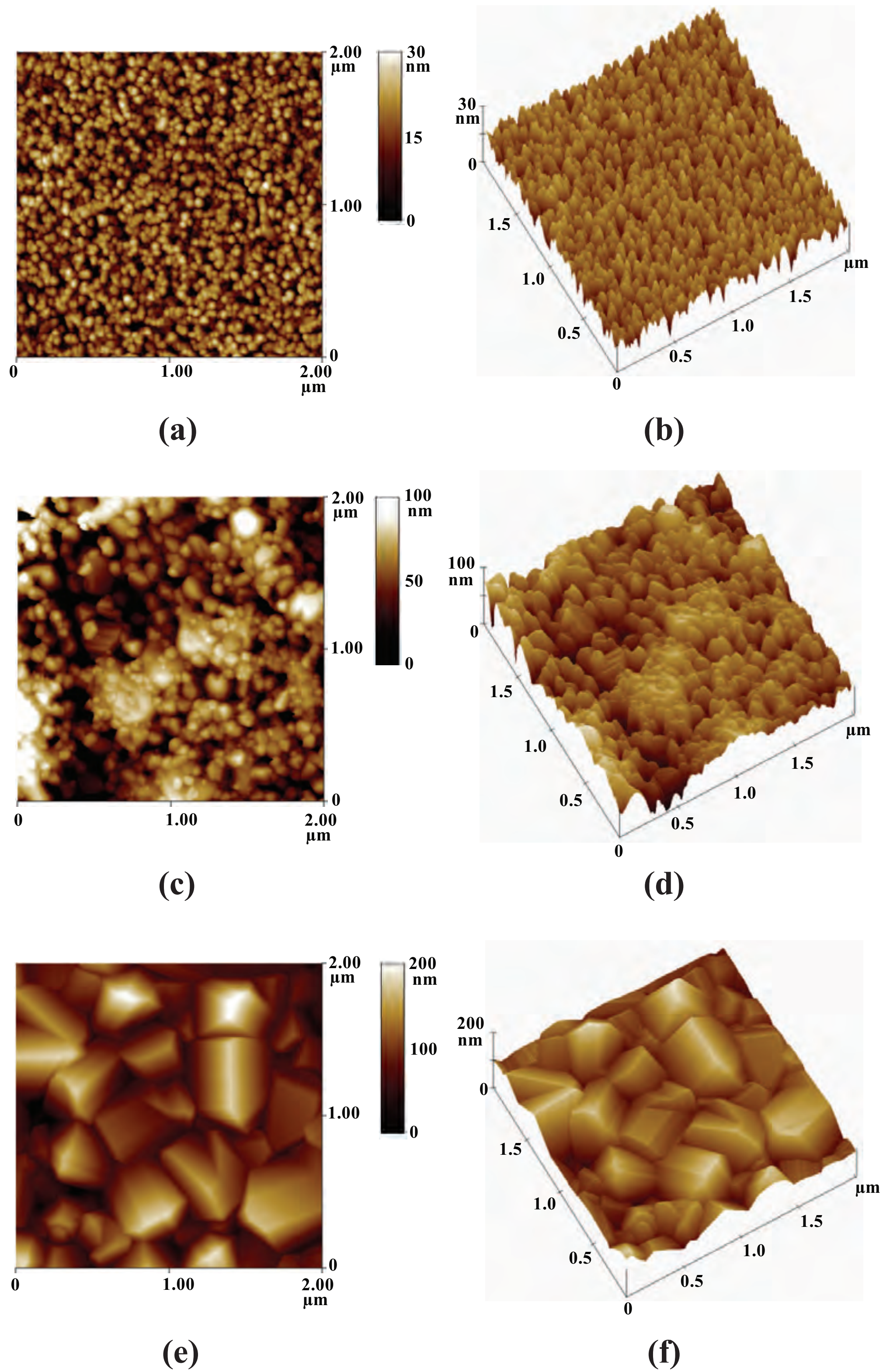

Figure 5.2: AFM images ($2 \times 2\ \mu m^2$) in 2D and 3D of the CCTO films deposited on Si substrate. (a) and (b) annealed at 800 °C, (c) and (d) annealed at 900 °C, (e) and (f) annealed at 1000 °C.

5.2 Effect of substrates on structural properties and surface morphology of CCTO films

As I mentioned in section 5.1, I have prepared CCTO films on Si substrate at the optimum temperature 800 °C by a sol-gel technique. The film grown on Si single crystal presents the polycrystalline film. Fig. 5.3 shows the XRD pattern of CCTO film deposited on Si substrate at 800 °C. We can see that the three main peaks (220), (400) and (422) appear with high intensities. From the line broadening of the XRD peaks, we calculated the particle size by using the Scherrer formula [40]. The particle size is found to be 36 nm for the film annealed at 800 °C. However, the average grain size of the CCTO film on Si obtained from AFM result is about 50 nm and the mean roughness is about 4.674 nm as seen in Fig. 5.4(a) and (b).

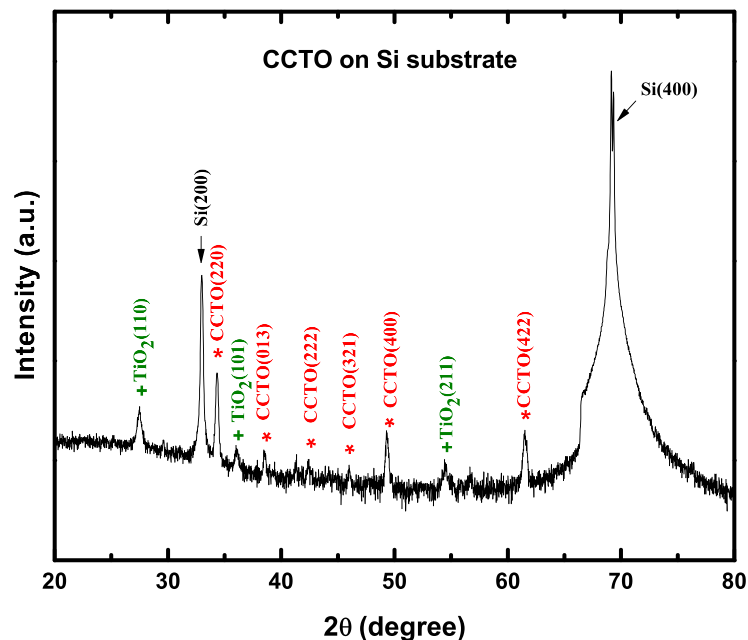

Figure 5.3: The XRD pattern of the CCTO film deposited on Si substrate annealed at 800 °C .

Morphology and microstructure of the CCTO films obtained from FESEM are shown in Fig. 5.5. Fig. 5.5(a) shows the surface morphology of CCTO film deposited on Si substrate annealed at 800 °C. The grains present in sponge-like shape with approximately grain size of 58 nm. The thickness of the film is approximately 400 nm as shown in Fig. 5.5(b). There are many voids observed in the films. The amount of voids that observed in the film depends on the film preparation. I will give some examples I have found from literature reviews. For example, in the work of Chang et al [34], they prepared the CCTO film in two different methods. The first one is single-cycle furnace annealing (SFA) at which the films were spun and preheated then these two processes were repeated before annealing in the furnace only once. The second one is multi-cycle furnace annealing (MFA) at which the films were spun, preheated and annealed in the furnace and the whole process was repeated several times to obtain the film with the desired thickness. They found that the films that prepared by SFA method showed many voids than in the film prepared by MFA method. Liu et al [4]. have found that a few pores were present in the film with large grains; smaller grains were combined to form large grains at higher temperature. For the interface between substrate and film, near the substrate surface the CCTO film show more dense grains than the upper layer film as seen in Fig. 5.5(c).

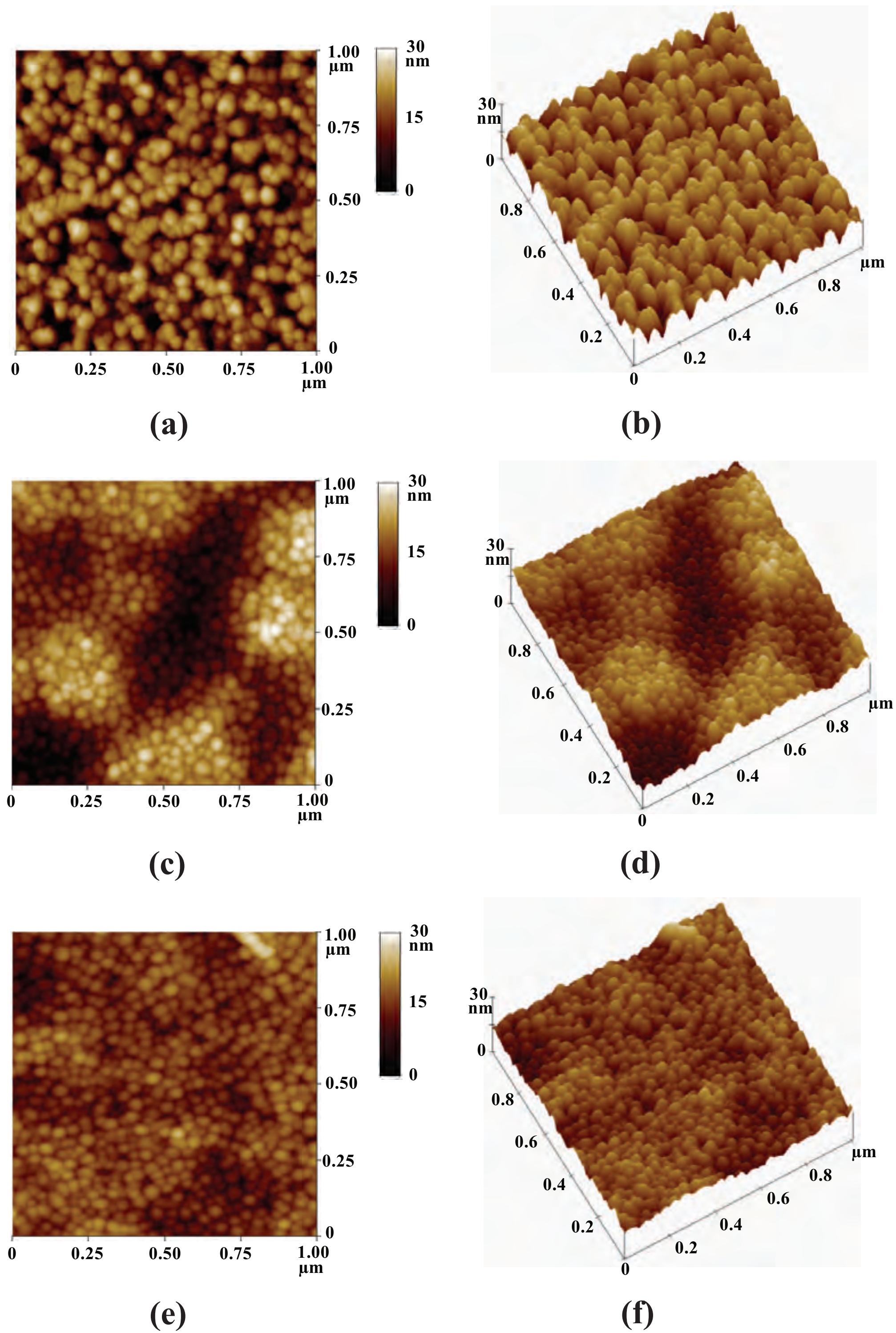

Figure 5.4: AFM images (1×1 μm^2) in 2D and 3D of the CCTO films deposited on (a) and (b) Si substrate, (c) and (d) LAO substrate, (e) and (f) NGO substrate.

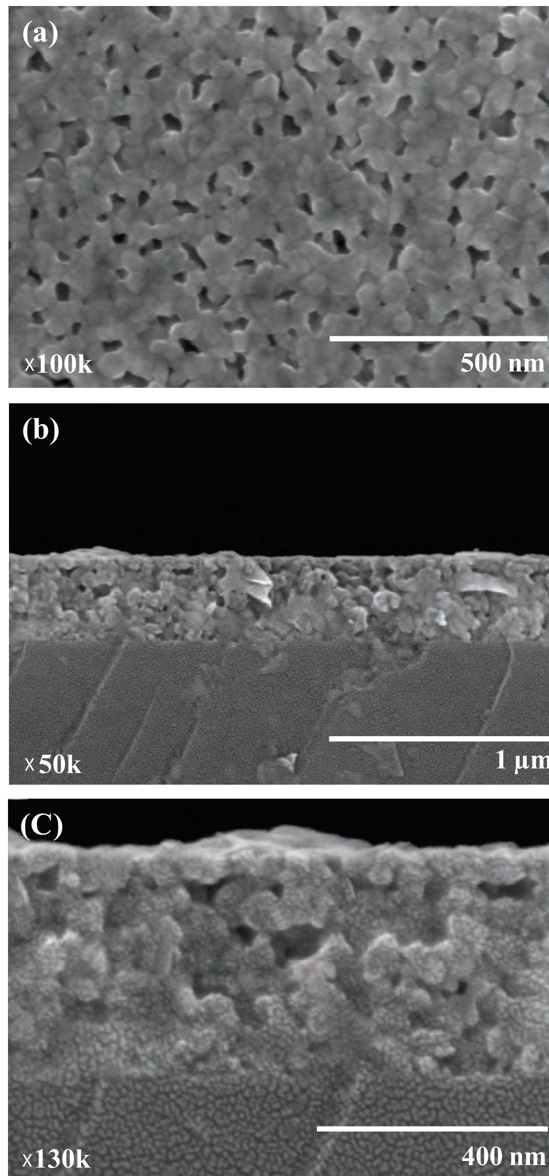

Figure 5.5: FESEM micrograph of the CCTO film deposited on Si substrate at 800 °C (a) plane view, (b) cross section and (c) the zoom of interface between the CCTO film and Si substrate surface.

Fig. 5.6 presents the XRD pattern of the CCTO film grown on LAO single crystal substrate annealed at 800 °C. The CCTO film deposited on LAO substrate tends to be an epitaxial film because of having small lattice mismatch between the film and substrate about 2.5%. The lattice mismatch is defined as the ratio of the difference in the lattice parameter between the film and the substrate and the lattice parameter of the substrate. Thus, the calculated lattice mismatch of the CCTO film and LAO substrate is $\frac{|3.790-3.696|\mathring{A}}{3.790\mathring{A}} \times 100 = 2.5\%$, which is considered to be a small lattice mismatch. The (400) and (600) peaks of CCTO are obviously seen while (200) peak is expected to be seen but it overlaps with LAO (100) substrate peak. However, the TiO_2 peak is observed at different diffraction angles from the film grown on Si substrate. The TiO_2 peak is comparable to the standard powder XRD pattern of TiO_2 for (004) plane in the JCPDS card No.03-065-5714. The lattice parameter of the CCTO film on LAO substrate is about 7.391 Å, consistent with the previous report for the CCTO film grown on $SrTiO_3$ (100) single crystal substrate [22]. The locations of atoms, Ca^{2+}, Cu^{2+}, Ti^{4+} and O^{2-} which are expected to fall on top of LAO crystal structure are shown in Fig. {fig:LAO100CCTO. The CCTO film grown on LAO shows {200} preferred orientation with the ratio I_{400} to I_{600} about 1.63. The particle size from the line broadening is about 24 nm. Fig. 5.4(c) and (d) illustrate the AFM images of surface morphology of CCTO film on LAO substare. The grain size of the CCTO film obtains from AFM is about 43 nm. The mean roughness is about 3.867 nm.

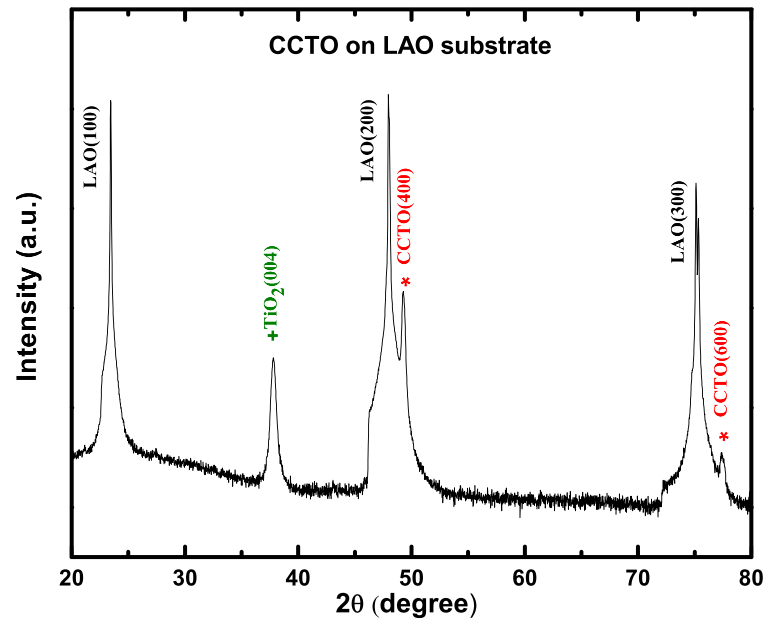

Figure 5.6: X-ray diffractogram of CCTO film deposited on LAO substrate at 800 °C .

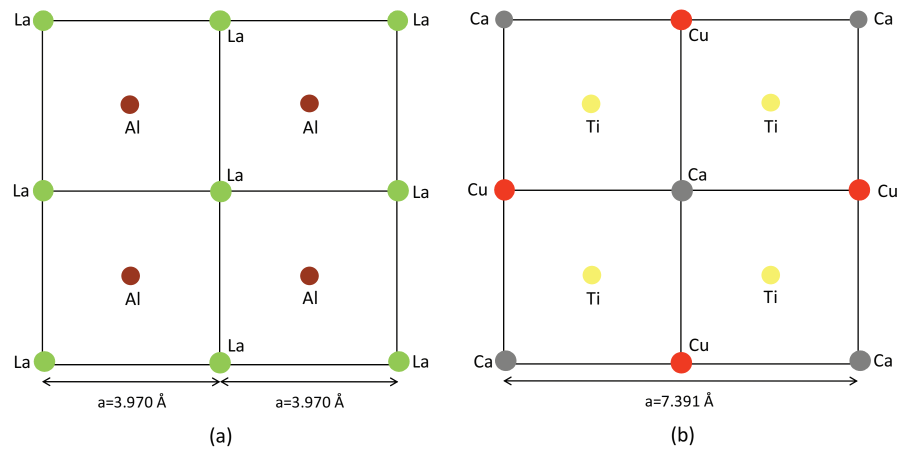

Figure 5.7: The plane view of locations of atoms in (a) LAO (100) substrate (b) CCTO (200).

Fig. 5.8 shows the FESEM images of the CCTO film grown on LAO substrate annealed at 800 °C. The FESEM result shows the round shape of grain with size of 40 nm. Comparison of the cross section of the CCTO film grown on Si and LAO substrate, the thickness of the film grown on LAO substrate is 490 nm which is thicker than the film grown on Si substrate. As we can see in Fig. 5.8(b) and(c), The CCTO film grown on LAO is more dense and presents less porous than the film grown on Si substrate.

Before growing the CCTO film on NGO substrate, I expected that the film grown on NGO is epitaxy film as well as the film grown on LAO due to small lattice mismatch about 4.2% [Lattice mismatch = $\frac{|3.860-3.696|\mathring{A}}{3.860\mathring{A}} \times 100 = 4.2\%$] which is less than 5%. The structural properties of the CCTO film deposited on NGO single crystal substrate revealed by XRD pattern is shown in Fig. 5.9. As contradict to my expectation, the CCTO characteristic peaks appeared at (220) and (222) planes not only 200 family plane consisting of (200),(400) and (600). If compared with the result of the film grown on LAO, the lattice mismatch of the film grown on NGO higher than the film grown on LAO about two times resulting in appearing of (220) and (222) CCTO characteristic peaks. However, the intensities of the {200} are much higher than the (220) and (222) planes. Also, I found that the intensities of (220) and (222) peaks of the film on NGO are much weaker than that of the film on Si. The ratio $I_{(400)}/I_{(600)}$ is 1.65, that means the CCTO film on NGO substrate shows {200} prefer orientation. The lattice parameter of the CCTO films grown on NGO substrate is about 7.390 Å which is close to that of the CCTO bulk. However, the (100) and (004) planes of TiO_2 exist in the film. Fig. 5.10 shows the locations of atoms, Ca^{2+}, Cu^{2+}, Ti^{4+} and O^{2-} which are expected to fall on top of NGO crystal structure. The particle size of the film grown on NGO obtained from the line broadening of the main peak using Scherrer formula equals to 27 nm. The surface morphology of the CCTO film deposited on NGO with grain size about 42 nm is demonstrated in Fig. 5.4(e) and (f) and the roughness of the film is approximately 2.281 nm.

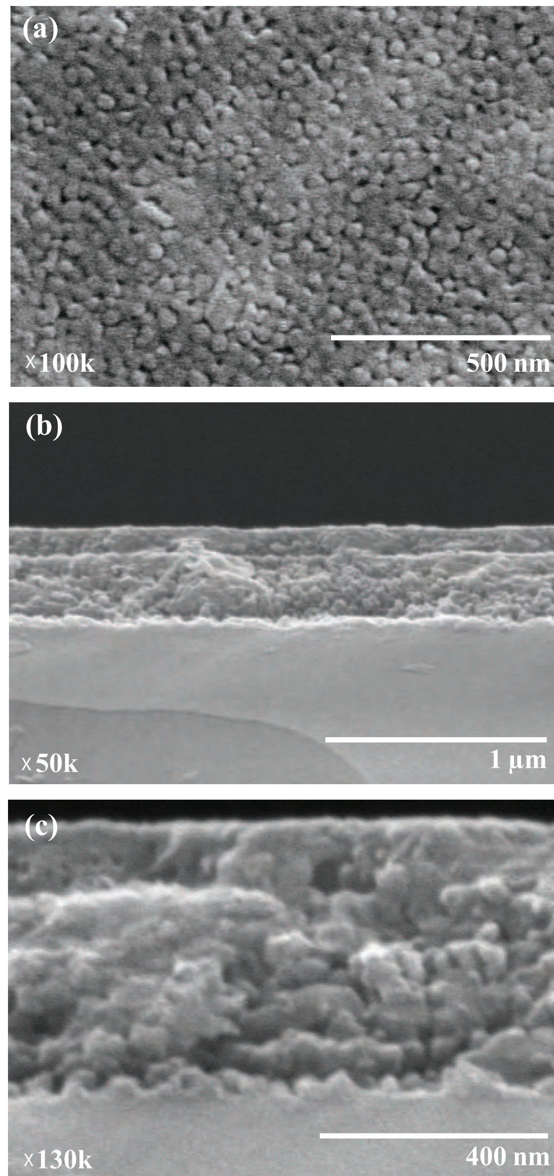

Figure 5.8: FESEM images of the CCTO film grown on LAO substrate at 800 °C (a) plane view, (b) cross section and (c) the zoom of interface between the CCTO film and the LAO substrate surface.

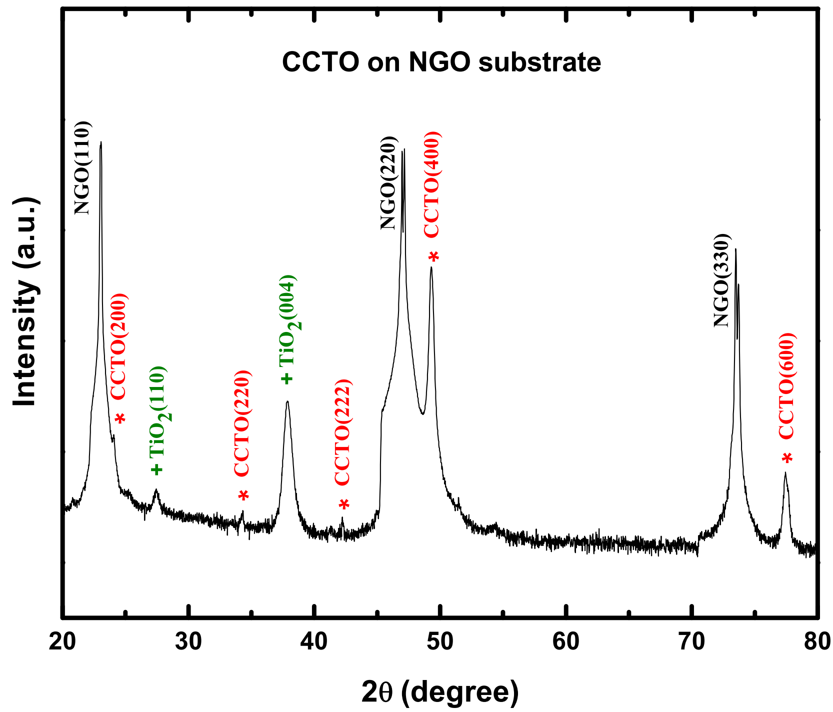

Figure 5.9: XRD spectra of the CCTO film grown on NGO substrate at 800 °C .

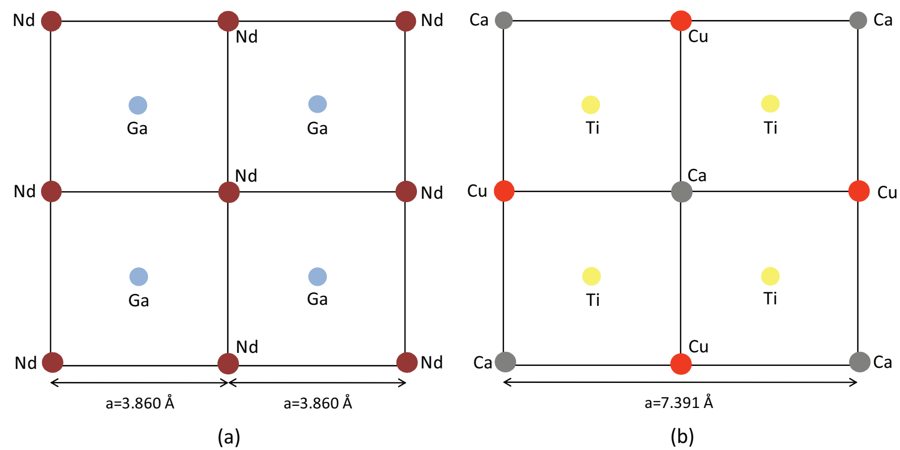

Figure 5.10: The plane view of locations of atoms in (a) NGO (110) substrate (b) CCTO (200).

As mentioned earlier, the rms roughness of the films deposited on different substrates including Si, LAO and NGO substrates are approximately 4.674 nm, 3.867 nm and 2.281 nm, respectively. The differences in roughness among these films are small, on the order of less than 5 nm. For the sake of comparison, the average roughness for cleaned single crystal substrates is about 1 nm [41]. This result indicate that the film surface morphology with the size of 1x1 μm^2 of our films at this film growth condition is rather uniform. The film on NGO showed the lowest rms value, as compared with LAO owning twin structure which might affect the resulting rms of the film. However, this is only my expectation because this is contradict with the result of the interface between the substrate and the film. The CCTO film at the interface is dense with less voids that those found in NGO. In order in conclude this, further investigation was need to be one would rather do more AFM measurements on several spots and the average rms has to be obtained from the first layer of deposition as well.

Fig. 5.11 presents the FESEM image of CCTO film grown on NGO substrate. Fig. 5.11(a) shows the surface morphology of CCTO film on NGO substrate. The grain has a round shape with size about 44 nm. The grain shapes of the film deposited on NGO and LAO are nearly the same while the grain shape of the film deposited on Si is sponge-like shape. The thickness of the film is approximately 438 nm. It is clearly seen that there are many porous structure in CCTO film on NGO. The interface between CCTO film and substrate is shown in Fig. 5.11(c). Near the substrate surface, there are more porous structure compare to the CCTO film on LAO and Si substrates.

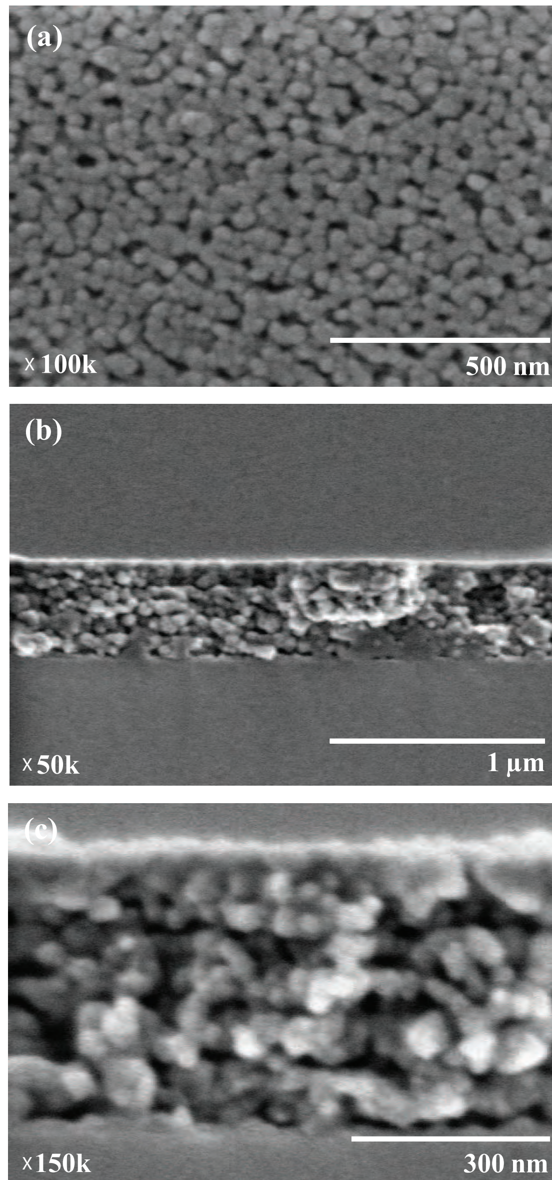

Figure 5.11: FESEM microstructure of the CCTO film deposited on NGO substrate at 800 °C (a) plane view, (b) cross section and (c) the zoom of interface between the CCTO film and the NGO substrate surface.

Table 5.1: Summary of the CCTO peak analysis and lattice parameter obtained from XRD.

CCTO film grown on	CCTO (220)	CCTO (400)	CCTO (600)	$I_{(400)}/I_{(220)}$	$I_{(400)}/I_{(600)}$	lattice parameter
Si	seen	seen	unseen	0.79	-	7.380 Å
LAO	unseen	seen	seen	-	1.63	7.391 Å
NGO	slightly seen	seen	seen	1.92	1.65	7.390 Å

Table 5.1 illustrates the summary of the XRD peaks, the main characteristic peak of the film deposited on Si substrate is (200) plane while on LAO and NGO are (400) plane. Similarly, the film grown on LAO and NGO showed the (600) plane with high intensity, however, the (600) for the film grown on Si could not be found. From table 5.1, the intensity ratio of the (400) plane to (600) plane are 1.63 and 1.65 for the film deposited on LAO and NGO, respectively. For the film grown on Si and NGO substrates the ratio of $I_{(400)}$ to $I_{(200)}$ are 0.79 and 1.48, respectively. As expected, the substrate have an impact on the characteristic peaks of CCTO thin films. We can see that the CCTO films deposited on LAO and NGO show the lattice constant about 7.391 Å and 7.390 Å, respectively which consistent with bulk CCTO result (7.391 Å). However, the lattice constant of the film deposited on Si is 7.380 Å which less than that of the bulk CCTO value.

5.3 Effect of Fe-doping on structural properties and surface morphology of CCTO films

The structural properties, surface morphology and element composition of pure and Fe-doped films were characterized by using X-ray diffraction and Field emission scanning electron microscope, respectively. The existing of Fe-doping in the films was confirmed by X-ray absorption spectroscopy. Fig. 5.12 shows the

XRD pattern of pure and Fe-doped CCTO films annealed at 800 °C with different iron contents (4-7 wt% Fe-doped) grown on Si substrates. The characteristic peaks of CCTO were preserved as long as the concentration of the Fe-doped not exceed 6% by weight. We can see that the peaks intensities for Fe-doping decreases compared to undoped films. The Fe-doped films present only the three main peaks of CCTO (220), (400), and (422) planes. As the Fe concentration increased to 7% by weight, the main CCTO peaks disappeared, but the TiO_2 peaks remain only.

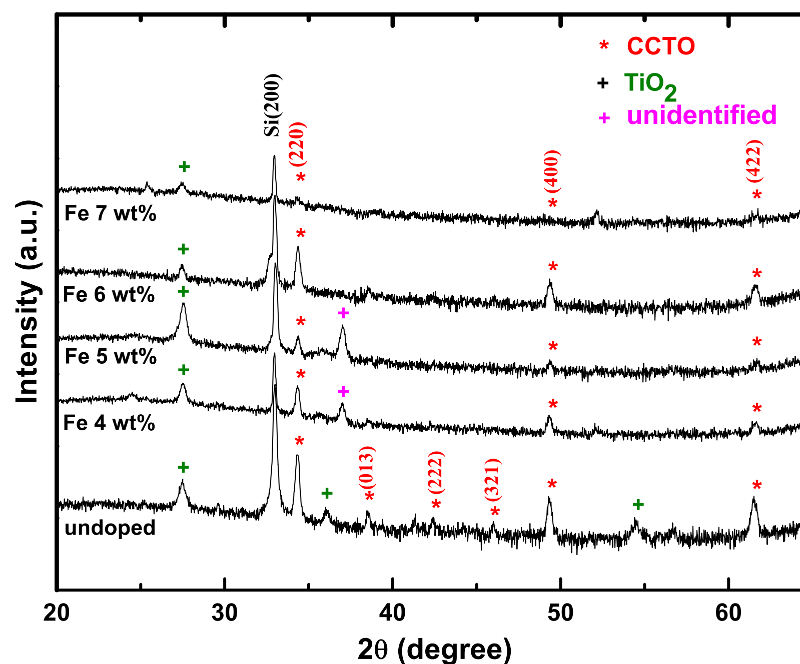

Figure 5.12: The XRD spectra of pure and Fe-doped CCTO films with various Fe concentrations deposited on Si substrates at 800 °C .

Fig. 5.13 illustrates the FESEM images of the surface morphology and the thickness of the film annealed at 800 °C with different Fe concentration. It is clearly seen that the grains are homogeneous in sponge-like shape but different in size. The average grain size decrease as the Fe contents increase except the film with Fe doped 7 wt%. The cross sectional images show the thickness of the film increase from 429 nm to 544 nm from the Fe content of 4 to 7 wt%. The

viscousness of the precursor with more Fe concentration is more viscous than the precursor with low Fe concentration. So that the film with more Fe contents present high thickness than the film with low Fe contents. Fig. 5.14 shows the Fe K-edge XANES spectra of Fe-doped CCTO films with various Fe contents and inset shows the expanded of pre-edge region. The pre-edge energy of our film is approximately 7113.5 which means the existence of Fe^{3+} oxidation state in our film [42]. A pre-edge peak in transition metal K-edge spectra is typically due to 1s state to 3d state transition [43]. From Fig. 5.14, the intensity and absorption K edge energy was increased with increasing Fe contents in the film. K edge represents the transition from the 1s electronic core state to the unoccupied state above the Fermi level. The absorption K edge energy was increased about 7124.3 eV, 7128.3 eV and 7130.3 eV with the increasing Fe-doped of 5 wt%, 6 wt% and 7 wt%, respectively [44]. Table.5.2 shows the elemental composition of the pure and Fe-doped CCTO obtained from EDS experiment. The nominal ratio of element composition of CCTO for Ca:Cu:Ti:O is 1:3:4:12. The Ca:Cu:Ti:O of our pure CCTO is 1:1.5:5.2:10.3 indicating the excess Ti and the insufficient Cu and O constitutions. The excess of Ti obtained from EDS consistent with the TiO_2 phase formation in XRD result. As expected, the Fe^{3+} in our film substituting for Ti^{4+} site because of their compatible radius (Ti^{4+} = 0.68 Å and Fe^{3+} = 0.65 Å) [45] which can be examined by EDS as seen in table.5.2. The increase in Fe ion substituting for Ti ion can be observed when the weight percentage of iron was added in the solution during the preparation.

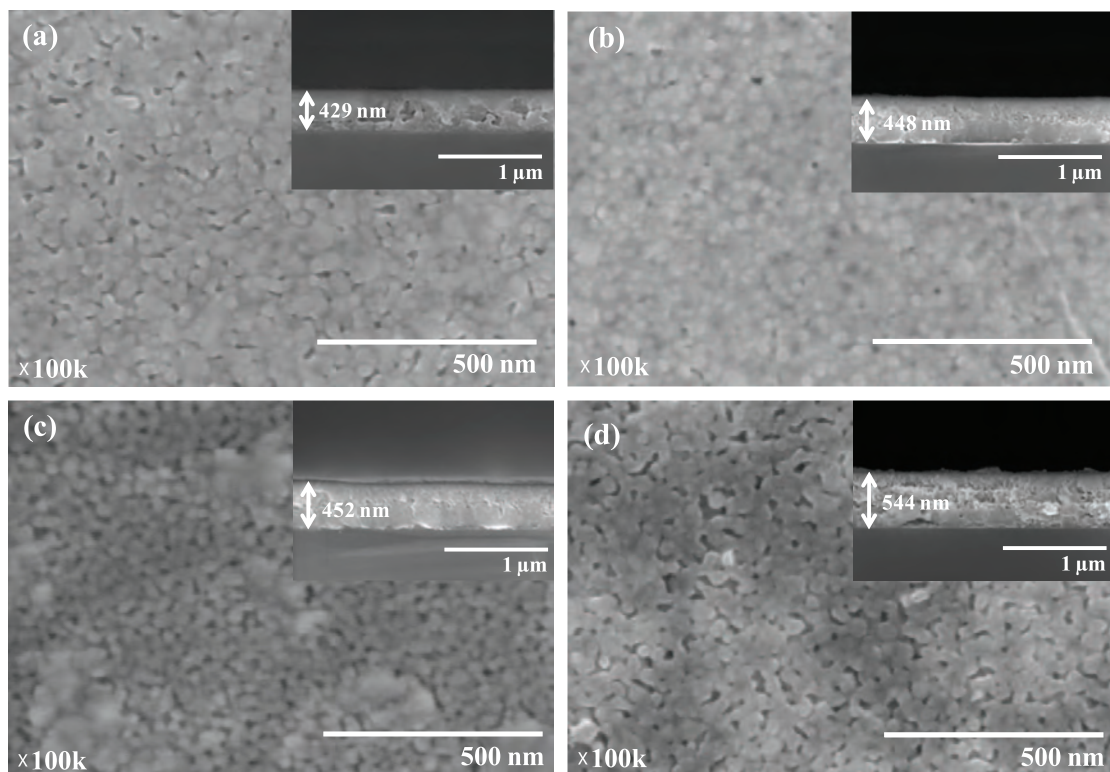

Figure 5.13: The FESEM surface morphology of CCTO films deposited on Si substrates at 800 °C with different Fe concentrations (a) 4 wt%, (b) 5 wt%, (c) 6 wt% and (d) 7 wt% .

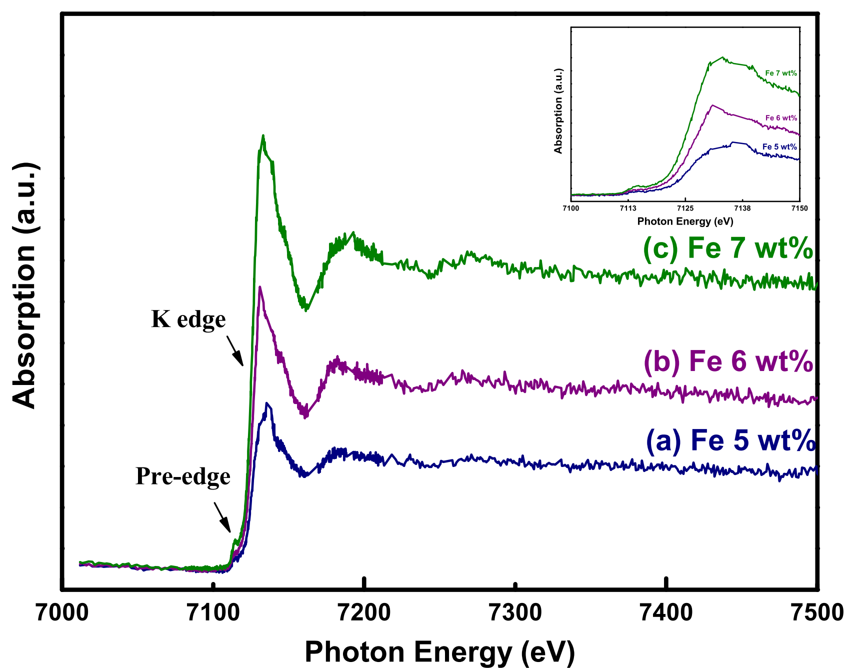

Figure 5.14: The XANES spectra of Fe-doped CCTO films deposited on Si substrates at 800 °C with different Fe concentrations and the zoom of pre-edge region (inset).

Table 5.2: The stoichiometry of pure and Fe-doped CCTO films with different Fe contents.

	Stoichiometry
Pure CCTO	$CaCu_{1.5}Ti_{5.2}O_{10.3}$
Fe 4 wt%	$CaCu_{1.5}Ti_{3.6}Fe_{0.4}O_{8.6}$
Fe 5 wt%	$CaCu_{1.5}Ti_{3.5}Fe_{0.5}O_{8.9}$
Fe 6 wt%	$CaCu_{3}Ti_{3.4}Fe_{0.6}O_{9.4}$
Fe 7 wt%	$CaCu_{3}Ti_{3.2}Fe_{0.8}O_{10.5}$

5.4 Electrical properties of CCTO films

In this thesis, the electrical properties of the CCTO films were obtained from the CCTO films deposited on alumina and NGO substrate. In section 5.2, we have shown the structural properties of the CCTO film grown on NGO substrates. In this section, the structural properties of the CCTO film grown on alumina substrate is presented and compared with that of NGO. Alumina substrates are known as insulating cheap substrates to fabricate microelectronic devices. In order to fabricate coplanar capacitors, the whole peice of substrate needs to be insulator. This is why I did not use the CCTO film on silicon substrate to make coplanar capacitor even though there are some thin layers of SiO_2 on Si. NGO substrates are very pricy, for example, one piece of NGO substrate with 2 inches diameter size costs about $1000. For the comparison, one piece of LAO substrate with the same size costs around $500 which is twice cheaper than the price of NGO substrate. Unfortunately, I did not have coplanar capacitors on CCTO film on LAO substrate due to the failure in the electrode patterning process. But the benefit of using NGO substrates is that NGO are single crystal substrates as compared with alumina which is polycrystalline substrate. As I have planned, there will be a comparison of dielectric responses between the crystalline film on Al_2O_3 and almost epitaxy film on NGO. Fig. 5.15 presents the XRD spectra of CCTO thin films grown on alumina substrate annealed at 800 °C. All CCTO diffraction peaks grown on alumina substrate appeared at the same peak positions as the film grown on Si (100) substrate. The lattice constant of the CCTO film deposited on alumina calculated from (220) peak is about 7.391 Å. Note that the lattice constant of the CCTO film on alumina is close to those of CCTO on NGO (7.390 Å) and CCTO on LAO (7.391 Å) but is larger than that of CCTO on silicon (7.380 Å). The surface morphology of the film grown on alumina substrate is shown in Fig. 5.16 (a). The average grain size and the rms roughness of the film are approximately 34 nm and 3.645 nm, respectively. For the CCTO film on NGO substrate, the grain sizes are nearly the same and the shape of the grains are

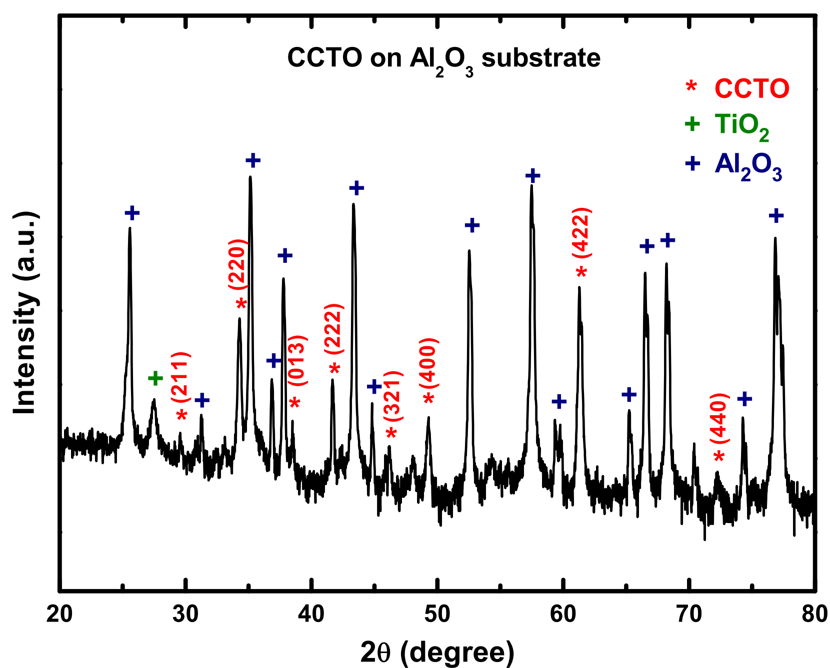

Figure 5.15: XRD spectra of the CCTO thin film on alumina substrate annealed at 800 °C.

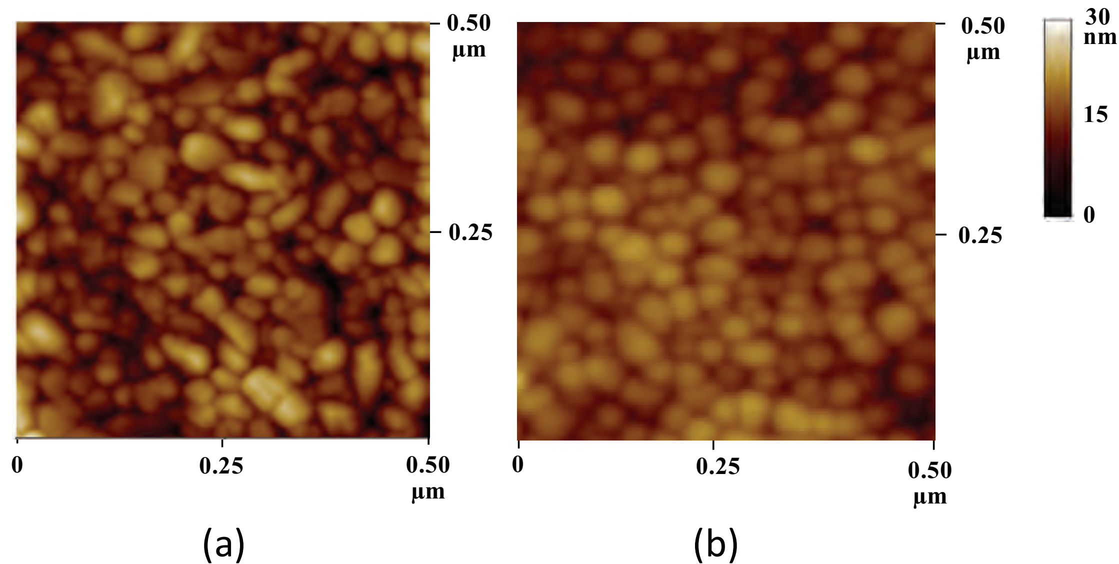

Figure 5.16: 2D AFM images of the CCTO films deposited on (a) alumina substrate (b) NGO substrate annealed at 800 °C.

uniformly round (see Fig. 5.16 (b)). In contrast with the CCTO film on alumina, there are differences in grain shapes and grain sizes.

The capacitance and dielectric loss of the CCTO interdigitated capacitor was measured at room temperature. Fig. 5.17 shows the capacitance versus frequency of the CCTO film on alumina substrate annealed at 800 °C. The capacitance of the film decreased as the frequency increased. The capacitance of the film decreased from 1.454 pF to 1.402 pF with the frequency increased from 40 kHz to 1000 kHz at 0 V. We can see that the capacitance of the film still did not change at the applied voltage 10 V. In another word, with an electric field of 10^5 V/m there is no electric field tuning of the polycrystalline CCTO film. The capacitance response of the CCTO film deposited on the NGO substrate is illustrated in Fig. 5.18. The capacitance of the film decreases from 2.080 pF to 2.054 pF with the increase in frequency from 40 kHz to 1000 kHz at 0 V. At the applied dc voltage 10 V, the capacitance of the film deposited on the NGO substrate decreases from 2.080 to 2.050 pF at 40 kHz.

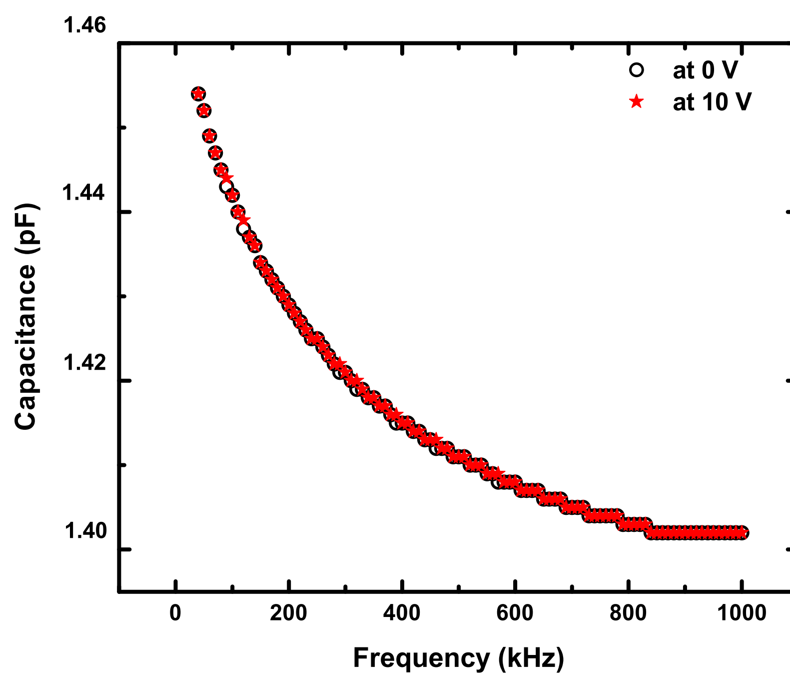

Figure 5.17: The frequency dependence of the capacitance of the CCTO thin film grown on alumina substrate annealed at 800 °C.

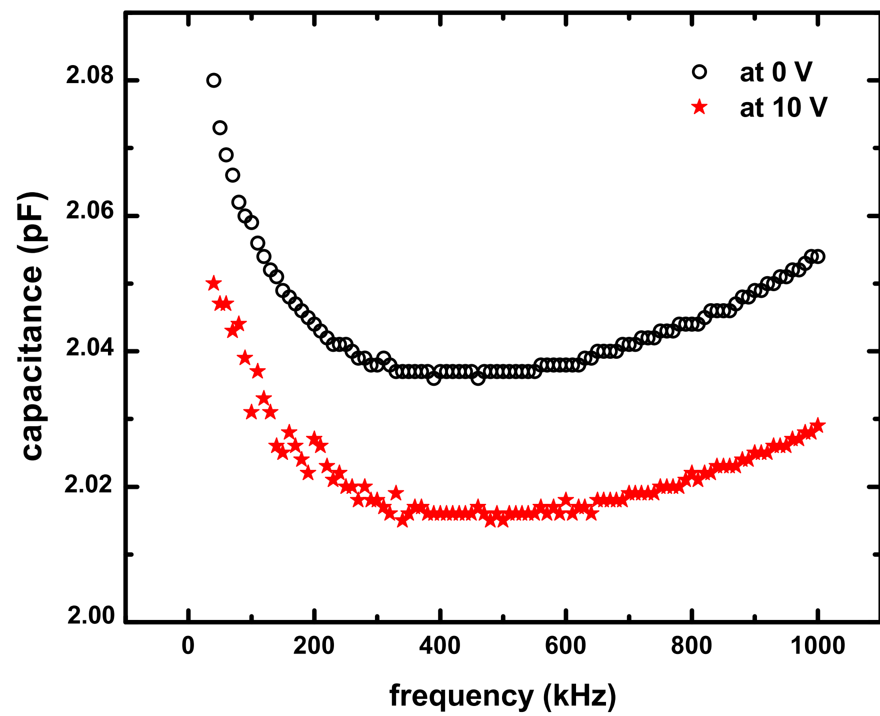

Figure 5.18: The frequency dependence of the capacitance of the CCTO thin film grown on NGO substrate annealed at 800 °C.

The dielectric constant and dielectric loss of the CCTO film deposited on alumina substrate are shown in Fig. 5.19. The dielectric constant of the CCTO film grown on alumina substrate is approximately 400 when there is no bias voltage and 10 V dc bias. However, the dielectric loss of the film slightly increases from 0.0496 to 0.0528 as the applied voltage increases from 0 V to 10 V. The frequency dependence of the dielectric constant and dielectric loss of CCTO film deposited on NGO substrate at 0 V and 10 V dc bias at room temperature is shown in Fig. 5.20. The dielectric constant of the film also decreased same as capacitance when the frequency increased. The dielectric responses to the frequencies are related with polarization. The polarization in dielectric material can be described by various possible mechanisms. At the lower frequencies, polarizing is took place by space charge and dipolar polarization which correspond to the individual process. As the frequencies increase, the dielectric constant decreases. This phenomena was explained by Wang et al. [23] that the dipole does not have enough time to react with the change in ac electric field. In this work, the maximum frequency is at 1 MHz so the tan δ relaxation peak related to Debye model [23] was not observed. The dielectric constant decrease from 1044 down to 1020 as the frequency increase from 40 kHz to 1000 kHz. The high dielectric constant of CCTO is related to their microstructure. It is known that the microstructure of CCTO material can be represented by the Brick's model as shown in Fig. 5.21(a). This model consisting of semiconducting grains between grain boundaries which has not been detected by XRD and SEM [4]. It has been reported that the circuit of this model consisting of two parallel RC circuits connect in series as seen in Fig. 5.21(b). The static permittivity (ε_s) of this model is explain by [46]

$$\varepsilon_s = \frac{R_g^2 C_g + R_{gb}^2 C_{gb}}{C_0 (R_g + R_{gb})^2} \tag{5.2}$$

where R_g and C_g are the grain resistance and capacitance, respectively. R_{gb} and C_{gb} are the grain boundaries resistance and capacitance, respectively. and C_0 is empty cell capacitance. Because of $R_g \ll R_{gb}$, can be obtained by

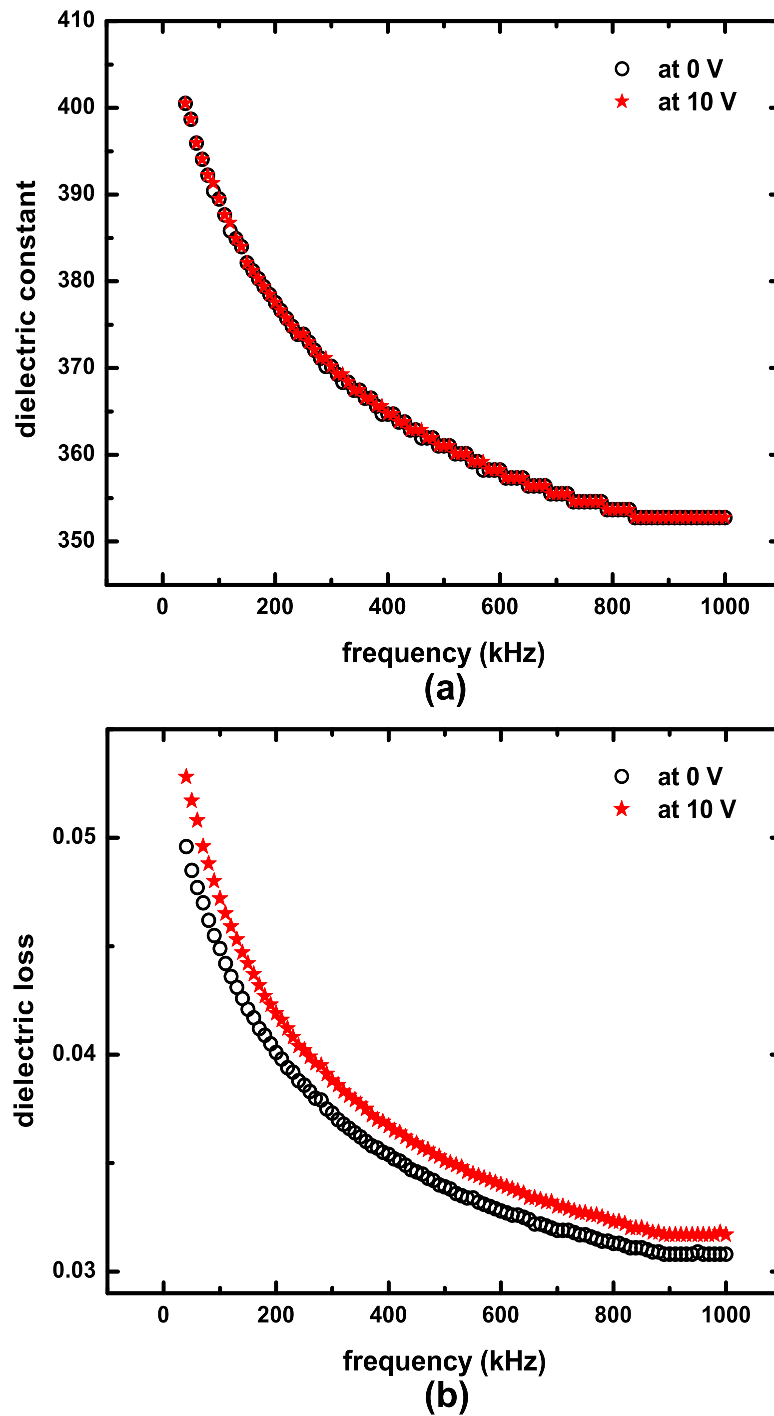

Figure 5.19: The (a) dielectric constant and (b) dielectric loss of the CCTO film deposited on Al_2O_3 substrate at 800 °C with different applied voltage.

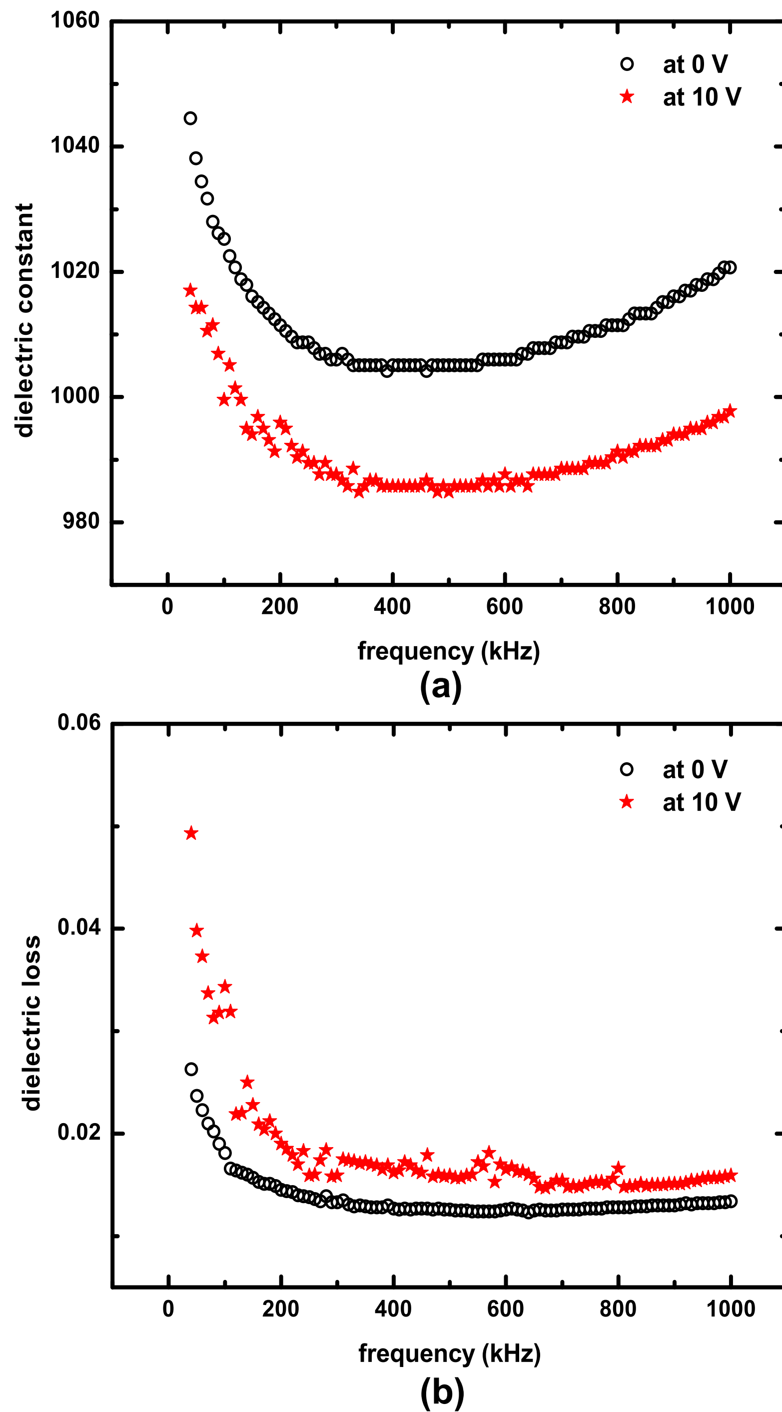

Figure 5.20: The (a) dielectric constant and (b) dielectric loss of the CCTO film deposited on NGO substrate at 800 °C with different applied voltage.

$$\varepsilon_s = \frac{C_{gb}}{C_0} = \varepsilon_{gb}\left(\frac{D}{d}\right) \quad (5.3)$$

where D is the grain size and d is the grain boundary thickness and ε_{gb} is dielectric constant of grain boundary.

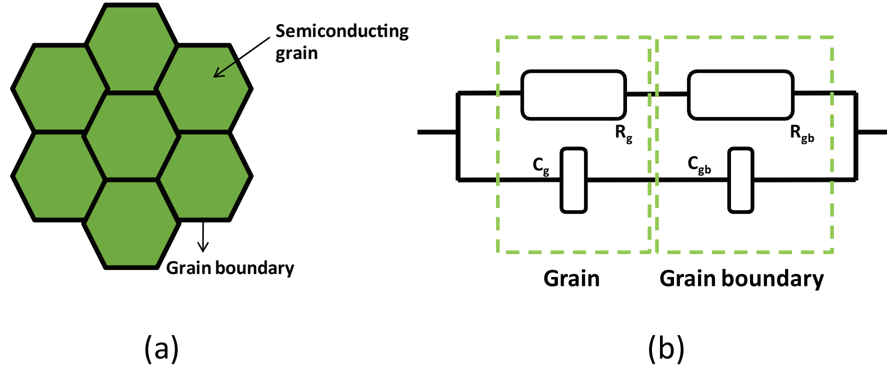

Figure 5.21: The (a) semiconducting grains between grain boundaries and (b) equivalent circuit for the microstructure of CCTO.

From this model the film that has bigger grain size, smaller and clearer grain boundary will have the high value of ε_s. In this thesis work, the grain size of the film deposited on NGO substrate shows clear grain boundary and presents bigger grain size (42 nm) than those film grown on alumina substrate (32 nm). Therefore, we can see that the film deposited on NGO substrate present higher dielectric constant than the film grown on alumina substrate. When the dc voltage 10 V is applied, the dielectric constant of the film grown on NGO decreases from 1044 (0 V) down to 1017 (10 V) as seen in Fig. 5.20(a). However, the loss tangent of the film increased as the applied voltage increased. The loss tangent abruptly changed from 0.0263 at 0 V to 0.0493 at 10 V dc bias as seen in Fig. 5.20(b). For the CCTO film deposited on the NGO substrate can be tuned with the tunability of 2.6% and maximum dielectric loss of 0.0493 by applying an electric field of 10^5 V/m while the CCTO film deposited on alumina can not be tuned. As expected, the CCTO film deposited on NGO single crystal substrate shows higher dielectric

constant than those film deposited on polycrystalline alumina substrate. Similarly, the film grown on NGO substrate that presents {200} preferred orientation can respond to an applied electric field than that of polycrystalline film grown on alumina substrate. The dielectric loss of the CCTO film deposited on NGO substrate is lower than that of the film grown on alumina substrate even if the film on NGO is bias with the applied voltage of 10 V.

CHAPTER VI

CONCLUSIONS

In this thesis work, we have prepared the CCTO films by a sol-gel spin coating technique. In previous chapters, we have explained and illustrated the CCTO thin film depositions, their characterizations as well as their results. For the conclusion of this study, we will conclude as follow:

In the part of effect of annealing temperature on structural properties and surface morphology of CCTO films, the CCTO films were deposited on Si substrate by varying the annealing temperature from 600 °C to 1000 °C. We chose Si substrates for this study because they are cheap. I found that the optimum temperature for growing CCTO films on Si substrate is 800 °C. At this temperature, the three main CCTO peaks indicating (221), (400) and (422) planes appeared with high intensities. The number and intensities of unwanted oxide peaks were minimum. At lower temperatures, 600 °C and 700 °C, there were no characteristic peaks of CCTO observed in the XRD spectra. All atoms did not have enough energy building from this such low temperatures to move around and form the crystalline structure. At higher temperatures, 900 °C and 1000 °C, the characteristic peaks appeared with low intensities compared to TiO_2 peaks. It seemed that the TiO_2 peaks tend to appear with high intensities at higher temperature. This could be explained that if the temperature is too high, the atoms that were already stable in their locations tend to move again. And the movements of atoms might be more random and hard to control at the such high temperatures. In the aspect of the surface morphology of the film, it is clearly seen that the grain size of the film increases with increasing annealing temperature. It can be explained that

the mobility of ad-atoms on the substrate surface increases at higher temperature so that the diffusion distance of the ad-atoms on the surface increase resulting in better growth of grains. The CCTO film annealed at 800 °C has an average grain size of about 50 nm and increases to 130 nm and 400 nm for the film annealed at 900 °C and 1000 °C, respectively.

For the effect of substrates on structural properties and surface morphology of CCTO films, the CCTO film grown on LAO substrate shows better quality than the film grown on Si and NGO substrates. The CCTO film on LAO tends to be an epitaxial film and exhibits the {200} preferred orientation due to small lattice mismatch between the film and the LAO substrate about 2.5 %. The lattice constant of the film grown on LAO is 7.391 Å. The film grown on NGO substrate shows not only the {200} preferred orientation of CCTO like observed in CCTO on LAO, but also presents (220) and (222) planes of CCTO. The lattice mismatch between the film and NGO is 4.3 %. It has been seen that the lattice mismatch strongly influences on the film quality which can be seen in the difference of characteristic planes of CCTO. With less lattice mismatch, the {200} orientations are preferred. The lattice mismatch between the film and NGO is about 2 times higher than that of LAO. However, the lattice parameters of the films grown on LAO and NGO substrates are 7.391 Å and 7.390 Å, respectively which are very much the same. The lattice parameter of the CCTO film on Si substrate is approximately 7.380 Å which is slightly smaller from that of LAO and NGO and from the CCTO bulk. This is due to the much difference in lattice constant of the CCTO film and Si. The average grain size of films deposited on Si, LAO and NGO are 58, 40 and 44 nm. The grain is biggest for the film on Si. Note that it was hard to measure the grain size for the film on Si due to the appearance of connecting grains forming sponge-like shape instead of individual grains. The difference in grain size among those film is not much which is in 40-60 nm range. This is due to a fixed annealing temperature at 800 °C. It has been known for a long time that temperature is the main parameter to control the grains besides the growth rate. However the shape of grains for each film was clearly different; sponge-like shape can be seen in the

films grown on Si and round shape can be seen in the film grown on LAO and NGO.

I have investigated the effect of the Fe doping on structural and morphology properties. In this thesis, I synthesized the CCTO film doped with Fe at 4, 5, 6 and 7 wt% which were confirmed with EDS results. I found that the crystal structure of the film doped with Fe exceed 6 % is destroyed. From the X-ray diffraction pattern, the CCTO dope with Fe 7 wt% the characteristic peaks of CCTO disappeared. The lattice constant of the film doped with Fe (7.37 Å) decreases compared to that of the pure CCTO film deposited on Si substrate (7.38 Å). This is because the Fe^{3+} (0.65 Å) with smaller ionic radius substituted in the Ti^{4+} (0.68 Å) resulting in the decrease in lattice constant in the doped film. Likewise the morphology property, the grain size of the Fe-doped films decreased as the Fe contents increased until 6 wt%. The grain size of the film doped with Fe decrease as the Fe concentration increase due to Fe atoms obstruct the forming of CCTO structure. However, the CCTO film doped with Fe 7 wt%, the grain size become bigger. This could be the thickness effect; this film was thicker due to more viscosity in the prepared precursor. The oxidation state of Fe in the CCTO film presents Fe^{3+} which confirmed by XAS experiment.

In the section of electrical properties of CCTO films, I compared the dielectric property of the films deposited on single crystal NGO substrate and polycrystalline alumina substrate. I found that the CCTO film deposited on NGO substrate exhibited high dielectric constants at which the value were higher than those of the CCTO film deposited on alumina substrate. The dielectric constant of our films at 40 kHz is approximately 1044 and 400 for the film grown on NGO and alumina substrates, respectively. The dielectric constant of the CCTO film is related to the microstructure. According to the equation 5.3, the grain size of the film deposited on NGO smaller than the film deposited on alumina resulting in the dielectric constant of the CCTO film on NGO substrate is higher than that of the CCTO film on alumina substrate. When applied electric field of 10^5 V/m, the dielectric constant of the film deposited on NGO can be tuned much better

compared to the film deposited on alumina substrate. In polycrystalline materials, the dipoles are oriented randomly compared to the dipoles in epitaxy materials. When an electric field is applied to each material, the response to the electric field is different; the dipoles in response epitaxy materials quicker and also the neighbor dipole easily induces the dipoles around it to orient in the same direction. The dielectric constant decreased from 1044 (0 V) to 1017 (10 V) for the film grown on NGO but there was no significantly change for the film grown on alumina substrate. This is due to the fact that the film grown on NGO substrate that presents {200} preferred orientation can respond to an applied electric field than that of polycrystalline film grown on alumina substrate. Moreover, the dielectric losses of the film grown on NGO substrate presented lower than values those of the film grown on alumina substrate. The maximum value of the dielectric loss at 40 kHz in our CCTO film deposited on alumina substrate was 0.0528, which was higher than that of the film on NGO substrate (0.0493). Since the dielectric constant of the CCTO film on NGO showing 200 preferred orientation can be tuned with dc bias better than the CCTO film on alumina, this behavior suggests the much more potential of 200 preferred orientation films in applying to phase-shifting devices. Along with high dielectric constant and the capability of tuning with an electric field, the advantage of using 200 preferred orientation films is that the dielectric loss tangent is small on the order of 10^{-2}.

References

[1] Subramanian, M. A., Li, D., Duan, N., Reisner, B. A., and Sleight, A. W. High Dielectric Constant in $ACu_3Ti_4O_{12}$ and $ACu_3T_3FeO_{12}$ Phases. *J. Solid State Chem.* 151 (2000): 323–325.

[2] Sinclair, D. C., Adams, T. B., Morrison, F. D., and West, A. R. $CaCu_3Ti_4O_{12}$: One-step internal barrier layer capacitor. *Appl. Phys. Lett.* 80 (2002): 2153–2155.

[3] Li, Y., Hu, Z., Sun, J., Meng, X., and Chu, J. Preparation and properties of $CaCu_3Ti_4O_{12}$ thin film grown on $LaNiO_3$-coated silicon by sol-gel process. *J. Cryst. Growth* 310 (2008): 378–381.

[4] Liu, L., Fan, H., Fang, P., and Jin, L. Electrical heterogeneity in $CaCu_3Ti_4O_{12}$ ceramics fabricated by sol-gel method. *Solid State Commun.* 142 (2007): 573–576.

[5] Calvert, C. C., Rainforth, W. M., Sinclair, D. C., and West, A. R. EELS characterisation of bulk $CaCu_3Ti_4O_{12}$ ceramics. *Micron* 37 (2006): 412–419.

[6] Thongbai, P. et al. Giant dielectric behaviour of $CaCu_3Ti_4O_{12}$ subjected to post-sintering annealing and uniaxial stress. *J. Phys.* 19 (2007): 236208–1 –10.

[7] Bender, B. and Pan, M.-J. The effect of processing on the giant dielectric properties of $CaCu_3Ti_4O_{12}$. *Mater. Sci. Eng., B* 117 (2005): 339–347.

[8] Yang, J., Shen, M., and Fang, L. The electrode/sample contact effects on the dielectric properties of the $CaCu_3Ti_4O_{12}$ ceramic. *Mater. Lett.* 59 (2005): 3990–3993.

[9] Sun, C. P. et al. A Low-Temperature Specific Heat Study of the Giant Dielectric Constant Materials. *J. Phys.* 20 (2008): 285214–285218.

[10] Fang, L. and Shen, M. Deposition and dielectric properties of $CaCu_3Ti_4O_{12}$ thin films on $Pt/Ti/SiO_2/Si$ substrates using pulsed-laser deposition. *Thin Solid Films* 440 (2003): 60–65.

[11] Zhao, Y. et al. High dielectric constant in $CaCu_3Ti_4O_{12}$ thin film prepared by pulsed laser deposition. *Thin Solid Films* 445 (2003): 7–13.

[12] Prakash, B. S., Varma, K., Michau, D., and Maglione, M. Deposition and dielectric properties of $CaCu_3Ti_4O_{12}$ thin films deposited on $Pt/Ti/SiO_2/Si$ substrates using radio frequency magnetron sputtering. *Thin Solid Films* 516 (2008): 2874–2880.

[13] Jimenez, R., Calzada, M., Bretos, I., Goes, J., and Sombra, A. Dielectric properties of sol-gel derived $CaCu_3Ti_4O_{12}$ thin films onto $Pt/TiO_2/Si$(1 0 0) substrates. *J. Eur. Ceram. Soc.* 27 (2007): 3829–3833.

[14] Nigro, R. L. et al. Effects of high temperature annealing on MOCVD grown $CaCu_3Ti_4O_{12}$ films on $LaAlO_3$ substrates. *Surf. Coat. Technol.* 201 (2007): 9243–9247.

[15] Si, W. et al. Epitaxial thin films of the giant-dielectric-constant material $CaCu_3Ti_4O_{12}$ grown by pulsed-laser deposition. *Appl. Phys. Lett.* 81 (2002): 2056–2058.

[16] MAURYA, D., SINGH, D. P., AGRAWAL, D. C., and MOHAPATRA, Y. N. Preparation of high dielectric constant thin films of $CaCu_3Ti_4O_{12}$ by sol-gel. *Bull. Mater. Sci.* 31 (2008): 55–59.

[17] Fang, L., Shen, M., Yang, J., and Li, Z. Reduced dielectric loss and leakage current in $CaCu_3Ti_4O_{12}/SiO_2/CaCu_3Ti_4O_{12}$ multilayered films. *Solid State Commun.* 137 (2006): 382.

[18] Chiodelli, G. et al. Electric and dielectric properties of pure and doped $CaCu_3Ti_4O_{12}$ perovskite materials. *Solid State Commun.* 132 (2004): 241–246.

[19] Grubbs, R. K. et al. Dielectric and magnetic properties of Fe- and Nb-doped $CaCu_3Ti_4O_{12}$. *Phys. Rev. B* 72 (2005): 104111–1 – 11.

[20] Krohns, S. et al. Correlations of structural, magnetic, and dielectric properties of undoped and doped $CaCu_3Ti_4O_{12}$. *Eur. Phys. J. B* 72 (2009): 174.

[21] Lunkenheimer, P. et al. Colossal dielectric constants in transition-metal oxides. *Eur. Phys. J. Special Topics* 180 (2010): 61–89.

[22] Feng, L., Wang, Y., Yan, Y., Cao, G., and Jiao, Z. Growth of highly-oriented $CaCu_3Ti_4O_{12}$ thin films on $SrTiO_3$ (1 0 0) substrates by a chemical solution route. *Appl. Surf. Sci.* 253 (2006): 2268.

[23] Wang, C.-M., Lin, S.-Y., Kao, K.-S., Chen, Y.-C., and Weng, S.-C. Microstructural and electrical properties of $CaTiO_3$-$CaCu_3Ti_4O_{12}$ ceramics. *J. Alloys Compd.* 491 (2010): 424.

[24] Deschanvres, A., Raveau, B., and Tollemer, F. Substitution of copper for a divalent metal in perovskite-type titanates. *Bull. Soc. Chim. Fr.* 11 (1967): 4077–4078.

[25] BOCHU, B. et al. Synthesis and characterization of a series of perovskite titanates isostructural with $[CaCu_3](Mn_4)O_{12}$. *J. Solid State Chem.* 29 (1979): 291–298.

[26] Homes, C. C., Vogt, T., Shapiro, S. M., Wakimoto, S., and Ramirez, A. P. Optical response of high-Dielectric-constant perovskite-related oxide. *SCIENCE* 293 (2001): 673.

[27] Almeida, A. et al. Experimental and numerical investigation of a ceramic dielectric resonator (DRA): $CaCu_3Ti_4O_{12}$ (CCTO). *Physica B* 403 (2008): 586.

[28] Manik, S. and Pradhan, S. Microstructure characterization of ball-mill-prepared nanocrystalline $CaCu_3$ Ti_4O_{12} by Rietveld method. *Physica E* 33 (2006): 160.

[29] Parra, R. et al. Sol-gel synthesis of mesoporous $CaCu_3Ti_4O_{12}$ thin films and their gas sensing response. *J. Solid State Chem.* 183 (2010): 1209–1214.

[30] Kim, I.-D., Rothschild, A., Hyodo, T., and Tuller, H. L. Microsphere templating as means of enhancing surface activity and gas sensitivity of $CaCu_3Ti_4O_{12}$ thin films. *Nano Lett.* 6, No.2 (2006): 193–198.

[31] Lasaga, A. C. and Cygan, R. T. Electronic and ionic polarizabilities of silicate minerals. *Am. Mineral.* 67 (1982): 328–334.

[32] B.D.Cullity. *Elements of X-Ray Diffraction.* New York: Addison-Wesley. 1978.

[33] C, K.. *Introduction to Solid State Physics.* UK:IOP Publishing Ltd 2001.

[34] Chang, L.-C., Lee, D.-Y., Ho, C.-C., and Chiou, B.-S. Thickness-dependent microstructures and electrical properties of $CaCu_3Ti_4O_{12}$ films derived from sol-gel process. *Thin Solid Films* 516 (2007): 454–459.

[35] Hong, L., Zhaohui, P., Xiaohong, Z., Dingquan, X., and Jianguo, Z. The effect of different electrode structures on the dielectric properties of lanthanum-doped lead titanate ferroelectric thin films. *Front. Mater. Sci. China* 1(3) (2007): 322–325.

[36] FARNELL, G. W., A.CERMAK, I., P.SILVESTER, and WONG, S. Capacitance and Field Distributions for Interdigital Surface- Wave Transducers. *IEEE T. Son. Ulrason* 3 (1970): 188–195.

[37] Hassini, A., Gervais, M., Coulon, J., Phuoc, V. T., and Gervais, F. Synthesis of $Ca_{0.25}Cu_{0.75}TiO_3$ and infrared characterization of role played by copper. *Mater. Sci. Eng., B* 87 (2001): 165.

[38] Ramana, C., Smith, R., Hussain, O., and Julien, C. On the growth mechanism of pulsed-laser deposited vanadium oxide thin films. *Mater. Sci. Eng., B* 111 (2004): 218–225.

[39] Fu, Y., Du, H., Zhang, S., and Gu, Y. Stress and surface morphology of tinicu thin films: effect of annealing temperature. *Surf. Coat. Technol.* 198 (2005): 389–394.

[40] Supasai, T. et al. Influence of temperature annealing on optical properties of $SrTiO_3/BaTiO_3$ multilayered films on indium tin oxide. *Appl. Surf. Sci.* 256 (2010): 4463.

[41] Hodak, S. K. and Rogers, C. T. Microstructure and dielectric response of $SrTiO_3/NdGaO_3$ interdigitated capacitors. *Microelectron. Eng.* 85 (2008): 444–451.

[42] Wilke, M., Partzsch, G. M., Bernhardt, R., and Lattard, D. Determination of the iron oxidation state in basaltic glasses using XANES at the K-edge. *Chem. Geol.* 220 (2005): 157.

[43] Armelao, L. et al. Nanocrystalline *alpha*-Fe_2O_3 sol-gel thin films: a microstructural study. *J. Non-Cryst. Solids* 192&193 (1995): 437.

[44] Ide-Ektessabi, A., Kawakami, T., and Watt, F. Distribution and chemical state analysis of iron in the Parkinsonian substantia nigra using synchrotron radiation micro beams. *Nucl. Instr. and Meth. in Phys. Res. B* 213 (2004): 592.

[45] Marino-Castellanos, P., Anglada-Rivera, J., Cruz-Fuentes, A., and Lora-Serrano, R. Magnetic and microstructural properties of the Ti_{4+}-doped Barium hexaferrite. *J. Magn. Magn. Mater.* 280 (2004): 216.

[46] Amaral, F., Valente, M., and Costa, L. Dielectric properties of $CaCu_3Ti_4O_{12}$ (CCTO) doped with GeO_2. *J. Non-Cryst. Solids* 356 (2010): 826.

APPENDICES

Appendix A

Fe-doping concentration

In order to dope Fe in CCTO films, we calculated the percentage of Fe concentration by following expression

$$\left(\frac{\frac{g_{Fe}}{MW_{Fe}}}{\frac{g_{Ca}}{MW_{Ca}}}\right)\left(\frac{MW_{Fe}}{MW_{CCTO}}\right) \times 100 = ...\% \tag{1}$$

$$\left(\frac{g_{Fe}}{278.01}\right)\left(\frac{176.19}{0.85}\right)\left(\frac{278.01}{1240.24}\right) \times 100 = ...\% \tag{2}$$

$$g_{Fe} \times 16.713 = ...\% \tag{3}$$

In this thesis, we tried to dope-Fe 1%, 3%, 5% and 10% by weight. By following the equation above, we weighed Fe 0.0598 g, 0.1790 g, 0.299 g and 0.598 g for Fe doped 1%, 3%, 5% and 10% by weight, respectively. However, the quantity of Fe in our films were later measured from EDS experiments which are 4%, 5%, 6% and 7% by weight instead of 1%, 3%, 5% and 10% by weight.

Appendix B
XRD database

The structure of the CCTO film obtained from XRD spectra were compared with the XRD database from The International Centre for Diffraction Data (ICDD) which presented as follow

Pattern : 01-075-2188 | **Radiation =** 1.540598 | **Quality :** Calculated

$(CaCu_3)Ti_4O_{12}$

Calcium Copper Titanium Oxide
Also called: Calcium tricopper tetratitanium oxide

Lattice : Body-centered cubic

S.G. : Im-3 (204)

a = 7.39100

Z = 2

Mol. weight = 614.31

Volume [CD] = 403.75

Dx = 5.053

I/Icor = 5.76

ICSD collection code: 032002
Temperature factor: ITF
Cancel:
Data collection flag: Ambient.

Bochu, B., Deschizeaux, M.N., Joubert, J.C., Collomb, A., Chenavas, J., Marezio, M., J. Solid State Chem., volume 29, page 291 (1979)
Calculated from ICSD using POWD-12++

Radiation : CuKa1

Lambda : 1.54060

SS/FOM : F22=1000(0.0000,22)

Filter : Not specified

d-sp : Calculated spacings

2th	i	h	k	l
16.952	27	1	1	0
24.062	3	2	0	0
29.581	38	2	1	1
34.289	999	2	2	0
38.486	73	0	1	3
42.327	49	2	2	2
45.904	40	3	2	1
49.276	263	4	0	0
52.485	13	4	1	1
55.562	3	0	2	4
58.529	8	3	3	2
61.405	401	4	2	2
64.204	5	0	1	5
69.618	6	1	2	5
72.252	92	4	4	0
74.848	17	4	3	3
77.413	7	6	0	0
79.951	7	6	1	1
82.471	101	6	2	0
84.975	1	1	4	5
87.470	1	6	2	2
89.961	2	1	3	6

Pattern : 00-021-1276 **Radiation =** 1.540598 **Quality :** High

TiO_2

Titanium Oxide
Rutile, syn
Also called: titania

Lattice : Tetragonal		***Mol. weight =*** 79.90
S.G. : P42/mnm (136)		***Volume [CD] =*** 62.43
a = 4.59330		***Dx =*** 4.250
		Dm = 4.230
c = 2.95920		
	Z = 2	***I/Icor =*** 3.40

General comments: No impurity over 0.001%.
Vickers hardness number: VHN_{100}=1132-1187.
Sample source or locality: Sample obtained from National Lead Co., South Amboy, New Jersey, USA.
General comments: Pattern reviewed by Syvinski, W., McCarthy, G., North Dakota State Univ, Fargo, North Dakota, USA, *ICDD Grant-in-Aid* (1990). Agrees well with experimental and calculated patterns.
General comments: Two other polymorphs, anatase (tetragonal) and brookite (orthorhombic), converted to rutile on heating above 700 C.
General comments: Additional weak reflections [indicated by brackets] were observed.
Optical data: A=2.9467, B=2.6505, Sign=+
Additional pattern: Validated by calculated pattern.
General comments: Optical data on specimen from *Dana's System of Mineralogy, 7th Ed.*, **I** 555.
General comments: Naturally occurring material may be reddish brown.
Color: White
Reflectance: Opaque mineral optical data on specimen from Sweden: R_3R%= 20.3, Disp.=Std.
Temperature of data collection: Pattern taken at 25 C.
Data collection flag: Ambient.

Natl. Bur. Stand. (U.S.) Monogr. 25, volume 7, page 83 (1969)

Radiation : CuKa1	***Filter :*** Monochromator crystal
Lambda : 1.54056	***d-sp :*** Not given
SS/FOM : F30=108(0.0087,32)	***Internal standard :*** W

2th	*i*	*h*	*k*	*l*
27.447	100	1	1	0
36.086	50	1	0	1
39.188	8	2	0	0
41.226	25	1	1	1
44.052	10	2	1	0
54.323	60	2	1	1
56.642	20	2	2	0
62.742	10	0	0	2
64.040	10	3	1	0
65.480	2	2	2	1
69.010	20	3	0	1
69.790	12	1	1	2
72.410	2	3	1	1
74.411	1	3	2	0
76.510	4	2	0	2
79.822	2	2	1	2
82.335	6	3	2	1
84.260	4	4	0	0
87.464	2	4	1	0
89.557	8	2	2	2
90.708	4	3	3	0
95.275	6	4	1	1
96.017	6	3	1	2
97.176	4	4	2	0
98.514	1	3	3	1
105.099	2	4	2	1
106.019	2	1	0	3
109.406	2	1	1	3
116.227	4	4	0	2
117.527	4	5	1	0
120.059	8	2	1	3
122.788	8	4	3	1
123.660	8	3	3	2
131.847	6	4	2	2
136.549	8	3	0	3
140.052	12	5	2	1
143.116	2	4	4	0
155.869	2	5	3	0

Pattern : 00-029-1360 | **Radiation =** 1.540598 | **Quality :** High

TiO_2

Titanium Oxide
Brookite

Lattice : Orthorhombic

S.G. : Pcab (61)

a = 5.45580

b = 9.18190

c = 5.14290

a/b = 0.59419

c/b = 0.56011

Z = 8

Mol. weight = 79.90

Volume [CD] = 257.63

Dx = 4.120

Dm = 4.140

Optical data: A=2.5831, B=2.5843, Q=2.7004, Sign=+, 2V=~28°
Additional pattern: To replace 00-016-0617 and validated by calculated pattern.
Color: Black
Additional pattern: See ICSD 36408 (PDF 01-076-1934).
Sample source or locality: Specimen from Magnet Cove, Arkansas, USA (USNM 97661).
Analysis: Spectrographic analysis: 0.1-1.0% Si; 0.01-0.1% each of Al, Fe, and V; 0.001-0.01% Mg.
General comments: Niobian brookite from Mozambique [Chemical analysis (wt.%): Ti O2 80.7, Nb2 O5 14.1, FeO 5.53]; Carvalho et al., *Rev. Cien. Geol. Ser. A*, **7** 61 (1974) reports an identical pattern.
Temperature of data collection: Pattern taken at 25 C.
General comments: Intensities verified by calculated pattern.
Data collection flag: Ambient.

Natl. Bur. Stand. (U.S.) Monogr. 25, volume 3, page 57 (1964)

Radiation : CuKa1

Lambda : 1.54056

SS/FOM : F30= 58(0.0115,45)

Filter : Beta

d-sp : Not given

2th	i	h	k	l
25.340	100	1	2	0
25.689	80	1	1	1
30.808	90	1	2	1
32.791	4	2	0	0
36.252	25	0	1	2
37.297	18	2	0	1
37.934	6	1	3	1
38.371	4	2	2	0
38.576	4	2	1	1
39.205	5	0	4	0
39.967	8	1	1	2
40.153	18	0	2	2
42.340	16	2	2	1
46.072	16	0	3	2
48.012	30	2	3	1
49.173	18	1	3	2
49.694	3	2	1	2
52.012	3	2	4	0
54.205	20	3	2	0
55.234	30	2	4	1
55.711	5	1	5	1
57.176	13	1	1	3
57.685	2	2	3	2
59.991	7	1	2	3
62.065	10	0	5	2
63.065	4	1	6	0
63.415	9	3	1	2
63.643	12	2	5	1
64.104	12	2	0	3
64.603	6	1	3	3
65.002	10	2	1	3
65.876	9	1	6	1
68.768	5	4	0	0
70.432	8	3	3	2
71.490	3	4	0	1
71.931	2	2	3	3
73.648	2	0	0	4
76.948	10	0	2	4
79.024	2	4	3	1
79.283	1	1	2	4
83.643	4	3	3	3
84.287	2	0	8	0
84.724	2	4	4	1
86.743	4	0	4	4
95.590	3	5	2	1
*95.590	3	4	2	3
95.993	2	2	8	1
97.609	4	3	2	4
102.559	2	1	2	5
103.201	4	3	7	2
*103.201	4	2	5	4

Pattern : 03-065-5714 | **Radiation =** 1.540598 | **Quality :** Calculated

TiO_2

Titanium Oxide

Lattice : Body-centered tetragonal
S.G. : I41/amd (141)
Mol. weight = 79.90
Volume [CD] = 136.30
a = 3.78500
c = 9.51400
Z = 4
Dx = 3.894
I/Icor = 5.04

NIST M&A collection code: A 50867 ST1243 1
Temperature factor: TF Isotropic TF given by author
Sample preparation: Commercial pigmentary material was used
Remarks from ICSD/CSD: Anatase-synthetic
Data collection flag: Ambient.

Cromer, D.T., Herrington, K., J. Am. Chem. Soc., volume 77, page 4708 (1955)
Calculated from NIST using POWD-12++

Radiation : CuKa1
Lambda : 1.54060
SS/FOM : F30=597(0.0014,35)
Filter : Not specified
d-sp : Calculated spacings

2th	i	h	k	l
25.304	999	1	0	1
36.949	56	1	0	3
37.793	175	0	0	4
38.566	71	1	1	2
48.036	238	2	0	0
53.886	148	1	0	5
55.061	146	2	1	1
62.107	23	2	1	3
62.684	103	2	0	4
68.756	49	1	1	6
70.287	49	2	2	0
74.053	4	1	0	7
75.046	74	2	1	5
76.032	20	3	0	1
80.740	3	0	0	8
82.156	5	3	0	3
82.672	35	2	2	4
83.154	15	3	1	2
93.244	5	2	1	7
94.202	17	3	0	5
95.162	19	3	2	1
98.325	11	1	0	9
99.812	7	2	0	8
101.236	5	3	2	3
107.478	24	3	1	6
108.988	12	4	0	0
112.826	2	3	0	7
113.868	22	3	2	5
114.918	13	4	1	1
118.472	35	2	1	9
*118.472	35	1	1	10
120.117	6	2	2	8
121.749	5	4	1	3
122.353	15	4	0	4
122.921	10	3	3	2
131.049	20	4	2	0
132.007	5	1	0	11
135.995	3	3	2	7
137.389	19	4	1	5
142.878	1	4	0	6
143.850	7	3	0	9

Pattern : 00-037-1497 **Radiation =** 1.540598 **Quality :** High

CaO

Calcium Oxide
Lime, syn
Also called: calcia, burnt lime, quicklime

Lattice : Face-centered cubic

S.G. : Fm-3m (225)

Mol. weight = 56.08

Volume [CD] = 111.33

a = 4.81059

Z = 4

Dx = 3.346

2th	i	h	k	l
32.204	36	1	1	1
37.347	100	2	0	0
53.856	54	2	2	0
64.154	16	3	1	1
67.375	16	2	2	2
79.665	6	4	0	0
88.524	6	3	3	1
91.459	16	4	2	0
103.343	12	4	2	2
112.631	6	5	1	1
129.879	6	4	4	0
142.642	10	5	3	1
147.776	16	6	0	0

Sample preparation: The sample was prepared from calcium hydroxide obtained from Fisher Scientific Co., Fair Lawn, New Jersey, USA, by heating it to 925° overnight. It was kept under a stream of dry N2 during data collection.
Structure: The structure was determined by Oftedal (1).
Additional pattern: See ICSD 75785 (PDF 01-082-1690).
Temperature of data collection: The mean temperature of data collection was 25.3°.
Additional pattern: To replace 00-004-0777 (2).
General comments: References to earlier patterns will be found in reference 4.
Color: Colorless
General comments: Pattern reviewed by K. Martin and G. McCarthy, North Dakota State Univ., Fargo, North Dakota, USA, *ICDD Grant-in-Aid* (1990). Excepte for the (220) reflection, there is good agreement with experimental and calculated patterns. The experimental pattern had I(220)=245; the calculated value is I(220)=49.
Data collection flag: Ambient.

McMurdie, H., Morris, M., Evans, E., Paretzkin, B., Wong-Ng, W., Hubbard, C., Powder Diffraction, volume 1, page 266 (1986)

CAS Number: 1305-78-8

Radiation : CuKa1

Lambda : 1.54060

SS/FOM : F13=149(0.0067,13)

Filter : Monochromator crystal

d-sp : Diffractometer

Internal standard : W

Pattern : 00-046-1212 **Radiation =** 1.540598 **Quality :** High

Al_2O_3

Aluminum Oxide
Corundum, syn
Also called: α- Al2 O3

Lattice : Rhombohedral

S.G. : R-3c (167)

Mol. weight = 101.96

Volume [CD] = 254.81

a = 4.75870

c = 12.99290

Z = 6

Dx = 3.987

2th	i	h	k	l
25.579	45	0	1	2
35.153	100	1	0	4
37.777	21	1	1	0
41.676	2	0	0	6
43.356	66	1	1	3
46.176	1	2	0	2
52.550	34	0	2	4
57.497	89	1	1	6
59.740	1	2	1	1
61.118	2	1	2	2
61.300	14	0	1	8
66.521	23	2	1	4
68.214	27	3	0	0
70.420	1	1	2	5
74.299	2	2	0	8
76.871	29	1	0	10
77.226	12	1	1	9
80.422	1	2	1	7
80.700	2	2	2	0
83.217	1	3	0	6
84.359	3	2	2	3
85.143	1	1	3	1
86.363	2	3	1	2
86.503	3	1	2	8
88.997	9	0	2	10

Sample source or locality: The sample is an alumina plate as received from *ICDD.*
General comments: Unit cell computed from d_{obs}.
Optical data: A=1.7604, B=1.7686, Sign=-
Data collection flag: Ambient.

Huang, T., Parrish, W., Masciocchi, N., Wang, P., Adv. X-Ray Anal., volume 33, page 295 (1990)

Radiation : CuKa1

Lambda : 1.54056

SS/FOM : F25=379(0.0026,25)

Filter : Not specified

d-sp : Diffractometer

Appendix C

Conference Presentations

International Presentations:

2009, Y. Kasa and S. K. Hodak. Characterization of Pure and Fe-doped $CaCu_3Ti_4O_{12}$ Thin Films Prepared by Sol-Gel Technique. Oral presentation at TACT 2009 International Thin Films Conference at National Taipei University of Technology, Taipei, Taiwan (December 14-16 2009) Code: C213-O

2009, Y. Kasa and S. K. Hodak. Characterization of Pure and Fe-doped $CaCu_3Ti_4O_{12}$ Thin Films Prepared by Sol-Gel Technique. Poster presentation at The Fifth Mathematics and Physical Sciences Graduate Congress, Faculty of Science, Chulalongkorn University, Bangkok (December 7-9 2009) Code: PM 516

Local Presentations:

2010.Y. Kasa, A. Wisitsoraat, D. Phokharatkul and S. K. Hodak. Structural Properties and Fabrication of $CaCu_3Ti_4O_{12}$ Thin Films Capacitor. Oral presentation at Siam Physics Congress 2010, Kanjanaburi (March 25-27 2010) Code: TF-O10

2010.Y. Kasa and S. K. Hodak. Structural Properties and Fabrication of $CaCu_3Ti_4O_{12}$ Thin Films Capacitor. Poster presentation at The 16th National Graduated Research Conference, Faculty of Science, Meajo University, Chaingmai (March 11 2010) Code: P-PS 10

2009, Y. Kasa and S. K. Hodak. Preparation and Characterization of $CaCu_3Ti_4O_{12}$ Thin Films Derived from Sol-Gel Process. Poster presentation at Siam Physics Congress 2009, Methavalai Hotel, Cha-am, Phetchburi (March 19-21 2009) Code: TF-P28

2009, Y. Kasa and S. K. Hodak. Preparation and Characterization of $CaCu_3Ti_4O_{12}$ Thin Films Derived from Sol-Gel Process. Oral presentation at The Science Forum 2009, Faculty of Science, Chulalongkorn University, Bangkok (March 12-13 2009) Code: P 4

Appendix D

Publication

2010.Y. Kasa and S. K. Hodak. Structural Properties and Fabrication of $CaCu_3Ti_4O_{12}$ Thin Films Capacitor. (to be published in The 16th National Graduated Research Conference proceeding)

สมบัติเชิงโครงสร้างและการสร้างตัวเก็บประจุแบบฟิล์มบางแคลเซียมคอปเปอร์ไททาเนต
Structural properties and fabrication of $CaCu_3Ti_4O_{12}$ thin film capacitor

ยูมัยเราะห์ กาซา[1/] และ สตรีรัตน์ โฮดัค[2/]

Yumairoh Kasa[1/] and Satreerat Hodak[2/]

บทคัดย่อ

ฟิล์มบางแคลเซียมคอปเปอร์ไททาเนตถูกเตรียมด้วยเทคนิคโซลเจลแบบสปินบนแผ่นรองรับอลูมินาที่อุณภูมิ 800 องศาเซลเซียส ฟิล์มแคลเซียมคอปเปอร์ไททาเนตแสดงความเป็นผลึกที่ระนาบการเลี้ยวเบน (200), (400) และ (422) ตัวเก็บประจุที่มีขั้วไฟฟ้าแบบอินเตอร์ดิจิเตจที่มีระยะห่างระหว่างขั้ว 100 ไมครอนจะถูกสร้างขึ้นโดยการตกสะสมโครเมียมต่อด้วยทองผ่านหน้ากากลงบนฟิล์ม การตอบสนองของค่าความจุอยู่ในช่วง 1.4-1.5 พิโคฟารัด และค่าความสูญเสียความเป็นไดอิเล็กตริก อยู่ในช่วง 0.03-0.06 ค่าความจุมีค่าลดลงและค่าความสูญเสียไดอิเล็กทริกมีค่าเพิ่มขึ้น เมื่อค่าความต่างศักย์ถูกไบแอสให้เพิ่มขึ้นถึง 30 โวลต์

คำสำคัญ: แคลเซียมคอปเปอร์ไททาเนต, ค่าความจุ, วิธีโซลเจล

Abstract

$CaCu_3Ti_4O_{12}$ (CCTO) thin films have been prepared by a sol-gel spin coating technique on alumina substrates at temperature of 800 ºC. The X-ray diffraction patterns of CCTO films revealed the presence of polycrystallinity with the sharp diffraction peaks at (200), (400) and (422). The interdigitated capacitors with 100 micron gap were fabricated by depositing chromium and followed by gold through a shadow mask on CCTO films. The capacitance responses of the films were measured in the frequency range of 10-1000 kHz. The capacitance was on the order of 1.4-1.5 pF and the dielectric loss (tan δ) was on the order of 0.03-0.06. While the applied voltage increased up to 30 V, the capacitance decreased and the dielectric loss increased.

Keywords: $CaCu_3Ti_4O_{12}$, Capacitance, Sol gel method

Introduction

High dielectric constant materials are attracted much interest in the industry and the research filed due to remarkable number of applications in microelectronic devices such as Dynamic Random Access Memory (DRAM), capacitor applications and microwave devices (Jimenez *et al*., 2007; and Manik and Pradhan, 2006). Recently, $CaCu_3Ti_4O_{12}$ (CCTO) has been discovered to have colossal dielectric constant of 10^3–10^5 over a broad temperature range (200K to 600K) and low frequency range (1kHz-1MHz) (Fang and Shen, 2003). Many research groups have investigated several possible influences on the enhancement of the dielectric constant. In the work of Jimenez *et al*. the dielectric constant of the CCTO films on Pt/TiO_2/Si(100) substrates prepared by a sol-gel technique are on the

[1/]นิสิตบัณฑิตศึกษา ภาควิชาฟิสิกส์ คณะวิทยาศาสตร์ จุฬาลงกรณ์มหาวิทยาลัย

[2/]ภาควิชาฟิสิกส์ คณะวิทยาศาสตร์ จุฬาลงกรณ์มหาวิทยาลัย

order of 100-800 and the dielectric loss on the order of 0.2-0.4 (Jimenez *et al*., 2007). Lin *et al*. have shown that the epitaxial CCTO thin films grown on $LaAlO_3$ (001) by pulse laser deposition exhibited the dielectric constant of about 10,000 at room temperature with the low dielectric loss of 0.05 at 1 MHz (Lin *et al*., 2002). Yang *et al*. have found the effects of the extrinsic contact electrode on the reduction in dielectric properties of CCTO ceramic (Lui *et al*., 2007). In this article we fabricated coplanar capacitors by sputtering chromium and gold directly on CCTO thin films to avoid the effects of the extrinsic contact electrode. Also, the effects of annealing temperatures on the crystal structure forms were investigated. We presented the capacitance and the dielectric loss of the CCTO polycrystalline thin film as a function of frequency and applied DC voltage.

Experimental details

$CaCu_3Ti_4O_{12}$ thin films were synthesized by a sol-gel spin coating technique. In this work we used two types of substrates, Si (100) and polycrystalline alumina substrates. In order to determine the stoichiometry in CCTO thin films and the optimum annealing temperature to form polycrystalline films, Si (100) substrate was chosen in this study. Due to better electrical insulator property in alumina, polycrystalline alumina was used as a substrate and interdigitated electrode was patterned directly on the CCTO films in order to study their electrical properties. For the CCTO precursor preparation, calcium acetate was mixed with acetic acid and baked at 120 ºC. Then we added copper acetate, Ti(IV) isopropoxide, ethylene glycol and formamide with appropriate ratio. After the synthesis of CCTO precursor was completed, the CCTO precursor was spun-coated on alumina substrate at the spinning speed of 2000 rpm for 40 s. Then, the films were pre-heated at 120 ºC for 20 min in order to dry the gel and annealed at different annealing temperatures for one hour each layer. This procedure was repeated for several times to obtain the films with different layers. The flow chart of synthesis CCTO precursor and thin film preparation is shown in Fig.1. The crystal structure of the films was observed by X-Ray Diffractometer (XRD:BRUKER model D8-Discover). The coplanar capacitors were fabricated by depositing Au/Cr on the film through a shadow mask with gap width about 100 microns using DC sputtering. The capacitance and the dielectric loss of the film were measured by Impedance Analyzer (HP 4192A).

Results and discussion

Fig.2 shows the XRD patterns of CCTO films on Si (100) substrates prepared at different annealing temperatures. For the sample annealed at 600 ºC, the characteristic peaks of CCTO were not shown indicating that it has amorphous structure. As the annealing temperature increases to 700 ºC, not only TiO_2 diffraction peaks occur at 24.4, 27.5 and 54.4ºC but the unidentified peaks also develop as seen at 35.2º and 37.0º diffraction angles, respectively. However, the sample annealed at 700 ºC still did

not exhibit any characteristic peaks of CCTO. When the temperature increases above 700 ºC, the unidentified peaks at 35.2 and 37.0ºC diffraction angles disappeared. At the annealing temperature of 800 ºC, the three main peaks of CCTO which consist of (221), (400) and (422) planes appeared with high intensities. Other planes which were confirmed the polycrystallinity of CCTO developed at this temperature are (211), (310), (222), (310) and (321), respectively. At the temperature of 1000 ºC, the (211) main peak was sharper but the intensities of (400) and (422) planes decreased. Nevertheless, the TiO_2 peaks became sharper whereas the unidentified peaks at 21.7, 52.2 and 65.3ºC started to appeared. From the XRD database, these unidentified peaks are not either rutile (JCPDS 34-0180) or anatase (JCPDS 21-1272) TiO_2 . These impurity peaks could be Ca or Cu oxides. Based on the X-ray diffractograms results, we chose the annealing temperature to be 800 ºC for the study of electrical properties of CCTO polycrystalline films on alumina substrates. We deposited Au/Cr interdigitated electrode on the film through a shadow mask with gap width about 100 microns as seen in Fig.3. Fig.4 presents the XRD spectra of CCTO thin films grown on alumina substrate annealed at 800 ºC. All CCTO diffraction peaks grown on alumina substrate appeared at the same peak positions as the film grown on Si(100) substrate. Fig.5 shows the capacitance and loss tangent versus frequency of the CCTO films on alumina substrate annealed at 800 ºC. The capacitance and dielectric loss of the film decreased as the frequency increased. The capacitance of the film decreased from 1.46 pF to 1.44 pF with increasing in applied voltage from 0 to 30 V, respectively. This means with the electric field of 3×10^5 V/m applied to the film, we can see the changes in the capacitance. However, the loss tangent of the film increased as the applied voltage increased. The loss tangent slightly changed in the 10-30 V DC bias range. It is known that the behavior of dielectric properties could be explained by Maxwell-Wagner model in which the CCTO consist of semiconducting grains with insulating grain boundary. It has been reported that the decrease of grain boundary resistance caused the decrease in static permittivity (ε_s') which is proportional to capacitance ($\varepsilon_s' = C_{gb}/C_0$ where C_{gb} is grain boundary capacitance, C_0 is empty cell capacitance) in low frequency range with applied DC voltage. These results agree with other reports (Lui *et al*., 2007; and Li and Schwartz, 2007).

Conclusion

The CCTO polycrystalline films were successfully prepared by sol-gel spin-coating technique at the optimum temperature of 800 ºC. The capacitance of the film decreased from 1.46 pF to 1.44 pF with increasing in applied voltage from 0 V to 30 V, respectively. The capacitance and dielectric loss of the film decreased as the frequency increased.

Acknowledgement

The authors are grateful to The Thailand Toray Science Foundation (TTSF), The Thailand Research Fund (TRF), Department of Physics Faculty of Science Chulalongkorn University, The Graduate Thesis Grant and Center of Innovative Nanotechnology for financial support.

References

Jimenez, R., Calzada, M.L., Bretos, I., Goes, J.C. and Sombra, A.S.B., 2007. Dielectric properties of sol–gel derived $CaCu_3Ti_4O_{12}$ thin films onto $Pt/TiO_2/Si(100)$ substrates. Journal of the European Ceramic Society 27: 3829.

Manik, S.K. and Pradhan, S.K., 2006. Microstructure characterization of ball-mill-prepared nanocrystalline $CaCu_3Ti_4O_{12}$ by Rietveld method. Physica, 33: 160.

Fang, L. and Shen, M., 2003. Deposition and dielectric properties of $CaCu_3Ti_4O_{12}$ thin films on $Pt/Ti/SiO_2/Si$ substrates using pulsed-laser deposition. Thin Solid Films 440: 60.

Lin, Y., Chen, Y.B., Garret, T., Liu, S.W., Chen, Chen, C.L.L., Bontchev, R.P., Jacobson, A., Jiang, J.C., Meletis, E.I., Horwitz, J. and Wu, H.D., 2002. Epitaxial growth of dielectric $CaCu_3Ti_4O_{12}$ thin films on (001) $LaAlO_3$ by pulsed laser deposition. Applied Physics Letters 81: 633.

Lui, L., Fan, H., Fang, P. and Jin, L., 2007. Electrical heterogeneity in $CaCu_3Ti_4O_{12}$ ceramics fabricated by sol–gel method. Solid State Communications 142: 575.

Li, W. and Schwartz, R.W., 2007. Maxwell-Wagner relaxations and their contributions to the high permittivity of calcium copper titanate ceramics. Physical Review B, 75: 012104-3.

Subramanian, M.A., Li, D., Duan, N., Reisner, B.A. and Sleight, A.W., 2000. High Dielectric Constant in $ACu_3Ti_4O_{12}$ and $ACu_3Ti_3FeO_{12}$ Phases. Journal of Solid State Chemistry 151: 323.

Sinclair, D.C., Adams, T.B., Morrison, F.D. and West, A.R., 2002. $CaCu_3Ti_4O_{12}$: One-step internal barrier layer capacitor. Applied Physics Letters 80: 2513.

Li, Y.W., Hu, Z.G., Sun, J.L., Meng, X.J. and Chu, J.H., 2008. Preparation and properties of $CaCu_3Ti_4O_{12}$ thin film grown on $LaNiO_3$-coated silicon by sol–gel process. Journal of Crystal Growth 310: 378.

Chiodelli, G., Massarotti, V., Capsoni, D., Bini, M., Azzoni, C.B., Mozzati, M.C. and Lupotto, P., 2004. Electric and dielectric properties of pure and doped $CaCu_3Ti_4O_{12}$ perovskite materials. Solid State Communications 132: 241.

Homes, C.C., Vogt, T., Shapiro, S.M., Wakimoto, S. and Ramirez, A.P., 2001. Optical Response of High-Dielectric-Constant Perovskite-Related Oxide. Science 293: 673.

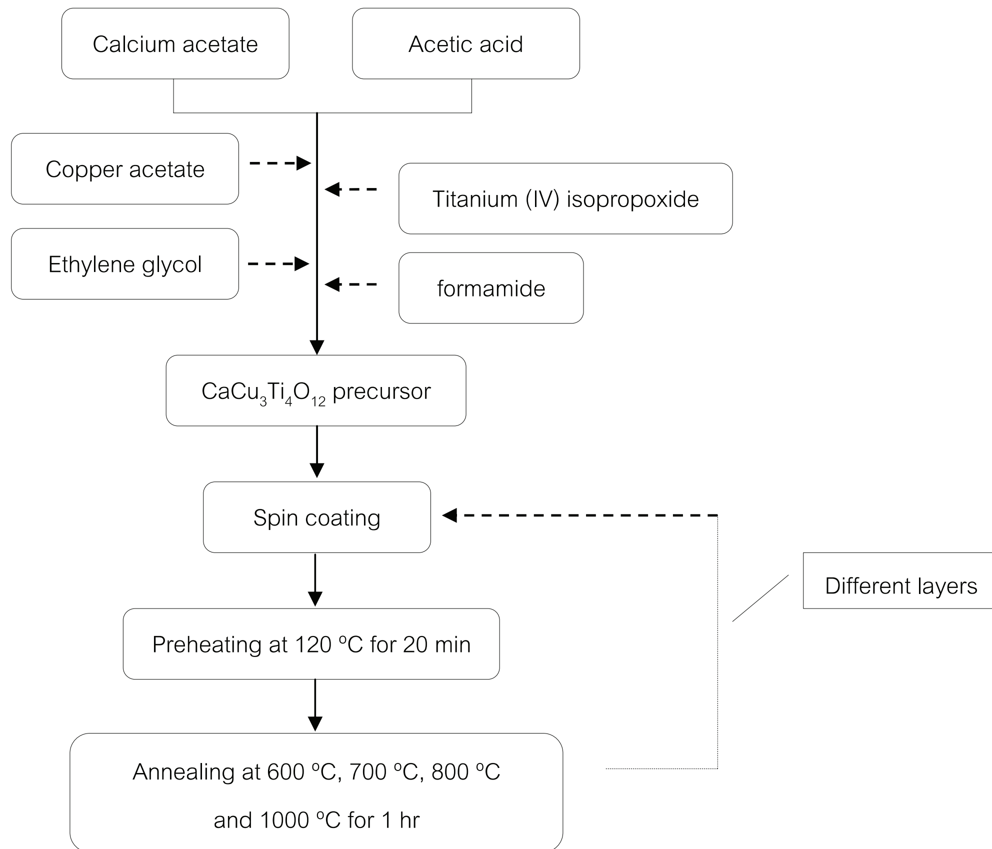

Fig. 1 The flow chart of synthesis CCTO precursor and thin film preparation.

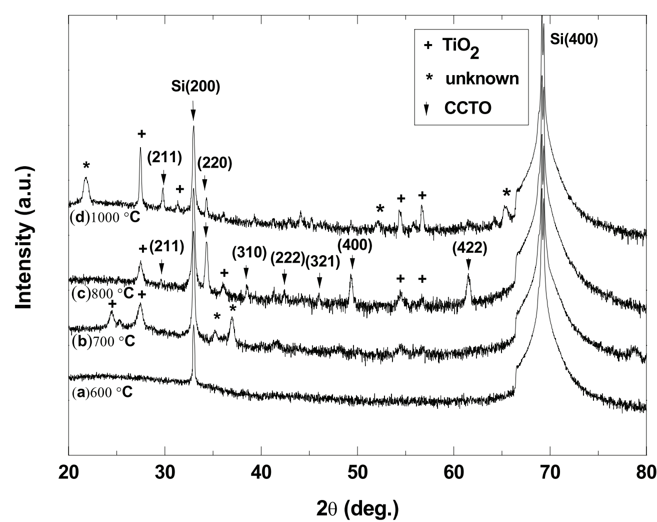

Fig. 2 XRD patterns of CCTO thin films on Si (100) substrate at different temperatures

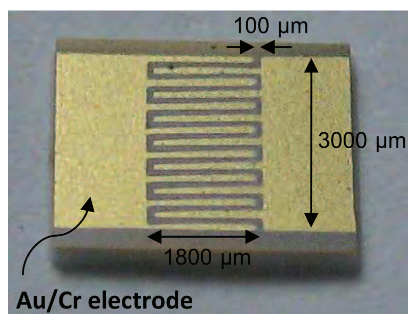

Fig. 3 Au/Cr electrode on CCTO films

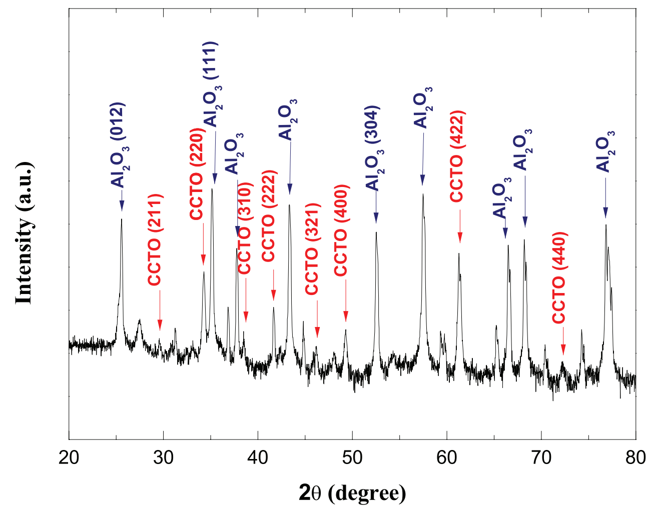

Fig. 4 XRD spectra of CCTO thin films on alumina substrate annealed at 800 °C temperatures

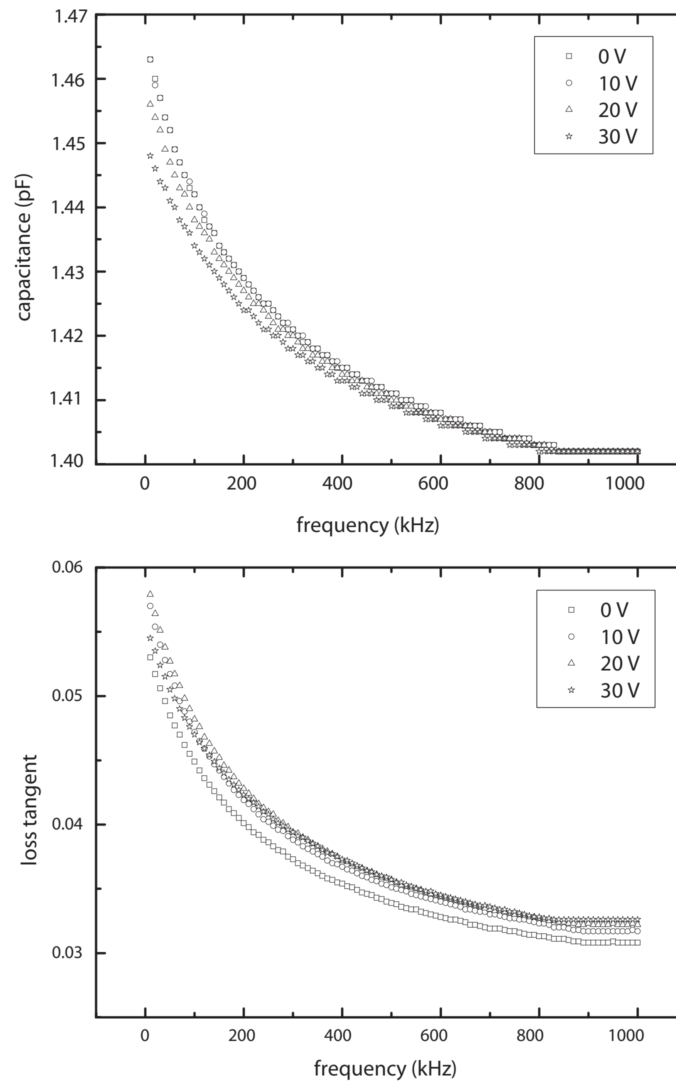

Fig. 5 The capacitance and loss tangent of the CCTO film on alumina substrate annealed at 800 ºC

Vitae

Miss Yumairoh Kasa was born on the 26th June 1985 in Pattani, Thailand. She finished high school from Dechapattanayanukul, Pattani, then received her Bachelor of Education degree in Science-Physics major from Thaksin University, Songkhla in 2007, and continued her master's study in Physics at Chulalongkorn University.